



Fracture Network Characterization using Hydrological and Geophysical Data

Caroline Dorn

► To cite this version:

Caroline Dorn. Fracture Network Characterization using Hydrological and Geophysical Data. Environmental Sciences. Université Lausanne, 2013. English. NNT : . tel-01099410

HAL Id: tel-01099410

<https://hal.science/tel-01099410>

Submitted on 8 Jan 2015

HAL is a multi-disciplinary open access archive for the deposit and dissemination of scientific research documents, whether they are published or not. The documents may come from teaching and research institutions in France or abroad, or from public or private research centers.

L'archive ouverte pluridisciplinaire **HAL**, est destinée au dépôt et à la diffusion de documents scientifiques de niveau recherche, publiés ou non, émanant des établissements d'enseignement et de recherche français ou étrangers, des laboratoires publics ou privés.



Faculté des géosciences et de l'environnement
Centre de recherches en environnement terrestre
(anciennement Institut de géophysique)

Fracture Network Characterization using Hydrological and Geophysical Data

Thèse de doctorat

Présentée à la
Faculté des géosciences et de l'environnement de
l'Université de Lausanne

par

CAROLINE DORN

Diplôme (Master of Science) en géophysique
Université de Leipzig (Allemagne)

date de soutenance: 28 Mars 2013

Jury

Prof. Dr. François Bussy, Président
Prof. Dr. Niklas Linde, Directeur de thèse
Prof. Dr. Klaus Holliger, Rapporteur
Prof. Dr. Frederick Day-Lewis, Expert
MER Dr. James Irving, Expert

Lausanne, 2013

IMPRIMATUR

Vu le rapport présenté par le jury d'examen, composé de

Président de la séance publique :	M. le Professeur François Bussy
Président du colloque :	M. le Professeur François Bussy
Directeur de thèse :	M. le Professeur Niklas Linde
Rapporteur :	M. le Professeur Klaus Holliger
Expert interne :	M. le Docteur James Irving
Expert externe :	M. le Professeur Frederik Day-Lewis

Le Doyen de la Faculté des géosciences et de l'environnement autorise l'impression de la thèse de

Madame Caroline DORN

Titulaire d'un
Master of Sciences in Geophysics
Université de Leipzig/Allemagne

intitulée

FRACTURE NETWORK CHARACTERIZATION USING HYDROLOGICAL AND GEOPHYSICAL DATA

Lausanne, le 28 mars 2013

Faculté des géosciences et de l'environnement



Professeur François Bussy, Doyen

Contents

Résumé	vii
Abstract	ix
1 Introduction	1
1.1 Preamble	1
1.2 Fractures	2
1.3 Fractured rock	3
1.3.1 Power law distributions	4
1.3.2 Fractals	4
1.3.3 Percolation theory	4
1.4 Flow and transport models of fracture aquifers	6
1.4.1 Flow and transport equations	7
1.5 Hydrological borehole investigations of fractured rock	8
1.5.1 Mechanical aperture versus equivalent aperture	9
1.6 Geophysical investigations of fractured rock	9
1.7 The GPR method	9
1.7.1 GPR applications in fractured rock	13
1.8 Data integration methods in hydrogeophysics	15
1.8.1 Deterministic methods	16
1.8.2 Stochastic methods	16
1.9 The Stang-er-Brune test site	18
1.10 Objectives and outline of the thesis	19
2 Fracture Imaging Using Reflection GPR Data	21
2.1 Abstract	22
2.2 Introduction	22
2.3 General setting of the crystalline aquifer	23
2.4 Multifold data acquisition	25
2.5 Data processing	25
2.6 Radar wavespeed estimation and borehole trajectory estimation	26
2.7 Single-hole processing	28

2.7.1	Processing challenges	28
2.7.2	Pre-stack time-domain processing	29
2.7.3	Pre-stack depth migration and stacking	30
2.8	Cross-hole processing	31
2.8.1	Challenges	31
2.8.2	Processing	33
2.9	Results	33
2.9.1	Single-hole GPR images	33
2.10	Discussion	35
2.11	Conclusions	38
3	GPR Reflection Imaging of Solute Transport	39
3.1	Abstract	40
3.2	Introduction	40
3.3	Field site and experiment	41
3.4	Data processing	42
3.5	Discussion	43
3.6	Conclusions	46
4	Inferring Transport Characteristics From Hydrological and Geophysical Monitoring Data	47
4.1	Abstract	48
4.2	Introduction	48
4.3	Methods	50
4.3.1	The single-hole ground-penetrating radar reflection method	50
4.3.2	Field site	52
4.3.3	Experimental setup	53
4.3.4	GPR data processing	55
4.4	Results	59
4.4.1	Tracer test data	59
4.4.2	Single-hole GPR data and difference imaging	62
4.5	Comparison of GPR reflection sections with tracer transport modeling	67
4.6	Discussion	70
4.7	Conclusions	73
5	Stochastic Generation of 3-D Connected and Conditioned Fracture Networks	75
5.1	Abstract	76
5.2	Introduction	76
5.3	Methodology	80
5.4	Field application	83

5.5	Results	90
5.6	Discussion	94
5.7	Conclusions	97
6	Conclusions and Outlook	99
6.1	Conclusions	99
6.2	Outlook	101
	Bibliography	103
	Acknowledgements	116
	Curriculum Vitae	117

Résumé

Les décisions de gestion des eaux souterraines doivent souvent être justifiées par des modèles quantitatifs d'aquifères qui tiennent compte de l'hétérogénéité des propriétés hydrauliques. Les aquifères fracturés sont parmi les plus hétérogènes et très difficiles à étudier. Dans ceux-ci, les fractures connectées, d'ouverture millimétrique, peuvent agir comme conducteurs hydrauliques et donc créer des écoulements très localisés. Le manque général d'informations sur la distribution spatiale des fractures limite la possibilité de construire des modèles quantitatifs de flux et de transport. Les données qui conditionnent les modèles sont généralement spatialement limitées, bruitées et elles ne représentent que des mesures indirectes de propriétés physiques. Ces limitations aux données peuvent être en partie surmontées en combinant différents types de données, telles que les données hydrologiques et de radar à pénétration de sol plus communément appelé géoradar. L'utilisation du géoradar en forage est un outil prometteur pour identifier les fractures individuelles jusqu'à quelques dizaines de mètres dans la formation. Dans cette thèse, je développe des approches pour combiner le géoradar avec les données hydrologiques afin d'améliorer la caractérisation des aquifères fracturés. Des investigations hydrologiques intensives ont déjà été réalisées à partir de trois forage adjacents dans un aquifère cristallin en Bretagne (France). Néanmoins, la dimension des fractures et la géométrie 3-D des fractures conductives restaient mal connue. Afin d'améliorer la caractérisation du réseau de fractures je propose dans un premier temps un traitement géoradar avancé qui permet l'imagerie des fractures individuellement. Les résultats montrent que les fractures perméables précédemment identifiées dans les forages peuvent être caractérisées géométriquement loin du forage et que les fractures qui ne croisent pas les forages peuvent aussi être identifiées. Les résultats d'une deuxième étude montrent que les données géoradar peuvent suivre le transport d'un traceur salin. Ainsi, les fractures qui font partie du réseau conducteur et connecté qui dominent l'écoulement et le transport local sont identifiées. C'est la première fois que le transport d'un traceur salin a pu être imagé sur une dizaine de mètres dans des fractures individuelles. Une troisième étude confirme ces résultats par des expériences répétées et des essais de traçage supplémentaires dans différentes parties du réseau local. En outre, la combinaison des données de surveillance hydrologique et géoradar fournit la preuve que les variations temporelles d'amplitude des signaux géoradar peuvent nous informer sur les changements relatifs de concentrations de traceurs dans la formation. Par conséquent, les données géoradar et hydrologiques sont complémentaires. Je propose ensuite une approche d'inversion stochastique pour générer des modèles 3-D de fractures discrètes qui sont conditionnés à toutes les données disponibles en respectant leurs incertitudes. La génération stochastique des modèles conditionnés par géoradar est capable de reproduire les connexions hydrauliques observées et leur contribution aux écoulements. L'ensemble des modèles conditionnés fournit des estimations quantitatives des dimensions et de l'organisation spatiale des fractures hydrauliquement importantes. Cette thèse montre clairement que l'imagerie géoradar est un outil utile pour caractériser les fractures. La combinaison de mesures géoradar avec des données hydrologiques permet de conditionner avec succès le réseau de fractures et de fournir des modèles quantitatifs. Les approches présentées peuvent être appliquées dans d'autres types de formations rocheuses fracturées où la roche est électriquement résistive.

Abstract

Groundwater management decisions must often rely on quantitative aquifer models that capture the heterogeneity of hydraulic properties. Fractured aquifers are one of the most heterogeneous types of aquifers and are very challenging to investigate. Connected millimeter-aperture fractures can act as hydraulic conductors and may provide very localized preferential pathways for fluid flow. The generally poor knowledge about the spatial distribution of hydraulically important fractures limits the ability to derive quantitative flow and transport models in such formations. The distribution of fractures are often poorly constrained by data that are spatially restricted, noisy, and represent indirect measures of physical properties. These data limitations can be partly overcome by combining different data types, such as hydrological and ground penetrating radar (GPR) reflection data. Borehole GPR imaging is a promising tool to image individual fractures up to some tens of meters away from boreholes. In this thesis, I develop approaches to combine GPR and hydrological data to improve the characterization of fractured aquifers. At a crystalline aquifer in Brittany, France, intensive borehole-based hydrologic investigations in three adjacent boreholes were previously performed, but a fracture length scale and the 3-D geometry of the conductive fracture network was poorly known. To overcome these limitations, I use GPR data to improve the fracture network characterization. First, I propose an advanced processing workflow that enables the imaging of fractures using multiple-offset borehole GPR data. The results illustrate that permeable fractures previously identified in borehole logs can be geometrically characterized away from their borehole intersections and that fractures that do not intersect the borehole can be identified. The results from a second study show that GPR reflection monitoring of saline tracer transport is a powerful tool to identify the fractures that are part of the conductive and connected fracture network that dominates local flow and transport processes. This is the first time that tracer transport over tens of meters in individual connected fractures could be imaged. A third study confirms these findings by repeated experiments and additional tracer tests stimulating different parts of the connected discrete fracture network. Furthermore, the combined interpretation of hydrological and GPR monitoring data acquired during tracer tests provides evidence that temporal changes of GPR amplitudes can provide information about relative changes in tracer concentrations away from the boreholes. Hence, the hydrological and geophysical imaging data are complementary. I then propose a stochastic inversion approach to generate 3-D discrete fracture models that are conditioned to all available data within their uncertainty ranges. The stochastic generation of GPR-conditioned fracture models is able to reproduce the observed hydraulic connections and their contribution to flow. The set of proposed conditioned models provides quantitative estimates of the length scales and the spatial organization of hydraulically important fractures. The different studies described herein give clear evidence that GPR imaging is a useful tool to characterize fractures. Its combination with hydrological data is able to successfully condition networks of hydraulically connected fractures and to provide quantitative fracture models. The presented approaches can be applied in other types of fractured rock formations where the host rock is electrically resistive.

Chapter 1

Introduction

1.1 Preamble

The current natural resource use is so high that future generations - and mostly developing countries - may be limited in their access to their fair share of scarce resources (e.g., Homer-Dixon, 1995; Postel, 2000). Moreover, the extensive use of natural resources and the subsequent production of waste have consequences on the environment that may induce serious damages that go beyond the carrying capacity of the environment (Krautkraemer, 1998). Since the 1980s, development politics attempt to account for the limitation of natural resources and try to implement their sustainable exploitation and use (e.g., EU Directive 80/68/EC, OJ L20 of 26.01.1980). Furthermore, most countries worldwide are aware that more responsible approaches should be taken for waste handling and disposal. Political directives on environmental issues rely partly on the scientific knowledge about those environments and their dynamics. With the increasing demand for resources and waste handling, the interest in understanding flow and transport dynamics in the subsurface has increased in the past decades.

Fractured rock formations are widespread on the globe (Struckmeier and Margat, 1995). Investigations of fractured formations often relate to their fundamental usages as (1) groundwater reservoirs, (2) petroleum reservoirs, (3) geothermal reservoirs and heat storage, (4) nuclear waste repositories and (5) mines. As an example, concerning the use of fractured rock as groundwater aquifers, approximately 30% of Swiss water supply is coming from fractured aquifers (mainly from springs) that cover about 78% of the subsurface of Switzerland (FOEN Switzerland, 2009).

Flow and transport in fractured rock formations are one of the most challenging subjects in hydrogeology. The spatial arrangement and connections between fractures are very difficult to capture but they may have a dominant influence on flow and transport processes at very different scales (individual fractures to regional scale). Predictive capabilities of fracture models are therefore generally limited. This thesis aims to contribute with new data types and methodologies to the characterization of fractured aquifers.

1.2 Fractures

A fracture is the local separation of rock that can be filled with different fluids (air, water, etc.). Fractures are caused by mechanical stress (compression or tension) beyond the rock strength. A fracture follows the weakest plane of the imposed stress.

Fractures can be classified in three major group: (1) dilating fractures or *joints* that are characteristically described as two rough surfaces with normal displacement, (2) shearing fractures or *faults* with parallel displacement between the rock surfaces and (3) closing fractures or *pressure solution surfaces* that only occur in sedimentary rocks (Long *et al.*, 1996). The genesis of fractures can underlie different mechanisms (mechanical, hydraulic, chemical and thermal) and are discussed in detail by Long *et al.* (1996) and references therein. In nature, often combinations of these three fracture types occur, the most common are faulted joints and jointed faults. Opposing walls of a developed joint that undergo motion different from the original movement may be displaced against each other (faulted joint). Joints and faults can be distinguished by their different surface texture. The opposing walls of joints show radial or antisymmetric plumose textures (Figure 1.1a), whereas fault walls bear characteristic linear traces. Furthermore, faults tend to have larger apertures than joints, that are commonly of hairline thickness. The aperture is the distance between the opposing fracture walls measured normal to their displacement. Due to the roughness of the opposing walls, channels may be produced that constitute potential fluid pathways.

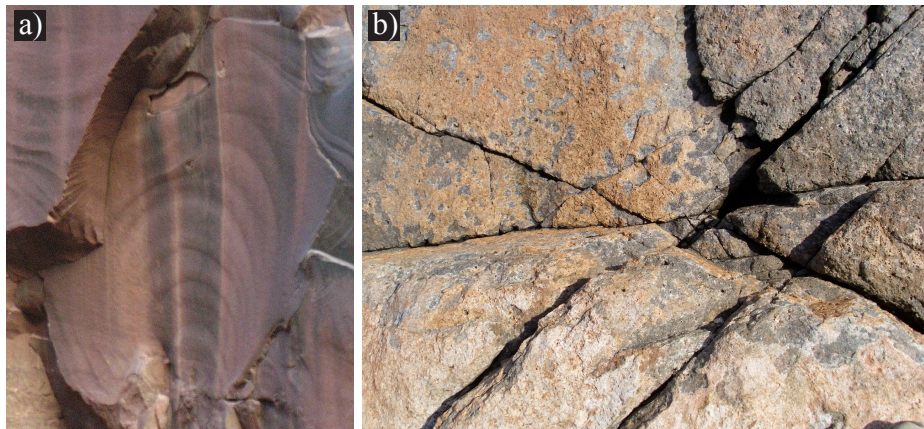


Figure 1.1: Photos of (a) plumose fracture surface in North Canyon, Arizona, adapted from Minnesota Geological Survey (2009), and (b) a granite fracture pattern from Schoodic Point, Acadia National Park, Maine (Henry, 2010).

The geometry of single fractures is often poorly known, because in-situ measurements of entire fracture planes are extremely difficult. The geometries of fractures depend on several factors during its genesis, as for example, the heterogeneity of the rock mass, the stress conditions and the interaction with neighboring fractures. Generally, joints are formed perpendicular to the imposed principal stress. In sedimentary rocks, joints often propagate perpendicular to the bedding planes (e.g., Engelder, 1987). In massive rocks (without internal layers, e.g., granite),

observations of single joints suggest straight planes with a circular or elliptical surface geometry (see also Figure 1.1a). The geometry of a straight plane may alter to a more wavy shape with ongoing propagation. The geometries of small faults (meters to some tens of meters) resemble those of joints, besides the mentioned differences in aperture and wall texture. In the following, the general term *fracture* is used when referring to the commonly observed fractured joints and jointed faults. Here, I focus on fractures with a spatial extent of meters to some tens of meters.

1.3 Fractured rock

Sets of fractures of the same type and age are approximately parallel. In nature, fractured rocks comprise a wide distribution of fracture orientations as rocks undergo different stress regimes during their formation history. Figure 1.1b shows a typical fractured formation in massive rock with fractures at different orientations. Natural fractures appear on a continuum of length scales, ranging from microcracks to crustal rifts that represent intrinsic lower and upper bounds. Geometrical characteristics of fractured rocks can be described, for example, by the spacing between fractures, the density of fractures and the distribution of fracture lengths and orientations (Long *et al.*, 1996). There are numerous concepts to geometrically quantify these fractured rock properties. They include distribution laws (power, exponential, log-normal) and fractals amongst others. Power laws and fractals can be used to describe fractured rocks with scale-invariant properties, meaning that no characteristic fracture length scale and thus no homogenization scale exist (Bonnet *et al.*, 2001). It is widely accepted that a wide range of fracture systems can be described by power laws and fractals, but certainly not all, as in the case when a characteristic length scale exist. The lack of a homogenization scale has important consequences on the use of equivalent porous media to describe hydraulic properties, as this is an underlying assumption of such approaches (Davy *et al.*, 2010). Bonnet *et al.* (2001) and references therein present a comprehensive description on the use of different distributions to describe fracture properties between intrinsic upper and lower bounds. The physical causes that underlie scale-invariant concepts have been examined by a number of authors (e.g., Main, 1996; Atkinson, 1987). Yet the physical grounds of the variations in parameters characterizing these distributions (i.e., power exponent, fractal length) are still poorly understood (Bonnet *et al.*, 2001). Studies of scaling properties have gained attention as fracture properties are easier to examine at laboratory or local scale, but it is often properties at the regional scale that are of interest. However, the description of real fractured rock using such concepts remain limited as supporting data is often 1-D (borehole logs) or 2-D (surface investigations), which makes 3-D extrapolation very difficult. For example, there is a bias introduced when evaluating fracture statistics based on borehole measurements. This bias is inherent to televiewer data that are preferentially sensing fractures dipping subhorizontally. With certain assumptions, it is possible to correct for this bias. In general, necessary corrections account for the effect of a spatially limited study area, for sampling bias due to the restrictions to borehole or surface

outcrops, or data resolution limitations. Unaccounted bias can lead to erroneous predictions for flow and transport in fractured rock, but the elimination of such bias is a very challenging task.

The geometrical distribution of fractures defines how likely connections between fractures are and thus how well a fracture network is connected. Adjacent fractures may build connected clusters at least up to the kilometer scale (Pollard and Aydin, 1984). But fracture formations that appear to be heavily fractured may not, in fact, be well-connected. Fracture spacing is one of the key parameters for connectivity in fractured media (e.g., Wu and Pollard, 1991). To quantify connectivity of a network, its underlying fracture distribution can be analyzed using percolation theory. In the following, I will briefly introduce the concept of power laws and fractals, as well as their analysis based on percolation theory.

1.3.1 Power law distributions

In contrast to other distributions, such as lognormal, exponential or gamma laws, the power law distribution does not imply a characteristic length scale. Many distributions of fracture properties l (e.g., fracture length) can be described by $n(l) = Al^{-a}$, where a is the power exponent, usually in the range of $1 < a < 3$ (Berkowitz, 2002), and A is a constant. A population that shows a linear behavior on a log-log graph of $n(l)$ versus l over sufficient ranges of scale (more than 1 order of magnitude) can be described by a power law.

1.3.2 Fractals

Fractal concepts assume that fracture patterns at different scales are quantitatively similar. Numerous studies have examined the application of fractals to describe properties of fracture networks (fracture density, fracture lengths) or single fractures (surface roughness) (e.g., Turcotte, 1997; Bonnet *et al.*, 2001). As an example, the most wide application of fractals is the box-counting method, where the fractal objects are covered by $N(r)$ number of boxes of size r . By varying the size r , the number of boxes should vary as $N(r) \approx r^{-D}$, where D is the fractal dimension. One way to define D is thus

$$D = \lim_{r \rightarrow 0} \frac{\ln N(r)}{\ln(1/r)}, \quad (1.1)$$

where the fractal dimension is obtained for infinitely small details of the objects.

1.3.3 Percolation theory

Percolation theory can be used to describe the global physical parameters of a fractured system. It is based on populations of sparsely distributed fractures in an impervious matrix. Geometrical properties that are described by distribution laws are linked through percolation theory to, for example, the system connectivity or permeability.

System connectivity describes the degree to which the system establishes connected paths between the far ends of the system. One way to quantify connectivity is to use the average number of intersections per fracture (Robinson, 1983; Berkowitz, 1995). Connectivities of simulated networks show a high degree of sensitivity to the underlying fracture distributions. The relevant parameters to quantify fracture network connectivity are still a subject of debate (e.g., Berkowitz, 2002). The system permeability describes the ability of a system to allow fluids to pass through.

Figure 1.2a and b shows some 2-D fracture network realizations with roughly similar number of fractures (Bour and Davy, 1997). The number of fractures in Figure 1.2a may seem much fewer, but the system size is 5000 times larger than in Figure 1.2b and hence a lot of small-scale fractures are below the resolution limit of the figure. The larger fractures in these networks play a key role in connecting the far ends of the system.

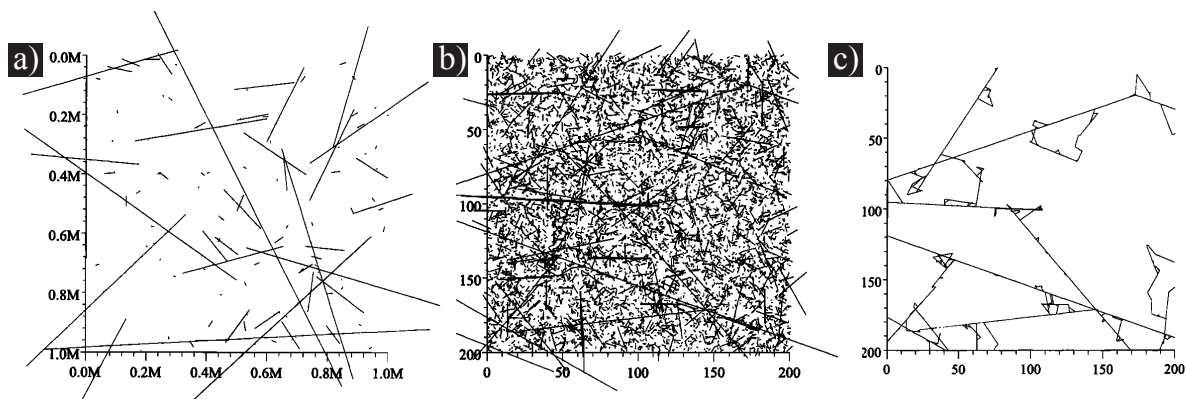


Figure 1.2: Example of 2-D fracture systems at percolation threshold that follow power law length distributions with (a) $a = 1.5$ and (b) $a = 2.5$. (c) The backbone of the fault system in (b). Note the different system sizes in (a) and (b). Adapted from Bour and Davy (1997).

For fracture systems there exist a so-called percolation threshold p_c , the critical density of fractures necessary to connect the boundaries of the system (Robinson, 1983). The fracture systems in Figure 1.2a and b are at this critical density, but because their underlying power law length distributions are different the critical density is smaller for the system described by $a = 1.5$ than for the system with $a = 2.5$. At the critical density, the connectivity is strongly dependent on the exponent a of the underlying fault-length distribution (Bour and Davy, 1997).

Just above p_c , network properties behave proportional to $(p - p_c)^x$, where x is a quantity specific exponent, p_c is the critical number of fractures at the percolation threshold and p is the total number of fractures in the system (Stauffer, 1985). The percolation threshold depends on the dimensionality of the system, the geometry of fractures and the underlying fracture distribution. Note that the permeability of a network is not proportional to the probability that any fracture is part of the connected cluster. This is because in a fractured system, not all fractures contribute to the total flow. Only fractures that are connected from the initial to the terminal points can contribute to the total flow (e.g., Berkowitz, 1995). A connected cluster of

fractures generally consists of fractures that are part of the backbone (the fractures through which fluid flow occurs) and dead-end fractures (which do not conduct significant amounts of fluid). Figure 1.2c shows the backbone structure of the fracture system in Figure 1.2b that is responsible for the connection between the four sides of the system. Only a small fraction of fractures are part of the backbone, for exponents $a = 2.5$ this fraction is less than 5% (Bour and Davy, 1997). The percentage of fractures that belong to the backbone is dependent on the fracture length exponent a . For such systems as in Figure 1.2a (for $a = 1.5$), there might be only one fracture that is part of the backbone and hence a high probability of occurrences of large fractures dominating the percolation threshold (Bour and Davy, 1997).

A detailed description on percolation theory can be found in Stauffer (1985).

1.4 Flow and transport models of fracture aquifers

Highly fractured rocks are potential aquifers with significant water supply. Host rocks of fractured aquifers can be of any kind of consolidated rock: sedimentary (e.g., sandstones), igneous (e.g., granite) or metamorphic (e.g., gneiss). In water-saturated rock, the fractures are filled with water. If a pressure gradient is imposed along a fracture, water will move from regions of high to regions of low pressures. Such a pressure-driven flow can occur within and between connected fractures. Water flow through the rock formation depends on its permeability (k in m^2), that is the ability of a rock to allow fluids to pass through. Permeability is an intrinsic parameter, independent of the fluid. It can vary greatly between $10^{-7}m^2$ for well sorted gravel to $10^{-25}m^2$ for almost impervious rocks. The often used hydraulic conductivity (K in m/s) is a measure of the volume of water that can move through a cross-sectional area of a media in a given time for a unit pressure gradient. The hydraulic conductivity K relates to the permeability k through the viscosity μ (kg/sm), the density ρ (kg/m³) of the fluid and the gravitational acceleration g (m/s²) as:

$$k = K \frac{\mu}{\rho g}. \quad (1.2)$$

The volume of water that can flow through a cross-sectional area of a layer (perpendicular to the flow direction) times its aperture for a unit pressure gradient in unit time is defined by the transmissivity (T in m^2/s). The transmissivity of a media can be defined by the layer thickness times its hydraulic conductivity (for a fracture it would be aperture times hydraulic conductivity). The heterogeneities of permeability and connectivity of a fractured rock define the amount of possible flow through the system, in which the fractures might have a significant impact (Berkowitz, 2002). Furthermore, due to the variation in geometrical apertures within a single fracture, flow might be organized in channels. At the system scale, flow might be organized in preferential pathways due to the different connectivities between the fractures. Field and laboratory experiments give strong evidence of the common occurrence of

flow channeling in individual fractures and preferential flow paths in fracture networks (e.g., Neretnieks *et al.*, 1982; Becker and Shapiro, 2000).

Flowing water in the subsurface can carry solutes (e.g., contaminants) along flow paths. In a homogeneous media, there are two transport mechanisms that move solutes. Advection is the movement of solutes due to the bulk flow of a fluid, where solutes are moved along the streamlines that follow the gradient of the imposed pressure field. Diffusion can describe the degradation of concentration differences due to Brownian motion of the particles. The rate of diffusive transport for a solute is described by the diffusion coefficient that depends on physical properties of the solute and the solvent. In a heterogeneous media, the attenuation of concentration differences also occurs due to the heterogeneity of the flow velocity field. Adjacent particles that are transported at different velocities move apart. This mechanism is called dispersion. Solutes may also be adsorbed to surfaces of the solid phase (i.e., grains), in a process that is usually reversible. Solutes can diffuse from the fractures into the rock matrix and the rock matrix may adsorb them.

Widely used transport models involve advection and dispersion driven transport in the fracture system and diffusion into the more or less porous rock matrix. Depending on the type of rock, the permeability and adsorption of the rock matrix might significantly affect flow and transport processes. In some cases, the matrix permeability is negligible, although in other cases it can contribute significantly to flow. This depends largely on the media of investigation, the time-scales considered and the flow velocities. Fluid flow and transport in fractured impervious rock versus fractured porous rock are thus partly dominated by different mechanisms.

1.4.1 Flow and transport equations

From the conservation of motion it is possible to derive a governing equation for fluid flow. Locally, this can be accurately described by the Navier-Stokes equation (for Newtonian fluids):

$$\rho \left(\frac{\partial \mathbf{u}}{\partial t} + (\mathbf{u} \cdot \nabla) \mathbf{u} \right) = -\nabla P + \mu \nabla^2 \mathbf{u} \quad (1.3)$$

where \mathbf{u} is the velocity vector in m/s and P is the pressure in kg/ms². Yet, the solution of the Navier-Stokes equation is computationally expensive for complex geometries and it is difficult to solve on an irregular geometry of rock fractures (e.g., Zimmerman and Yeo, 2000).

Based on empirical observations, Darcy's law has been developed; it can also be derived by the Navier-Stokes equations via homogenization (Allaire, 1989). Darcy's law relates the flux q (discharge per unit area, in m/s) through

$$q = -\frac{k}{\mu} \nabla h, \quad (1.4)$$

with ∇h being the head gradient (De Marsily, 1986, p. 56). Its principle physical property is the permeability k . Permeability is often assumed to be closely related to fracture aperture

$k \sim b^2$ (e.g., Zimmerman and Bodvarsson, 1996).

From the conservation of mass it is possible to derive a governing equation for solute transport that is often described by the advection-dispersion equation:

$$\frac{\partial C}{\partial t} = -\mathbf{u} \cdot \nabla C + D \nabla^2 C \quad (1.5)$$

where D is the diffusion-dispersion coefficient (in m^2/s), \mathbf{u} is the velocity field and C is the concentration field. The diffusion-dispersion coefficient is the sum of the diffusion coefficient and the product of fluid velocity times dispersivity (Ingebritsen and Sanford, 2006).

1.5 Hydrological borehole investigations of fractured rock

Hydraulic and tracer tests within or between boreholes are generally based on perturbing the groundwater system and measuring the resulting effects of this perturbation (e.g., by imposing a hydraulic gradient, releasing a tracer solution). These types of methods yield information on flux-averaged bulk properties (e.g., hydraulic conductivity, storativity, porosity).

Hydraulic tomography is an approach that often involves a series of packer tests used to derive a tomographic image of the hydraulic diffusivity field (ratio of hydraulic conductivity to specific storage). Water is pushed in a packed-off interval while its pressure response is measured in the observational packed-off interval. High resolution tomographic images necessitate a large number of packer tests. However, the resulting tomograms do generally not resolve individual fractures, but fracture zones (e.g., Hao *et al.*, 2007). A difficulty that often arises, however, is that short-circuiting by interconnected fractures yields misleading results. Single-hole and cross-hole flowmeter testing can be employed without or limited use of packer systems. During a flowmeter test, a head gradient is imposed to the system and the resulting in- and outflow at the intersections of permeable fractures with the borehole are determined. In the same manner, but without imposing a hydraulic gradient, the effect of the ambient flow regime on the borehole intersecting fractures is obtained (e.g., Paillet, 1998; Le Borgne *et al.*, 2007).

Tracer tests are generally applied to determine the connectivity between well-defined locations in the subsurface and to estimate the transport properties of the involved transport path (dispersivity, adsorption). In fractured rock where flow is often very localized, tracer tests are usually performed by imposing a large hydraulic gradient to assure that the tracer arrives at the desired location (e.g., Tsang and Neretnieks, 1998). Imposing a high hydraulic gradient impact the estimates of hydrological parameters (e.g., Becker and Shapiro, 2003; Kosakowski and Berkowitz, 1999). In addition, the heterogeneous connectivity between the fractures at the field scale can lead to highly varying tracer arrival times (very short as well as very long) and tracer arrival locations. The inference of solute transport in fracture networks remains a challenging task in hydrology, because of the dominance of connectivity on the topology of a fracture network at the field scale that is generally poorly understood.

1.5.1 Mechanical aperture versus equivalent aperture

Natural fractures are likely to be rough walled, with walls contacting each other at discrete points and thus lowering total flow (e.g., Long *et al.*, 1996). In this case, an *equivalent aperture* is derived from hydraulic or tracer tests, which represents a simplified phenomenological parameter for the description of flow and transport through fractures. There are three different definitions of equivalent aperture: mass balance aperture, frictional loss aperture and cubic law aperture (Tsang, 1992; Abelin *et al.*, 1985). In general, the three definitions yield estimates that are smaller than the actual mechanical aperture (e.g., Klimczak *et al.*, 2010; Zimmerman and Bodvarsson, 1996). The relation between the mechanical and the equivalent apertures has been studied with limited success (Tsang, 1992). Different approaches have been used to derive one representative hydraulic aperture by introducing an empirical relation to the geometrical aperture based on hydromechanical coupling experiments (e.g., Barton *et al.*, 1985), corrections with a friction factor (e.g., Witherspoon *et al.*, 1980) due to the tortuosity of the flow path in the fracture (e.g., Cook *et al.*, 1990) or the geometric mean of the aperture distribution (e.g., Renshaw, 1995).

1.6 Geophysical investigations of fractured rock

The most common geophysical methods for fractured aquifer characterization are electrical resistivity tomography (ERT), ground-penetrating radar (GPR), electromagnetic (EM) methods and seismic methods. The direct dependence of bulk electrical conductivities on water content can be used in ERT measurements to resolve fracture zones, but the resolution of resistivity tomograms is insufficient to identify individual fractures (e.g., Day-Lewis *et al.*, 2005). Other tomographic methods that use seismic or radar travel times suffer from similar resolution limitations. Even when full-waveform inversions are applied to GPR transmission data, the resolution is still likely to be more than ten times larger than usual fracture apertures ($a < 10$ mm). EM methods give volume estimations of electrical conductivities, they have for instance been investigated to study electrical anisotropy that is due to preferred fracture orientations of fracture formations (Linde and Pedersen, 2004). The use of GPR reflection imagery is a promising tool to identify individual fractures (e.g., Olsson *et al.*, 1992). A general description of hydrogeophysical methods for the investigation of aquifers can be found, for example, in Hubbard and Linde (2011).

1.7 The GPR method

The ground-penetrating radar (GPR) technique uses electromagnetic (EM) waves, usually in the 10 MHz - 1 GHz range, to detect electromagnetic contrasts in the subsurface. The operation modes of GPR is similar to those of seismics, where a source pulse is emitted from a transmitter antenna into the subsurface and a receiver antenna registers the energy that is partially reflected back on inhomogeneities of the subsurface. The image processing of a

raw GPR section requires the understanding of the propagation of an EM wave through the subsurface, as summarized in the following. The following equations are cited from Balanis (1989) and Annan (2005), in which comprehensive descriptions on EM wave propagation theory can be found.

EM wave propagation is governed by the well-known Maxwell's equations and three constitutive parameters that control the propagation of EM waves through materials. All of them can be complex and frequency dependent: the electrical conductivity σ (S/m), the dielectric permittivity ϵ (F/m) and the magnetic permeability μ (N/A²). Figure 1.3 gives an overview of the large ranges of σ , while the variability in magnetic permeability is typically negligible. The ranges of permittivity are often expressed in terms of the relative permittivity (i.e., dielectric constant) of a material ϵ_r , that is the ratio between the absolute permittivity of the material and the vacuum permittivity $\epsilon_0 = 8.85 \times 10^{-12}$ F/m. For fresh and salt water at room temperature ϵ_r is 80, while for pure ice it is between 3-4, for granite between 4-6 and below 30 for most sedimentary rocks saturated with fresh water (Davis and Annan, 1989).

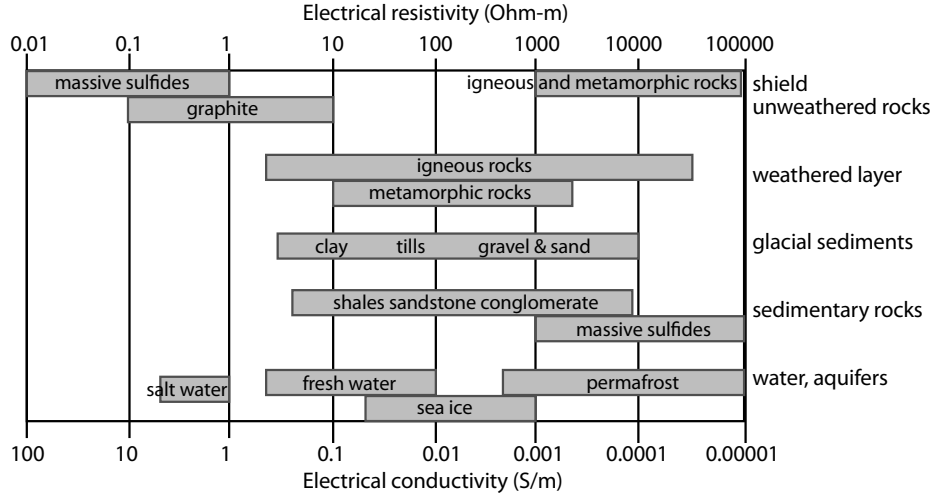


Figure 1.3: Electrical conductivity σ and corresponding electrical resistivity ranges of earth materials. Adapted from Palacky (1988).

The basic wave equations describing electrical and magnetic vector fields (\mathbf{E} and \mathbf{B} , respectively) can be written as:

$$\nabla^2 \mathbf{E} = \mu\epsilon \frac{\partial^2 \mathbf{E}}{\partial t^2} + \mu\sigma \frac{\partial \mathbf{E}}{\partial t} \quad (1.6)$$

$$\nabla^2 \mathbf{B} = \mu\epsilon \frac{\partial^2 \mathbf{B}}{\partial t^2} + \mu\sigma \frac{\partial \mathbf{B}}{\partial t} \quad (1.7)$$

The solutions for a monochromatic, linearly polarized wave that propagates through a homogeneous media in the z -direction can be written in complex notation as

$$\tilde{\mathbf{E}}(z, t) = \tilde{\mathbf{E}}_0 e^{i(\omega t - \hat{k}z)} \quad (1.8)$$

$$\tilde{\mathbf{B}}(z, t) = \tilde{\mathbf{B}}_0 e^{i(\omega t - \hat{k}z)} \quad (1.9)$$

where w is the angular frequency $2\pi f$ (with f (Hz) being the natural frequency), t (s) is time and \hat{k} (1/m) the wavenumber. $\tilde{\mathbf{E}}$ and $\tilde{\mathbf{B}}$ are complex electric and magnetic field vectors and $\tilde{\mathbf{E}}_0$ and $\tilde{\mathbf{B}}_0$ are the complex amplitudes defining polarization and phase of the wave at $z = 0$. The physical fields \mathbf{E} and \mathbf{B} are the real parts of equations 1.8 and 1.9. For a plane wave, the electric and magnetic fields are perpendicular to the direction of propagation and to each other. The wavenumber is complex and depends on the frequency and the three constitutive material parameters. Splitting \hat{k} in its real \hat{k}_{real} and imaginary part \hat{k}_{im} , equations 1.8 and 1.9 can be rewritten as

$$\tilde{\mathbf{E}}(z, t) = \tilde{\mathbf{E}}_0 e^{-\hat{k}_{im}z} e^{i(wt - \hat{k}_{real}z)} \quad (1.10)$$

$$\tilde{\mathbf{B}}(z, t) = \tilde{\mathbf{B}}_0 e^{-\hat{k}_{im}z} e^{i(wt - \hat{k}_{real}z)} \quad (1.11)$$

with imaginary and real part of the wavenumber denoted as

$$\hat{k}_{im} = w \sqrt{\frac{\mu\epsilon}{2} \left(\sqrt{1 + \left(\frac{\sigma}{q\epsilon}\right)^2} - 1 \right)} \quad (1.12)$$

$$\hat{k}_{real} = w \sqrt{\frac{\mu\epsilon}{2} \left(\sqrt{1 + \left(\frac{\sigma}{q\epsilon}\right)^2} + 1 \right)} \quad (1.13)$$

where the imaginary part of the wavenumber (equation 1.12) defines the attenuation (usually denoted as α), meaning the exponential decrease of the wave amplitude as the wave travels along z . The attenuation of electromagnetic waves is frequency dependent. High frequencies are attenuated much more quickly than low frequencies. This is why the GPR wavelet, which is a composition of a range of frequencies, changes shape as it travels through the subsurface. This phenomenon is known as wave dispersion and results in a blurry appearance of GPR images that increases with depth. The real part of \hat{k} determines the wave speed v and the wavelength λ of the wave by:

$$v = \frac{w}{\hat{k}_{real}} \quad (1.14)$$

$$\lambda = \frac{2\pi}{\hat{k}_{real}} \quad (1.15)$$

For high enough frequencies and low enough conductivities of the medium, the low-loss condition $\sigma/w\epsilon < 1$ can be assumed that approximates the definitions of attenuation and wave speed to:

$$k_{im} \approx \frac{\sigma}{2} \sqrt{\frac{\mu}{\epsilon}} \quad (1.16)$$

$$v \approx \frac{1}{\sqrt{\mu\epsilon}} \quad (1.17)$$

When an EM wave encounters an electromagnetic boundary (contrast in σ , ϵ or μ), reflection and refraction occur. For a reflected wave, the reflection angle is equal to the incidence angle. In case of transmission through an interface, there is a change in the direction of wave

propagation, this is called refraction. Snell's law describes the change in direction by the contrast in wave speed between two layers (v_1 and v_2). The incidence angle β_1 is related to the refracted angle β_2 as:

$$\frac{\sin \beta_1}{\sin \beta_2} = \frac{v_1}{v_2} \quad (1.18)$$

The ratio between the amplitudes of reflected and incident waves are given by the reflection coefficient R (similarly for transmitted waves with the transmission coefficient T , where $T = 1 - R$). For the special case of a normal incident plane wave on a planar boundary between two layers 1 and 2 (for TE mode¹), the reflection coefficient can be written in a simplified form (Griffiths, 1998):

$$R = \frac{\mu_2 k_1 - \mu_1 k_2}{\mu_2 k_1 + \mu_1 k_2} \quad (1.19)$$

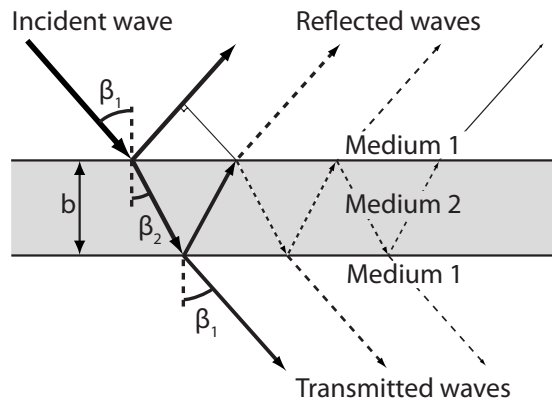


Figure 1.4: Schematic representation of the complex wave interferences of multiple wave reflections and transmissions for an incident wave on a fracture embedded between two identical layers. Adapted from Deparis and Garambois (2009).

In the special case of a fracture in solid rock forming the EM boundary, there is not one contrast between two layers but one thin layer enclosed between two layers of the same kind. As the fracture aperture b is normally much smaller than the wavelength of the signal traveling within the fracture ($\lambda/b \gg 4$), multiple reflections between the two interfaces create frequency-dependent interferences (Figure 1.4) (Deparis and Garambois, 2009). Deparis and Garambois (2009) derived an expression of thin-bed reflection coefficients that describe the dependence on the dielectric properties of the propagating medium and of the filling material on the aperture of the thin bed, on the incidence angle of the wave, and finally on the frequency of the signal:

$$R(w) = \frac{R_{12}(w) - R_{12}(w)e^{-i\phi(w)}}{1 - R_{12}^2(w)e^{-i\phi(w)}} \quad (1.20)$$

¹electric field vector is parallel to the strike of a dipping fracture plane, whereas in the TM mode the electric field vector is perpendicular to it

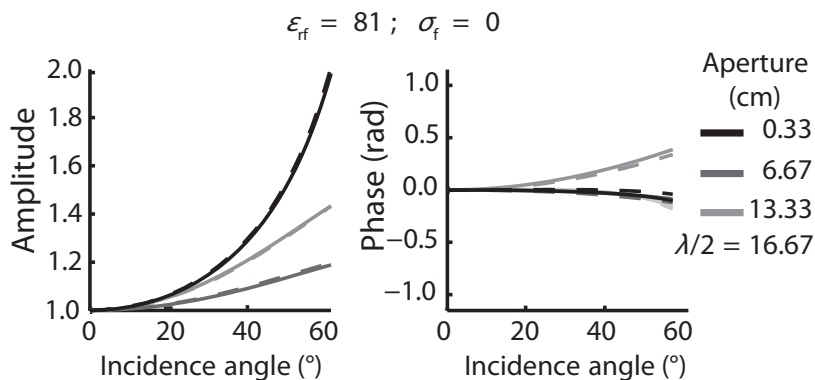


Figure 1.5: Amplitude and phase variations as a function of incidence angle for a wave that is reflected on a water filled fracture of varying apertures between two layers of homogeneous limestone with $\epsilon_r = 9$ and $\sigma = 10^{-3}$ S/m. The curves were computed for a signal frequency of 100 MHz. Adapted from Deparis and Garambois (2009).

where $\phi(w) = 2b\hat{k}_2(w)\cos(\beta_i)$ and $\hat{k}_{real1,2} = w\sqrt{\mu_{1,2}\epsilon_{1,2}}$. R_{12} is referring to the reflection coefficient between layers 1 and 2, and β_i is the incidence angle. Figure 1.5 illustrates an example of a water-filled fracture in limestone. The black curve refers to a model of a fracture with an aperture that is 100 times smaller than the wavelength, which is also a realistic case for fractures in massive rock (i.e., granite).

1.7.1 GPR applications in fractured rock

The literature is rich of GPR applications to very different near-surface investigations starting with early works in the 1960s on mapping ice sheet thickness (e.g., Waite Jr, 1966). A lot of work has been done related to nuclear waste repositories during the last 30 years (e.g., Olsson *et al.*, 1992). The use of GPR data for imaging fractures was explored by a series of studies (e.g., Hollender *et al.*, 2001; Grasmueck, 1996). More recent studies investigate the use of GPR phases and amplitudes to quantify properties of individual fractures (e.g., fracture aperture, fracture filling) (e.g., Tsofias and Hoch, 2006; Deparis and Garambois, 2009; Lane Jr *et al.*, 2000).

Surface GPR reflection data can image shallow dipping fractures under favorable circumstances (Grasmueck, 1996). Tsofias *et al.* (2004) give evidence that polarization properties of EM wavefields can be used to identify also steeply dipping fractures due to the phase difference between orthogonal pairs of polarization data sets. Surface-based applications provide a fairly well-constrained model of subsurface fracture geometry. Commonly used borehole antennas are restricted to omnidirectional radiation patterns around the borehole axis and thus poorly constrain azimuths of imaged reflectors. Directional borehole antennas have been developed but are not widely used (for a review on this topic, see Slob *et al.*, 2010). There exist directional antenna systems that require mechanical rotation and those where the directivity can be derived through data processing (e.g., Eisenburger and Gundelach, 2000; Ebihara *et al.*,

2000). Using state-of-the-art directional systems, the azimuth of imaged reflectors can be resolved with an accuracy of about 30° (Slob *et al.*, 2010). The fracture-detection limitations of the GPR method are restricted to (1) the areas of fractures with favorable orientation namely where normal vectors exist that cut the observation profile between transmitter and receiver positions, (2) fracture areas that are larger than the first Fresnel zone, and (3) fractures that lie within the penetration depth of the GPR method. Note that in highly fractured media the imaging of individual fractures might be very challenging.

The employment of GPR methods for monitoring temporal changes during pumping or tracer tests allows to obtain spatial information on flow and transport dynamics in the subsurface in between observation boreholes. Using cross-borehole radar in fractured granite, radar attenuation experiments during tracer injection were successful to detect changes due to tracer occupation (Ramirez and Lytle, 1986; Daily and Ramirez, 1989, in welded tuff) or to image the movements of the tracer through regions of high fracture intensity (Day-Lewis *et al.*, 2003). Using surface reflection GPR data, Tsofias *et al.* (2001) monitored the GPR amplitude response of a shallow radar reflector during a pumping test in fractured dolomite. They found that changes in the water saturation of the fracture could be correlated to the GPR signal. By a combined interpretation of GPR results and hydrological data, they could identify asymmetric drainage patterns. When GPR is used for monitoring tracer experiments (e.g., Day-Lewis *et al.*, 2003; Tsofias and Becker, 2008), saline solutions are usually used, as the resulting electrical conductivity contrast between fresh groundwater and the saline tracer is well pronounced and saline tracers are cheap. Talley *et al.* (2005) injected a tracer under both natural hydraulic gradient conditions and dipole pumping test configurations in a subhorizontal fracture zone in a sandstone aquifer. Temporal amplitude variations could be correlated to tracer movements and to changes in the electrical conductivity of the fracture fluid.

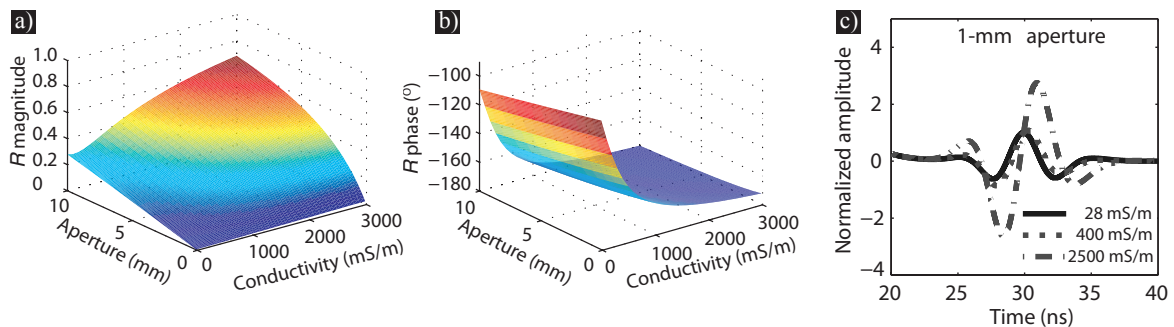


Figure 1.6: (a) Magnitude and (b) phase of the reflection coefficient R as a function of fracture aperture and water electrical conductivity for a signal frequency of 100 MHz. (c) Numerically simulated GPR traces reflected from a 1-mm-aperture fracture between two layers of sandstone, saturated with low-, medium-, and high-salinity water. Fractured-rock-matrix relative permittivity and electrical conductivity were set to 7 and 0.1 mS/m, respectively; the relative permittivity of water to 80; and EM wave angle of incidence to 7.5° to simulate field acquisition. Adapted from Tsofias and Becker (2008).

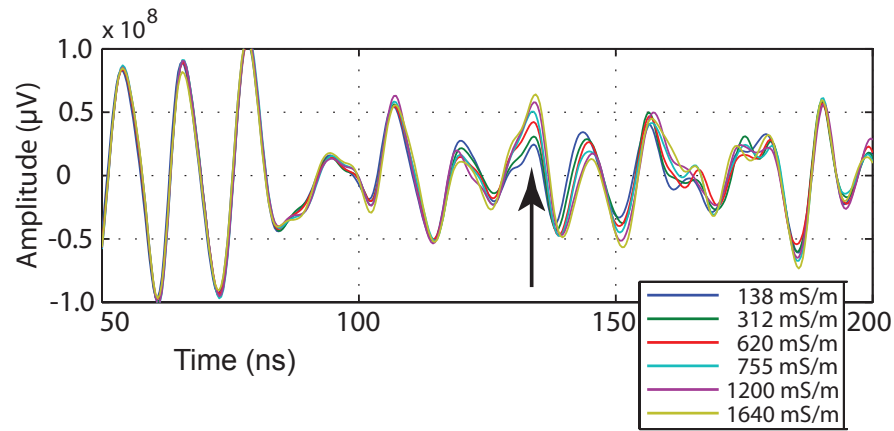


Figure 1.7: Acquired GPR traces during a tracer injection experiment in a subhorizontal fracture of 0.5 mm aperture located 7.6 m below ground surface using a central frequency of 100 MHz. For display purposes, there is a gain and a low pass frequency filter applied to the traces. The black arrow corresponds to the position of the fracture. Adapted from Tsoflias and Becker (2008).

The sensitivity of GPR reflection amplitudes to salinity was demonstrated by Tsoflias and Becker (2008). They analytically derived the changes of a GPR signal for several scenarios of fracture apertures and electrical conductivities of the fracture fluid (see Figure 1.6a and b). They simulated the change in a radar reflected signal on an isolated fracture in sandstone for different electrical conductivities of the fracture fluid. Figure 1.6c shows an increase in amplitude and phase lag with increasing electrical conductivity of the fracture filling fluid which was consistent with the experimental data (Figure 1.7). Figure 1.7 also shows that the main signal differences occur at GPR traveltimes that correspond to the arrival times of reflections at the fracture. Later arriving signals are also affected as those signals are transmitted two times across the subhorizontal fracture, but the relative differences are less pronounced. Changes in amplitude and phase for an identified fracture position can thus be related to fracture aperture and fluid electrical conductivity (Tsoflias and Becker, 2008).

1.8 Data integration methods in hydrogeophysics

The literature on data integration is manifold and I will only focus on hydrogeophysical applications. Data integration is of growing importance and lots of progress has been done in the past decade to combine different geophysical data with borehole logs, hydraulic and tracer test data (e.g., Gallardo and Meju, 2007; Linde *et al.*, 2006a; Tronicke and Holliger, 2005; Chen *et al.*, 2006; Williams and Johnson, 2004). At established field research sites, there are usually a series of different geophysical and hydrological data sets available that focus on the same target area. There are for example the Mirror Lake (e.g., Day-Lewis *et al.*, 2006), MADE (e.g., Zheng *et al.*, 2011) and Boise (e.g., Peterson Jr *et al.*, 1999) sites in the U.S.A., the Ploemeur site in France (e.g., Le Borgne *et al.*, 2007), Eggborough field site in the U.K.

(e.g., Binley *et al.*, 2002), and the Arrenaes file site in Danmark (e.g., Looms *et al.*, 2008), amongst others. Furthermore, computing power and versatile processing or inversion schemes have substantially improved to make data integration and joint inversion feasible, be it with the help of deterministic or stochastic approaches.

1.8.1 Deterministic methods

The most common way to integrate data is the separate processing and inversion of data and their subsequent combined interpretation (e.g., Looms *et al.*, 2008; Coscia *et al.*, 2011). The advantage is clearly in the independent treatment of different data, that can be individually tested and adjusted. Direct mapping (e.g., Hubbard *et al.*, 1997) from geophysical property estimates to hydraulic state variables can be done if petrophysical relationships are well established. For mapping of different lithological units, this approach might already be sufficient to answer the questions posed. Joint inversion approaches (e.g., Gallardo and Meju, 2007; Linde *et al.*, 2006b) can help to reduce model uncertainty if the combined data is complementary. Such approaches either assume functional relationships between hydrological and geophysical properties or impose a purely structural similarity between the models of different physical parameters during the inversion process. Constrained inversions are useful to invert data that are sensitive to bulk properties by constraining them to structural boundaries inferred from other data types (Doetsch *et al.*, 2012). A deterministic inversion searches for a single model that fit the data given their error characteristics and satisfies any other prescribed constraints (often that the model should be the smoothest possible). This model is then used to predict the system behavior. Even if deterministic inversions are most suitable for high dimensional problems, their usefulness is limited for highly non-linear problems, in that they rely on gradient information, that may make the algorithm getting trapped in local minima.

1.8.2 Stochastic methods

Inversion problems are typically complicated by a non-linear relationship between data and the parameters of interest, the problem's dimensionality, under-/over-determination of the model, noisy and dependent data, etc. The severity of these issues often makes deterministic algorithms ineffective if the results are to be used for uncertainty assessments. Stochastic approaches can be an alternative approach, as they explore the set of possible models that honor all imposed data constraints together with prior information and hence provide insights into the uncertainty of model parameters associated with the inversion result. Stochastic methods usually rely on some sort of Monte-Carlo sampling, that is, a random selection and evaluation of models from a prior set of models. In most stochastic inversion schemes, the selected models are analyzed with Bayesian statistics. Model parameters are treated as probabilistic variables having a joint posterior probability density function. The posterior distribution $p(\mathbf{m}|\mathbf{d})$ is described by Bayes' theorem as

$$p(\mathbf{m}|\mathbf{d}) = \text{const } p(\mathbf{m})L(\mathbf{m}|\mathbf{d}), \quad (1.21)$$

where $L(\mathbf{m}|\mathbf{d})$ is the likelihood function, $p(\mathbf{m})$ is the prior distribution of the models and $const$ is a normalizing constant $const = 1/\int L(\mathbf{m}|\mathbf{d})p(\mathbf{m})d\mathbf{m}$. The likelihood function describes the agreement between simulated and observed data \mathbf{d} for a given model \mathbf{m} . Instead of testing the model against all available data (consisting of different types $\mathbf{d} = (\mathbf{d}_1, \dots, \mathbf{d}_{ntype})$) at each iteration step of the algorithm, it can often be advantageous from a practical or computationally point of view, to condition the model sequentially to each data type \mathbf{d}_i . This assumes that the data errors of the different data types are uncorrelated. First, I will express equation 1.21 with the distinction of the different data types:

$$p(\mathbf{m}|\mathbf{d}) = const \, p(\mathbf{m}) \prod_{i=1}^{ntype} L(\mathbf{m}|\mathbf{d}_i) \quad (1.22)$$

The application of Bayes' theorem in stages leads to the expression, that has been proposed by Glaser *et al.* (2004) and Aines *et al.* (2002), among others:

$$p(\mathbf{m}|\mathbf{d}...\mathbf{d}_i) = const \, p(\mathbf{m}|\mathbf{d}...\mathbf{d}_{i-1})L(\mathbf{m}|\mathbf{d}_i) \quad (1.23)$$

The step-wise conditioning of models is favorable for applications in fractured rock, where for example the calculation of measures of system connectivity is much faster than the simulation of steady-state flow for a proposed fracture model, which in turn is much faster than that of transport under transient pressure conditions.

An explicit expression for the posterior probability density function is often impossible to obtain. The simplest approach to sample a distribution that is proportional to the posterior distribution is the rejection-acceptance sampling (e.g., Marjoram *et al.*, 2003), in which models are randomly sampled from the prior distribution and are being accepted proportional to their likelihood. The likelihood is calculated on a sampled model by calculating the difference between observational and simulated data. If this difference is within a predefined threshold, the model is accepted. This approach requires the choice of a metric to describe the difference between observational and simulated data. Further reading on this topic can be found in Marjoram *et al.* (2003), Mosegaard and Tarantola (1995), and Tarantola (2005).

One of the first applications of Monte Carlo methods in geophysics were done by Press (1968) and Anderssen and Seneta (1971). There are many studies that employ different stochastic approaches to hydrogeophysical data integration (e.g., Chen *et al.*, 2006, 2001; Chen and Rubin, 2003; Chen *et al.*, 2004; Subbey *et al.*, 2004; Dafflon *et al.*, 2009; Tronicke and Holliger, 2005; Glaser *et al.*, 2004; Day-Lewis *et al.*, 2000). Markov chain Monte Carlo (MCMC) methods are popular as higher acceptance rates can be expected compared to an exact sampler, such as pure rejection-acceptance algorithms. Glaser *et al.* (2004) developed a stochastic scheme that rapidly chooses among a very large number of hypothesized models and selects those that are consistent within the uncertainty ranges of all available information. By using MCMC they stochastically inverted for three-dimensional changes in electrical resistivity during a tank leak experiment (Ramirez *et al.*, 2005). Chen *et al.* (2006) developed a Bayesian

model and used a MCMC sampling strategy to estimate the probability of being in a zone of high hydraulic conductivity. Flowmeter data and seismic travel times were used to condition the models. They applied the technique to a densely fractured shale bedrock and could demonstrate that the resulting fracture zonations were consistent with results from bromide tracer breakthrough data and uranium biostimulation experiment. Other approaches are based on simulated annealing (e.g., Day-Lewis *et al.*, 2000) or genetic algorithms (e.g., Romero *et al.*, 2000) to generate model realizations. Day-Lewis *et al.* (2000) used simulated annealing to investigate high-permeability fracture zones by conditioning the models to borehole and hydraulic connection data. Tronicke and Holliger (2005) investigate how a simulated annealing approach can yield porosity distributions in the submeter range of an alluvial heterogeneous aquifers that are conditioned to neutron porosity logs and cross-hole georadar tomographic data. This approach was further improved by Dafflon *et al.* (2009).

1.9 The Stang-er-Brune test site

For the experimental studies described herein, the Stang-er-Brune site in Brittany, France, was chosen as a convenient field site due to different reasons. The site has been well-studied by different researchers mainly from the University of Rennes, University of Birmingham and the Massachusetts Institute of Technology (e.g., Le Borgne *et al.*, 2007; Ruelleu *et al.*, 2010; Belghoul, 2007; Touchard, 1999). The site is part of a long-term observatory for hydrogeological research in France. There are a series of data and different data types available. Moreover, the numerous previous experiences related to field specific experimental challenges were crucial to effectively design the experiments described herein. The site is part of a transmissive aquifer that constitutes the main water supply for the nearby town of Ploemeur, France, with a significant average extraction rate of 2,000 L/min (Le Borgne *et al.*, 2006). Our tracer tests were conducted ~ 3 km away from the water extraction site (Le Borgne *et al.*, 2007). The underlying crystalline formation consists of saturated granite overlain by highly deformed mica schists. The contact zone dipping 30° is at $z \approx 40$ m depth (Figure 1.8). At the site, three deeper boreholes (B1, 83 m deep; B2 and B3, 100 m deep) and some piezometers of 10 m depth were drilled in the formation. The granite formation has the most permeable fractures (Le Borgne *et al.*, 2007) and is therefore the area of primary interest in this study.

Belghoul (2007) and Le Borgne *et al.* (2007) used borehole log data and hydraulic testing (notably single-hole and cross-hole flowmeter tests) to characterize transmissive fractures that intersect the boreholes and identify those that are hydraulically connected. The formation is highly transmissive with overall hydraulic transmissivities on the order of 10^{-3} m²/s over the length of each borehole. The transmissive fracture network at the site is dominated by a relatively limited number of well-connected fractures (i.e., only 3-5 such fractures intersect a borehole over its entire length). The dips and azimuths of the boreholes suggest that there is no single fracture that intersects both boreholes B1 and B2 (Le Borgne *et al.*, 2007).

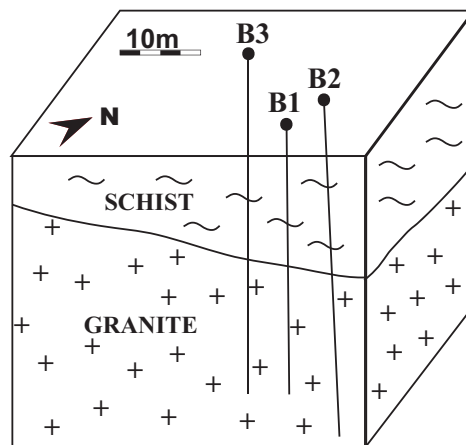


Figure 1.8: Simplified geological model of the field site at Stang-er-Brune.

1.10 Objectives and outline of the thesis

The main goals of this thesis are to investigate how GPR reflection data can be implemented to improve the characterization of fractured aquifers. The following objectives are to be addressed:

1. Improve the imaging of tracer movements in complex fracture systems using GPR reflection data and locate corresponding tracer flow paths.
2. Infer fracture network characteristics from a combined interpretation of hydrological and GPR reflection data.
3. Generate 3-D fracture models that are consistent with available hydrological and GPR imaging data.

The key characteristics to capture flow and transport dynamics for a fractured system (assuming impervious rock matrix) are the transmissivities of the individual fractures, the 3-D fracture geometry (position and size) and the connectivity between the fractures. Within this thesis, I try to improve the estimation of these characteristics by the integration of GPR imaging results with classical hydrological data. All following chapters present methodological studies, introducing new processing schemes and a data integration scheme. All methods are applied to the Stang-er-Brune site in France and are discussed in terms of their added value to the understanding of the local fracture network.

Chapter 2 introduces the strengths and challenges related to single- and cross-hole GPR reflection imaging. Here, multi-offset data was used to improve the signal-to-noise ratios of the data. Numerical modeling of cross-hole reflection data strengthen the interpretation of the cross-hole GPR reflection images.

Chapter 3 presents the use of GPR reflection data to monitor temporal changes in a complex fractured environment during tracer test conditions. The consistency of changes in GPR signals is discussed and compared to hydrological data that were simultaneously acquired.

In Chapter 4, the changes in GPR magnitudes are semi-quantitatively analyzed by modeling flow and transport in a simplified model that was build on the basis of GPR results. Temporal changes of GPR amplitudes corresponding to imaged fractures are compared to simulated relative changes in tracer concentrations. This study gives evidence that the GPR data can provide complementary information that help to determine the dynamics of tracer transport between the observation boreholes.

In Chapter 5, the previously processed, described and analyzed data are integrated in a stochastic inversion scheme to build 3-D connected discrete fracture network models. Hence, the fracture models are conditioned to all considered data, be it hydrological and geophysical. The set of possible models that is created allows to retrieve statistics of the conductive fracture network that dominates local flow and transport.

The Chapters 2, 3 and 4 are published as articles in peer-reviewed journals. The work presented in Chapter 5 is still in preparation and is soon to be submitted. I contributed as first author to all the work presented herein.

Chapter 2

Fracture Imaging Within a Granitic Rock Aquifer Using Multiple-Offset Single-Hole and Cross-Hole GPR Reflection Data

Caroline Dorn, Niklas Linde, Joseph Doetsch, Tanguy Le Borgne and Olivier Bour

published in *Journal of Applied Geophysics*¹

¹C. Dorn, N. Linde, J. Doetsch, T. Le Borgne, and O. Bour (2012). Fracture imaging within a granitic rock aquifer using multiple-offset single-hole and cross-hole GPR reflection data. *Journal of Applied Geophysics*, **78**, 123–132.

2.1 Abstract

The sparsely spaced highly permeable fractures of the granitic rock aquifer at Stang-er-Brune (Brittany, France) form a well-connected fracture network of high permeability but unknown geometry. Previous work based on optical and acoustic logging together with single-hole and cross-hole flowmeter data acquired in 3 neighboring boreholes (70-100 m deep) have identified the most important permeable fractures crossing the boreholes and their hydraulic connections. To constrain possible flow paths by estimating the geometries of known and previously unknown fractures, we have acquired, processed and interpreted multifold, single- and cross-hole GPR data using 100 and 250 MHz antennas. The GPR data processing scheme consisting of time-zero corrections, scaling, bandpass filtering and F-X deconvolution, eigenvector filtering, muting, pre-stack Kirchhoff depth migration and stacking was used to differentiate fluid-filled fracture reflections from source-generated noise. The final stacked and pre-stack depth-migrated GPR sections provide high-resolution images of individual fractures (dipping $30\text{-}90^\circ$) in the surroundings (2-20 m for the 100 MHz antennas; 2-12 m for the 250 MHz antennas) of each borehole in a 2-D plane projection that are of superior quality to those obtained from single-offset sections. Most fractures previously identified from hydraulic testing can be correlated to reflections in the single-hole data. Several previously unknown major near vertical fractures have also been identified away from the boreholes.

2.2 Introduction

The hydraulic response of fractured rock aquifers is largely governed by the spatial organization of permeable fractures. Identifying and characterizing individual permeable fractures or flow paths at the local field-scale (1-100 m) is an important and largely unresolved research goal for the hydrological and geophysical research communities (Long *et al.*, 1996; Day-Lewis *et al.*, 2006). Fractured rock masses are used worldwide, among others, for water supply purposes (e.g., Carruthers and Smith, 1992), as host rocks for environmentally hazardous waste (e.g., Mair and Green, 1981) and their characterization is necessary in rock fall prone areas (e.g., Spillmann *et al.*, 2007). Single-hole ground-penetrating radar (GPR) is a powerful technique to map potential permeable fractures and fracture zones away from boreholes and at large depths in relatively resistive rock (e.g., Olsson *et al.*, 1992; Hollender *et al.*, 2001), whereas surface GPR can be very useful down to some 10-20 m depth in sparsely fractured crystalline and metamorphic rock (Grasmueck, 1996). Borehole or surface-based time-lapse GPR experiments carried out during saline tracer tests, or combined interpretations of hydraulic data and borehole or surface-based GPR may identify larger m-scale fractures that are permeable and significantly contribute to the local fluid flow (Day-Lewis *et al.*, 2003, 2006; Talley *et al.*, 2005; Tsoflias *et al.*, 2001; Tsoflias and Becker, 2008).

Most previous work using single-hole GPR reflection data have used only one single-offset data from lower frequency antennas, such as 60 MHz, without migrating the data (see Spill-

mann *et al.* (2007) for an example of migrated single-offset high-frequency data). Hollender *et al.* (2001) illustrated that multiple-offset data can significantly improve the resolution of single-hole GPR sections. We expect that using high-frequency (100 and 250 MHz) multiple-offset data together with advanced processing will allow us to further improve the results of single- and cross-hole GPR investigations compared with those present in the literature. We also want to investigate to what extent cross-hole radar reflections complement single-hole reflection data. More importantly, the field-based results are expected to provide critical information about fractures that cannot be obtained from hydrological investigations alone.

Our field site is a well-studied hydrological research site located in a crystalline aquifer in Brittany (Stang-er-Brune, Figure 2.1a) in which Le Borgne *et al.* (2007) performed extensive hydrological testing and borehole logging. They concluded that the local conductive fracture network is dominated by only a few well-connected fractures (i.e., only 3-5 such fractures intersect a borehole over its entire length of ~ 90 m). High-resolution borehole images of the transmissive fractures show that these fractures have predominantly dip angles between 30° and 70° . The geometry of the hydrological connections between fractures are unknown. This is illustrated by apparent connections dipping up to 80° and that none of the permeable fractures appear to cross more than one borehole. The geometry of the permeable fracture network remains largely unknown as borehole data only provide detailed information in the close vicinity of the boreholes, whereas the single-hole and cross-hole flowmeter data provide information about connections, but not their geometry (Le Borgne *et al.*, 2006).

To better understand the geometry of potential flow paths by imaging single fractures at the site, borehole GPR experiments were carried out in June 2009 to image single fractures up to some 20 m from the boreholes. We acquired multifold single-hole and cross-hole GPR data in three boreholes (B1-B3, see Figure 2.1) using 100 MHz and 250 MHz antennas. This data are here used to determine the size, dip angles and to constrain the possible orientations of single fractures, especially for those that have not been previously identified, as they do not intersect the boreholes. We expect the strongest recorded GPR reflections to originate from the major open water-filled fractures (Tsoflias and Becker, 2008) and at the ~ 40 m deep contact between mica schist and granite (Figure 2.1).

In this contribution, we describe the processing of data acquired in borehole B1 (single-hole) and within the borehole-plane B1-B2 (cross-hole). We then present the final migrated sections including the boreholes B1-B3. The results are then interpreted together with available hydrological and borehole logging data.

2.3 General setting of the crystalline aquifer

Our field-site in Brittany (Stang-er-Brune), France, is located 3 km west of the main groundwater-pumping site of Ploemeur and is part of a long-term hydrological research observatory (<http://hplus.ore.fr>). The 3 deeper boreholes installed at the site reach depths from 80 to 100 m (water table during acquisition at ~ 1.5 m depth). The borehole deviations are up

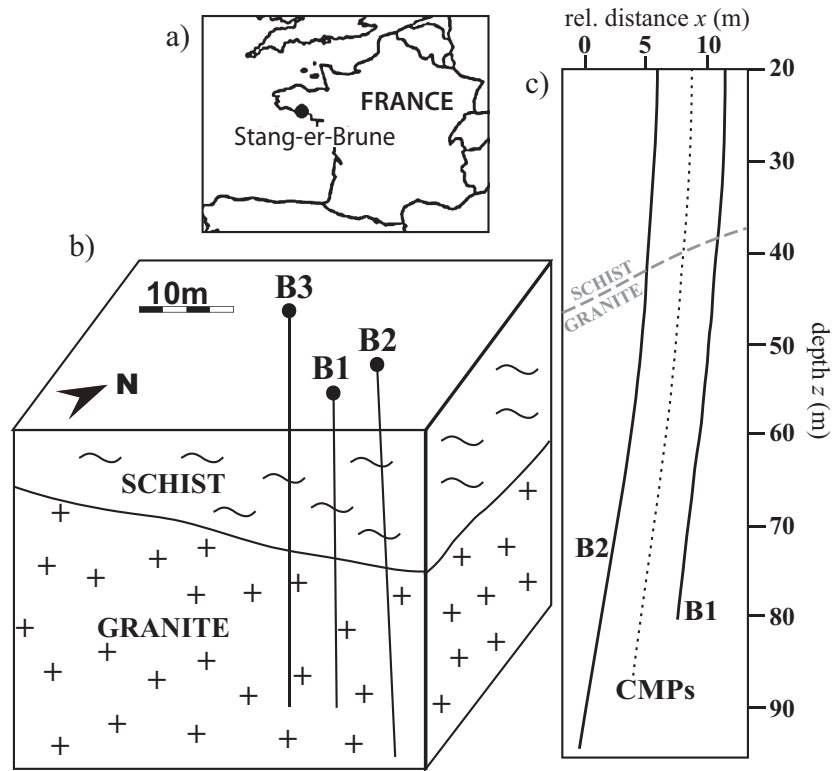


Figure 2.1: (a) Location of Stang-er-Brune, France. (b) Geological model of the field site showing the 30° dipping contact between mica schist and underlying granite. (c) 2-D projection of the borehole geometry of B1, B2 and cross-hole CMP (common midpoint) locations. At $z > 50$ m there is a relative dip between B1 and B2 of 3° .

to 6° from the vertical as estimated by a deviation probe using a three-axis fluxgate magnetometer for bearing and a three-axis accelerometer for inclination. This tool has an estimated uncertainty of 0.5° , which leads to an expected standard deviation of 0.9 m in the horizontal coordinates at 100 m depth. The characterization of fractures and the geology of the site are known from borehole coring (B1) and optical, acoustic, gamma-ray and electrical geophysical logs that are discussed in detail in Le Borgne *et al.* (2007) and Belghoul (2007). At a regional scale, the geology is characterized by low-porosity granite overlain by mica schists, with a contact zone dipping $\sim 30^\circ$ towards north (Touchard, 1999; Le Borgne *et al.*, 2006; Ruelleu *et al.*, 2010). The contact zone is relatively complex and consists of alternating deformed granitic sheets and enclaves of mica schists, pegmatite and aplite dykes (Ruelleu *et al.*, 2010). At the Stang-er-Brune site, we observe a part of this contact zone with mica schists in the first 30 to 40 meters overlying the Ploemeur granite. The formation is highly transmissive with overall transmissivity over the depth of each borehole varying around $10^{-3} \text{ m}^2/\text{s}$. This high transmissivity implies a strong connectivity of the permeable fractures that is probably related to the contact zone between the intrusive granite and the overlying mica schists.

2.4 Multifold data acquisition

Single-hole GPR data were acquired in all three boreholes (B1-B3) in common offset sections using 16 (4) different transmitter-receiver separations for the employed 100 MHz (250 MHz) antennas with a depth sampling of 0.15 m (0.1 m). The antenna offsets were equally distributed in the range of 2.3-11.3 m (100 MHz antennas) and 1.8-7.8 m (250 MHz antennas). The dominant frequencies are around 70 (140) MHz for the data acquired with the 100 (250) MHz antennas.

The cross-hole GPR data were acquired for all three borehole planes (B1-B2, B1-B3, B2-B3) in common transmitter gathers. The cross-hole planes of B1-B2 were acquired with 250 MHz antennas, whereas 100 MHz antennas were used for B2-B3 and B1-B3. Transmitters were spaced every 0.5 m and receivers every 0.1 m resulting in nominal 30-fold data at a common-midpoint (CMP) spacing of 0.125 m. The acquired offsets were restricted to those for which reasonable signal-to-noise ratio data could still be obtained.

To protect and to center the antennas in the boreholes, we attached two self-made plastic packers to each antenna, with a slightly smaller diameter than those of the boreholes (10.5 cm). Antennas were first positioned by transforming distances along the borehole measured with a trigger wheel into depths with the help of the deviation logs. Differential GPS was used to measure the top of the borehole casings. All depths are given relative to the top of the B1 casing. Time-zero measurements were performed when changing the antenna separation (single-hole) or after measuring 40 source-gathers (cross-hole).

2.5 Data processing

Significant ringing in the 250 MHz raw data and the dominance of the direct wave at early times, together with positioning uncertainties and radar wavespeed variations, resulted in numerous processing-related challenges. The processing scheme (Table 2.1) addressed these issues and resulted in high-quality GPR images of the surrounding fractured rock matrix. Even if the individual processes are standard in seismic imaging (Yilmaz, 2001), it was necessary to adapt the processing and the parameters to address the specific characteristics of the borehole GPR data.

We begin the description by first explaining the progressively improved radar wavespeed and borehole trajectory estimates before we outline the specific processing schemes used for single-hole and cross-hole data.

In the following, dips of reflectors are always given with respect to the surface assuming vertical boreholes if not mentioned differently. Note that shallow dips (relative to the surface) refer to steep dips of features relative to the subvertical borehole trajectories.

Table 2.1: Main processing steps of single- and cross-hole GPR data.

Representative Figure	Single-hole data processing	Cross-hole data processing	Representative Figure
	Static corrections	Static corrections	
2a →	AGC	AGC	
	Bandpass filter	Bandpass filter	
	F-X deconvolution	F-X deconvolution	
	Eigenvector filter	Eigenvector filter	
2b →	First-break mute	First-break mute	
2c, 3a →	Prestack depth migration	Dip-decomposition dip-moveout (includes stack)	7b ←
	Custom mute		7c ←
3d →	CMP Stack	Kirchhoff depth migration	

2.6 Radar wavespeed estimation and borehole trajectory estimation

The single- and cross-hole data were used together to define average radar wavespeed functions $v(z)$ and refine the estimated borehole trajectories. Isotropy of the radar wavespeed was assumed on the wavelength scale to allow for comparison of the single- and cross-hole data. This assumption is reasonable as granite is an igneous rock of low porosity having negligible intrinsic anisotropy.

An initial radar wavespeed model was obtained from the single-hole data by fitting a straight line to the slope of the corrected direct wave (which travels at the wavespeed of the rock in the vicinity of the borehole) travel times vs. transmitterreceiver distances for each CMP location. This procedure allows us to avoid static errors, resulting for example from the assumption that a finite-length antenna can be represented as a point source or by neglecting the delay of the direct wave in the water filled space between the antenna and the borehole. At $z > 40$ m, the differences between the radar wavespeed functions from all three boreholes are 2.5 % on average.

The first radar wavespeed estimates were subsequently refined by traveltime tomography. The mean of the 1-D radar wavespeed functions of each borehole pair for which tomography was carried out was used as initial and reference models in the tomography (green line in Figure 2.2a). The tomography was mainly carried out to improve the borehole positioning and to evaluate if the radar wavespeed estimates from the cross-hole data correspond with those determined in the vertical direction (i.e., assumption of isotropy). For the tomography, we followed the inversion procedure of Linde and Doetsch (2010) using a stochastic regularization operator based on an exponential isotropic covariance model with integral scales of 0.5 m aiming at fitting the data to an error level of 1.0 ns. The integral scale corresponds to the distance at which the spatial correlation has decreased to $1/e$. To decrease the sensitivity to

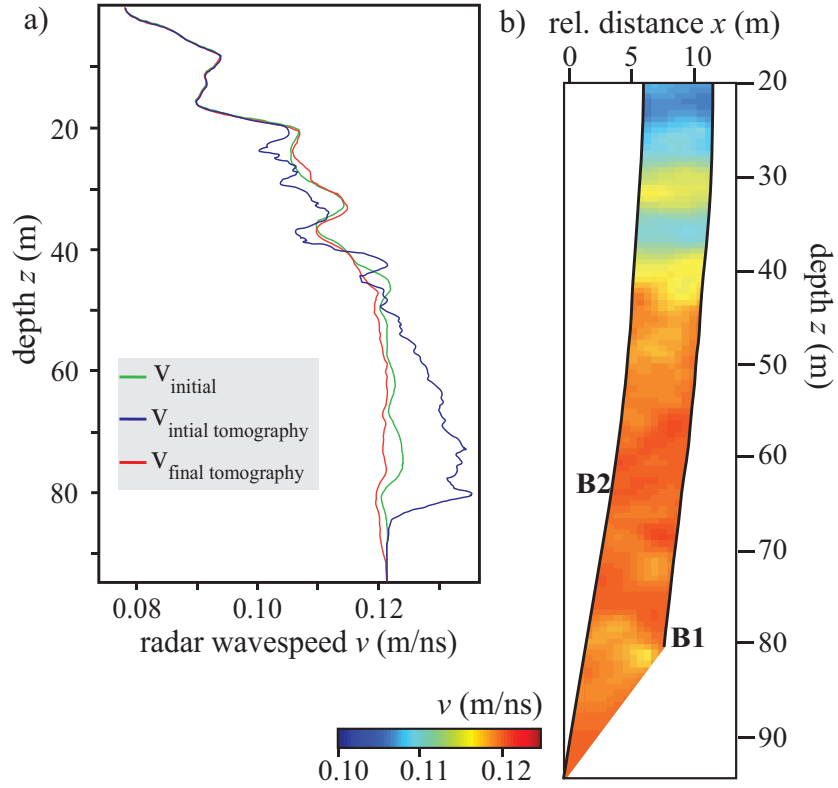


Figure 2.2: (a) 1-D radar wavespeed estimates for the plane B1-B2: (blue) after tomographic inversion of the cross-hole traveltimes using the initial borehole geometry and the initial radar wavespeed function (green) as starting and initial model, (red) after using the same tomographic inversion scheme but with final geometrical corrections applied. (b) Tomogram derived from first arrivals using the initial radar wavespeed function (a, green line) as starting and reference model and with final geometrical corrections.

noise in the data and to image sharp radar wavespeed variations we used a formulation based on iteratively reweighted least-squares (Farquharson, 2008).

Initial inversions of the cross-hole traveltimes in the plane B1-B2 resulted in suspiciously high radar wavespeeds at $z > 50$ m (blue line in Figure 2.2a) compared with the initial mean radar wavespeed function B1/B2 (green line in Figure 2.2a) indicating that the borehole spacing is smaller than indicated by the deviation logs. This inversion reached a final RMS error of 1.84 ns after 10 iterations. To improve the results it was necessary to correct the antenna positions in both the vertical and horizontal directions. For each transmitter gather, the receiver array was shifted vertically to minimise offset-correlated behaviour in the residuals. This correction (max. 0.5 m) was in all cases increasing with depth and helped to reduce small-scale variations in the resulting radar wavespeed models. Twisting of the antenna cables might have caused these errors.

To further constrain the distances between B1 and B2, we picked the observed prominent reflections originating from the adjacent borehole in the depth-migrated single-hole data (using the initial radar wavespeed function shown as green line in Figure 2.2a). We corrected for

the relative borehole geometry given the shape of the picked reflector distances. To correct for significant borehole deviation errors for the other cases where we could not identify reflections from the adjacent boreholes (B2-B3 and B1-B3), we tested horizontal correction factors that linearly varied with depth until the residuals (after the first iteration) have the lowest correlation possible.

The geometrical corrections and the subsequent inversion of the B1-B2 data resulted in the tomogram shown in Figure 2.2b with an rms error of 1.05 ns after 10 iterations. As expected, the traveltimes tomography provides no information about individual fractures but images large-scale radar wavespeed variations and trends. The final radar wavespeed model plotted in red in Figure 2.2a is based on the horizontal average of the tomographic model in regions with dense ray-coverage ($z = 20$ to 80 m) and the initial model outside this region. The final radar wavespeed estimates are mostly in the range of 0.09 ± 0.002 m/ns (mica schist) to 0.12 ± 0.002 m/ns (granite). Given the small lateral variations in the tomogram (Figure 2.2b), it appears that the assumption of a 1-D radar wavespeed function holds well if all applied corrections prior to the inversion are correct. These 1-D radar wavespeed functions were used to migrate the single- and cross-hole data.

2.7 Single-hole processing

2.7.1 Processing challenges

The GPR single-offset section (B1, 250 MHz antenna) in Figure 2.3a illustrates some of the data characteristics. Source-generated noise (N) or rather poor coupling within the antenna-borehole-rock system creates ringing effects parallel to the direct wave (D) but at later times. The ringing is most critical for the 250 MHz data, where it is superimposed on early reflections (R). The reflectivity pattern varies along the borehole and there is an abrupt increase in signal-to-noise ratios at approximately 40 m depth below the schist.

A general problem in single-hole GPR imaging with standard commercial omni-directional antennas (directional borehole antennas exists (e.g., Slob *et al.*, 2010) but are not widely used) is that the orientation of the fractures cannot be determined using data from one borehole alone. The data carries no information about the direction at which a reflection wavefront arrives at the borehole. Our processing and migration is therefore carried out under the assumption that the radar wavespeed varies only in the vertical direction (1-D radar wavespeed function $v(z)$, where z is depth). We showed in section 2.6 that the 1-D radar wavespeed assumption appears to hold well within the granite, which is of primary interest in this study as it is the host rock of the most permeable fractures.

Borehole logging data (optic and acoustic) and analysis of the retrieved core of B1 indicate that the shallowest dips of transmissive fractures are in the range of 30° (except one fracture dipping 15° ; Le Borgne *et al.* (2007)). Using migration methods to image such subhorizontal dips (steep dips with respect to the observation line) require an accurate radar wavespeed model.

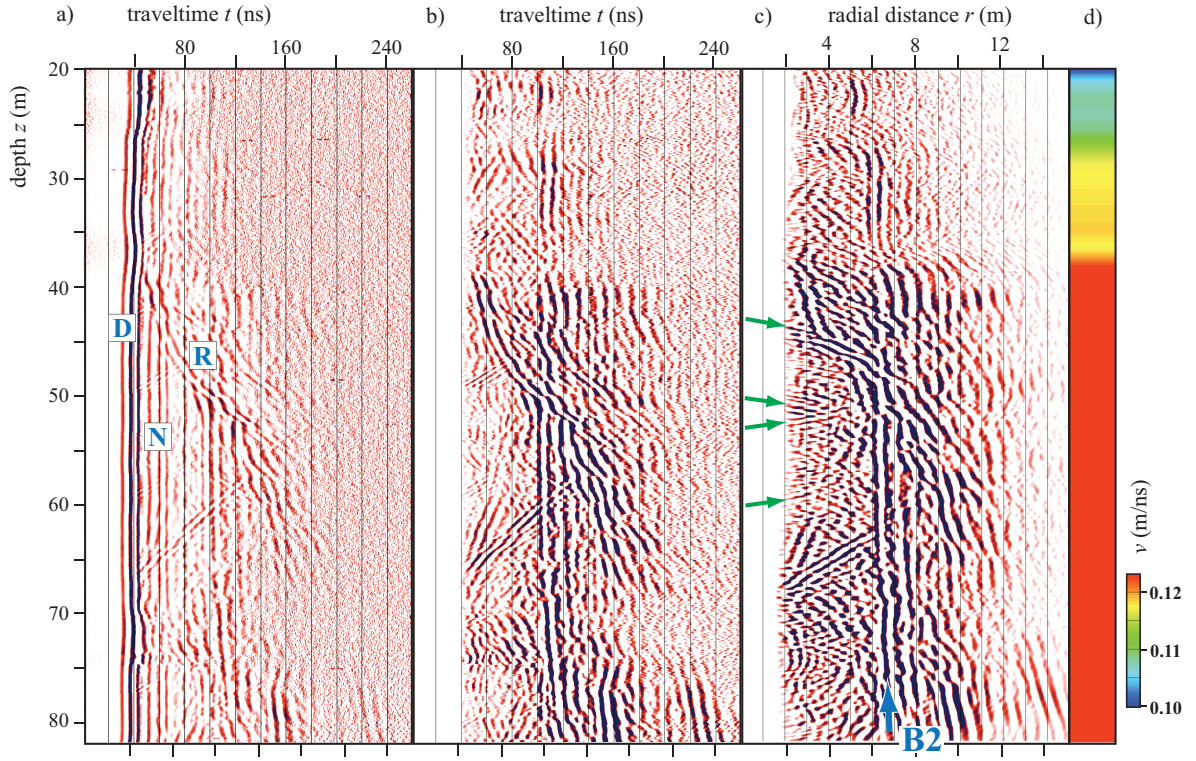


Figure 2.3: Results of pre-stack processing applied to a typical common-offset section of B1 (3.8 m offset, 250 MHz antennas). (a) Section with applied static corrections and an AGC of 70 ns window length. Letters indicate regions dominated by: D direct wave; N source-generated noise (ringing); R - reflections. (b) As in (a) but after application of bandpass filter, F-X deconvolution, eigenvector filter and custom mute (see text). (c) As in (b) but after pre-stack depth migration (the axis aspect ratio $r:z$ is 2:1). The blue arrow in (c) indicates reflections generated from the adjacent borehole B2; the green arrows refer to features discussed in the text. (d) 1-D wavespeed model for depth migration in (c).

2.7.2 Pre-stack time-domain processing

Table 2.1 lists the main single-trace and multi-trace filter and deconvolution tools that were applied to the single-offset data. All parameters within the processing sequence were chosen to account for the different frequency contents of the 100 and 250 MHz data.

Corrections were carried out to account for inaccuracies in the data acquisition sampling frequency (c.f., Hollender *et al.*, 2001), drifts in the time-zero and geometrical positioning errors. After appropriate scaling (Figure 2.3a), reflections (R) had to be enhanced and separated from the direct wave (D) and ringing noise (N), resulting in a common single-offset section as shown in Figure 2.3b. Bandpass filtering (30-270 MHz for the 250 MHz data, 20-130 MHz for the 100 MHz data) removed low and high frequency noise from the data. F-X deconvolution increased reflection coherency by reducing random noise without introducing noticeable artifacts. For the 250 MHz data, an eigenvector filter was applied in a window around the direct wave to remove energy parallel to the direct wave mainly containing ringing noise (N). Residual energy that appears earlier than the direct wave is muted afterwards.

2.7.3 Pre-stack depth migration and stacking

Pre-stack Kirchhoff depth migration of single-offset sections provided high-quality image reflections with overlapping features and a wide dip angle range (Figure 2.3c). The migration radar wavespeeds used are in the range of 0.09 m/ns (mica schist) to 0.12 m/ns (granite). In section 2.7, we describe how we estimated the radar wavespeed function.

We used a migration method that computes first arrivals through an implicit Eikonal solver. The amplitudes are neither calculated nor meaningful as the processing is based on a monopole (point) radiator, which does not correspond well with the dipole-like radiation characteristics of borehole antennas. In regions without significant radar wavespeed variations (40-100 m), subhorizontal dipping features (down to 30°) are well preserved after migration (green arrows in Figure 2.3c). Migration artifacts are likely to be present around $z = 40$ m (Figure 2.3c) since the 1-D radar wavespeed model does not account for the 30° dip angle of the mica schist-granite contact. Apart from this region, extensive comparisons of migrated sections using a variety of radar wavespeed models indicate that the sections are free of major migration artifacts.

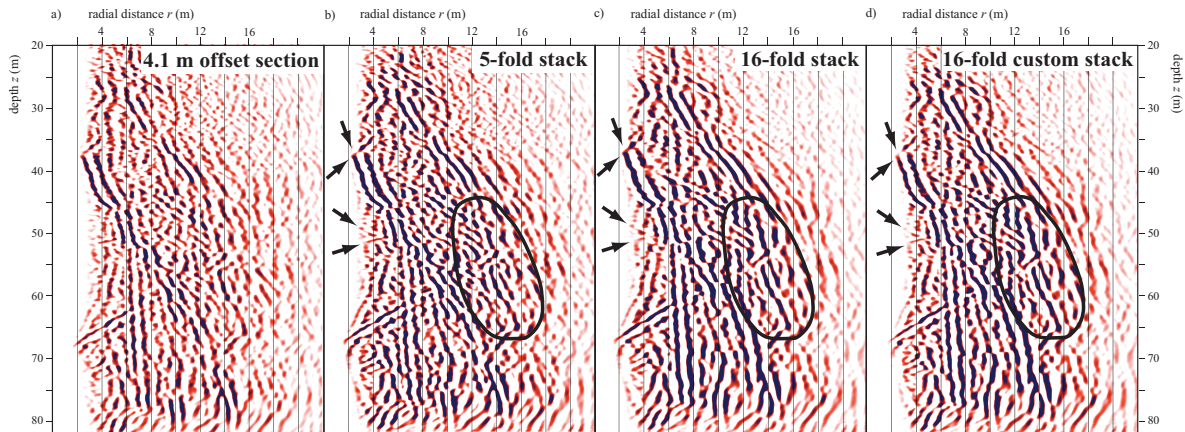


Figure 2.4: Illustration of the improved signal-to-noise ratios offered by stacking the migrated images of B1 (100 MHz data). (a) Single-offset section with 4.1 m antenna separation. (b) Stack of the 5 shortest antenna separations, (c) all 16 offset sections, and (d) as in (c) but with a custom mute applied for each offset section before stacking. Note that subhorizontally dipping events at small radial distances are best imaged in (b) and (d) (see arrows), whereas at larger radial distance they are best imaged in (c) and (d) (see ellipses).

Stacking the migrated single-offset sections of the 100 MHz data significantly improved the quality compared to individual single-offset sections (compare Figure 2.4a and c). Close to the borehole, subhorizontal dipping features (e.g., $\sim 30^\circ$) are less well imaged at larger antenna offsets (see arrows in Figure 2.4b and c). Further away from the borehole, reflections from subhorizontal dipping features of limited extent are best recognized at larger antenna offsets (see ellipses in Figure 2.4b and c). The image quality increases for larger radial distance $r \gtrsim 8$ m by adding information from larger offset sections, but decreases for $r \lesssim 6$ m. To avoid

sub-optimal resolution close to the boreholes in the final image, we applied an offset-dependent top mute prior to stacking (Figure 2.4d); the larger the offset the longer the applied top mute.

For the 250 MHz data we stacked the three largest offset sections, since the shortest offset (1.8 m) sections were highly contaminated by ringing effects and did not contribute significantly to the stacked images. The major improvements of stacking the 250 MHz data came from the additional offset information and less from an increased signal-to-noise ratio, given that only a few offsets were used. We do not image any features at distances $r < 2$ m because of the dominance of the direct wave at early times and its subsequent removal, which also tends to remove superimposed reflections at early times. This complicates direct comparisons with the borehole logging data.

2.8 Cross-hole processing

2.8.1 Challenges

Common cross-hole processing tools such as single-trace mapping techniques (Khalil *et al.*, 1993; Lazaratos *et al.*, 1995) that focus on layered structures can only handle horizontal to sub-horizontal reflectors correctly. The complex spatial distribution of fractures at the site and the cross-hole acquisition geometry necessitate an approach that can accurately consider all reflector dips.

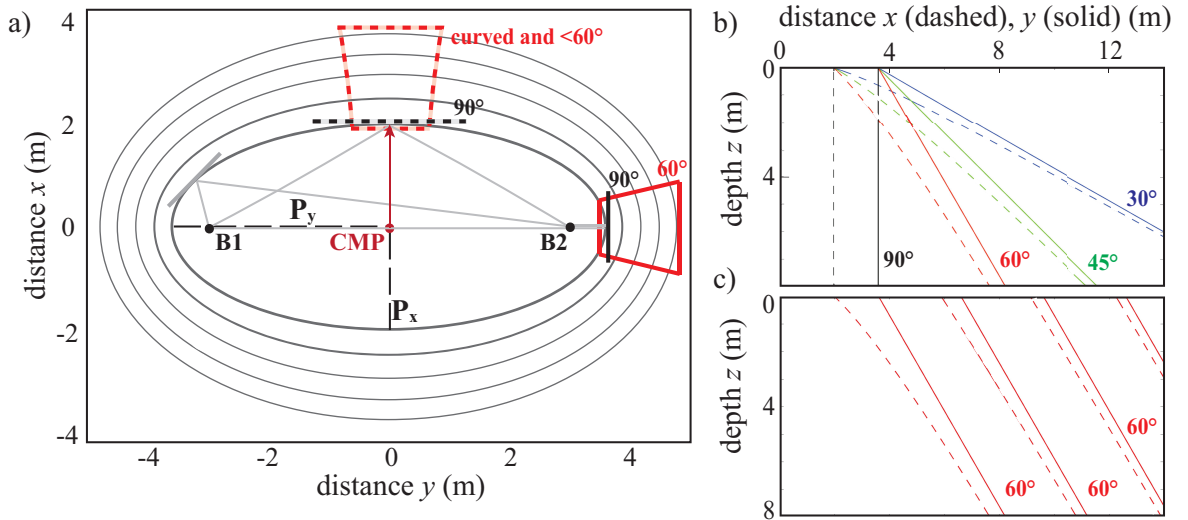


Figure 2.5: (a) 2-D-schematic of elliptic distance projection in cross-hole reflection imaging showing boreholes B1 and B2 from a birds eye view. A 90° dipping reflector at a distance $x = P_x$ in the depth-migrated GPR image can originate from anywhere on an ellipse described by the two main axes P_x and P_y surrounding the CMP. (b) and (c) Dip and distance representations in the depth-migrated images. The solid lines describe tangential reflector planes striking perpendicular to the inter-borehole plane and dipping at angles 30° , 45° , 60° and 90° (see solid lines in (a) of both 90° and 60° dipping planes). The dashed lines describe how they would appear in a depth-migrated image (see dashed lines in (a) of plane representations).

Unlike the cylindrical symmetry of the single-hole data, reflections in the cross-hole sections can originate from any point on an ellipsoid around a respective CMP location (Figure 2.5). Some analysis is therefore needed to better understand how to migrate such data and interpret the results in terms of possible dip angle and distance ranges. For this geometry, any signal traveling between the two boreholes B1 and B2, being reflected on a 90° dipping plane at $y = P_y$ (Figure 2.5a) cannot be distinguished from any other reflection on the ellipse described by the two main axes P_x and P_y . In the depth-migrated image this plane would show up at a shorter distance $x = P_x$. A reflector plane at $y = P_y$ dipping 60° away from the borehole (see solid red lines in Figure 2.5a-c) is imaged in the depth-migrated section as a curved feature (see corresponding dashed red lines in Figure 2.5a-c).

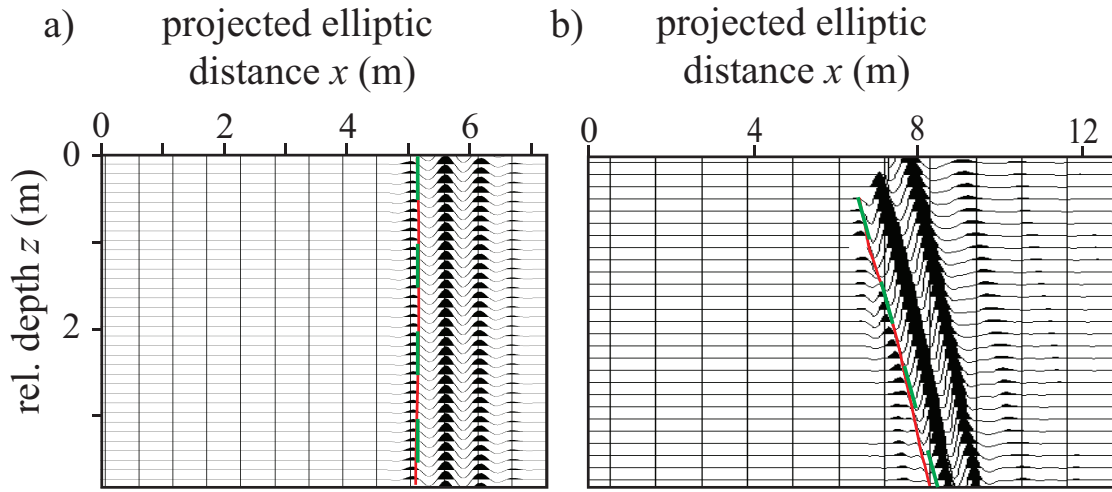


Figure 2.6: (a) Modeled depth-migrated seismic data for a borehole geometry as in Figure 2.5a and a 90° dipping reflector plane at $y = 5.9$ m away from the CMP. The picked (red line) and predicted distances (green line) are both $x = 5.1$ m. (b) As for (a), but for a modeled reflector plane dipping 60° away from the surface.

To simulate the geometrical effects of the examples described above (90° and 60° dipping reflector), we have computed synthetic seismograms for the B1/B2 borehole geometry using the 3-D viscoelastic finite difference modeling code of Bohlen (2002) (Figure 2.6). An alternative would have been to use a 3-D GPR code (e.g., Giannopoulos, 2005). The use of synthetic seismograms can help to explain the GPR reflection geometry, but not the GPR amplitudes. The modeled and depth-migrated data confirms our geometrical assumption of an elliptic projection. Calculated and observed distances in the depth-migrated image fit well. Figure 2.6b confirm that planar features might appear curved in the migrated sections.

Due to the removal of the direct wave that strongly contaminated early reflections, the earliest reflections that are possible to image originate from an ellipse (see ellipse in Figure 2.5a) in a range from 2 to 4 m away from the CMP.

2.8.2 Processing

The pre-processing of the cross-hole data was similar to that of the single-hole data (section 2.6) but was followed by dip decomposition DMO and depth migration (Table 2.1). The NMO stack (Figure 2.7a) performed with the dip-independent stacking wavespeeds (Figure 2.2a, red line), reveals some structural complexity but fails to clearly image subhorizontal dipping reflectors superimposed on subvertical features. We treated the preprocessed data with a dip-moveout (DMO) algorithm based on Jakubowicz (1990) that distinguishes and processes events on the basis of dip, with angles between 0° and 90° discretised into 45 different values. For each of the 45 dip angle values, the CMP gathers were NMO corrected using appropriate velocities estimated from the dip-independent wavespeeds based on standard formulas and then stacked. Finally, all 45 dip-filtered stacks were summed together to form a DMO-corrected stack (Figure 2.7b). Compared to the NMO stack, the DMO process improved signal-to-noise ratios throughout the section and conflicting dips are better imaged (see rectangles in Figure 2.7a and b). Other tested DMO algorithms did not sufficiently image subhorizontal dips (e.g., common-offset F-K DMO).

The migrated section (Figure 2.7c) was obtained by a post-stack Kirchhoff depth migration for steep dips (in this context steep refers to dips with respect to the observation line, Table 2.1) using the same implicit Eikonal solver as for the single-hole data. This allowed us to obtain images that were free of major artifacts. We decided to use partial pre-stack migration followed by post-stack depth migration because it showed the least migration artifacts in comparison with pre-stack-migration schemes performed on the modeled cross-hole seismograms (see also Figure 2.6).

2.9 Results

2.9.1 Single-hole GPR images

The final stacked and migrated sections of B1-B3 show several linear reflections (dipping 30° - 90°) located at 2-14 m and 2-20 m radial distance for the 250 MHz (Figure 2.8) and 100 MHz (Figure 2.9) data. These reflections are expected to mainly originate from individual fractures and fracture zones. The sections obtained from the 100 and 250 MHz antennas are comparable as most prominent features in the 250 MHz section are also represented in the 100 MHz section. The higher resolution of the 250 MHz data at $r < 8$ m allows more structural details to be imaged, especially for subhorizontal dipping features. The change from low to high reflectivity at $z = 38$ m in B1 ($z = 42$ m in B2, $z = 35$ m in B3) is related to the higher attenuation in the more conductive overlying mica schist compared to the granite.

The prominent sub-vertical reflections at $r \sim 6$ m (arrows B2 and B1 in Figures 2.8 and 2.9) correspond to the neighboring borehole. Identical reflector planes can be recognized in both B1 and B2 GPR sections as having similar dips and corresponding depth ranges. We can also distinguish reflections originating from outside the borehole plane B1-B2 from reflections

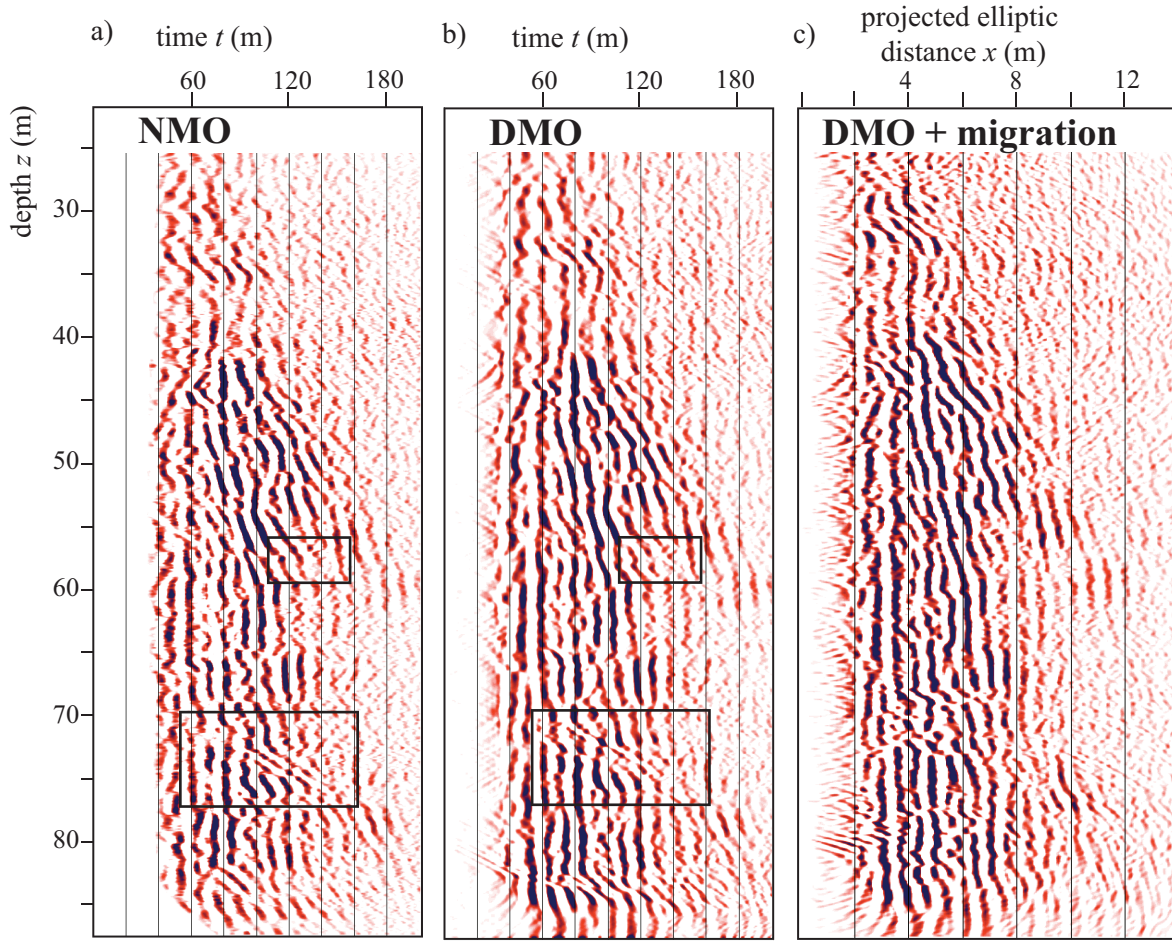


Figure 2.7: Post-stack processed cross-hole section for B1-B2. (a) NMO stack, (b) dip-decomposition DMO stack and (c) post-stack Kirchhoff depth-migrated version of (b) based on radar wavespeed model shown in Figure 2.2a (red line). Black rectangles refer to features discussed in the text.

generated between the boreholes. Reflections originate from outside the plane B1-B2 if the imaged reflections have similar dip angle and dip direction for both single-hole sections (see A1 in Figure 2.8). Reflections originate from within the borehole plane if they have similar dips but the dip direction appears different comparing both single-hole sections (see A2 in Figure 2.8).

A series of transmissive fractures previously identified at their intersection with the boreholes and characterized through flowmeter tests and optical logging (Le Borgne *et al.*, 2007) can be correlated to reflections in the GPR sections (blue letters in Figures 2.8 and 2.9) based on their dips and extrapolated intersection points given positioning errors of up to 4%. Fractures that could not be correlated to GPR reflections either lie in the mica schist (B1-1) where signal-to-noise ratios are low, have a nearly horizontal dip and hence cannot lead to direct reflections (B1-4 in Figure 2.8a: probable phase shift on reflections due to B1-4) or have a too small spatial extent to be seen at $r > 2$ m (B3-2 and B2-2 are only seen up to $r = 4$ m in

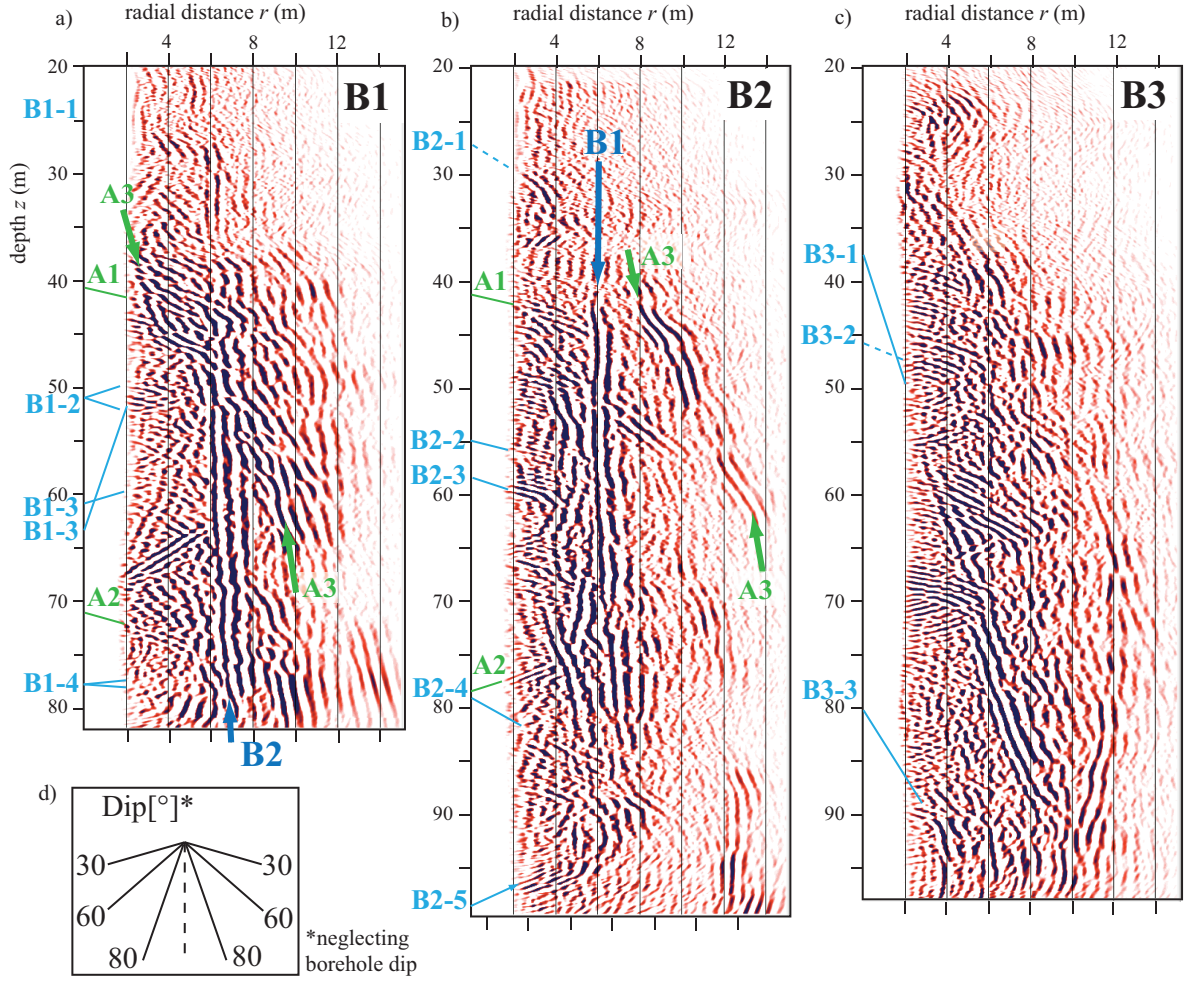


Figure 2.8: Processed and pre-stack depth-migrated single-hole GPR data acquired with the 250 MHz antenna in (a) B1, (b) B2, and (c) B3. Blue letters refer to transmissive fractures observed in the boreholes from optical logs and flowmeter tests (Le Borgne *et al.*, 2007), green letters refer to additional features discussed in the text. The radial distance r indicates distances away from the respective boreholes. Note the lack of information at $r < 2$ m due to the direct wave removal. (d) Dip angles corresponding to the axis aspect ratio $r:z$ of 2:1. Note that a given dip (0-90°) can be imaged with two different dip directions (e.g., A2).

Figure 2.8 but are not clearly seen in the 100 MHz data in Figure 2.9). A number of hitherto unknown prominent subvertical features can be seen that do not cross the boreholes. As an example there is a larger fracture zone (A3) dipping $\sim 70^\circ$ that is crossing the sections B1 and B2 at $r = 2$ -10 m.

2.10 Discussion

Multiple-offset data acquisition together with a tailored pre-processing and pre-stack migration made it possible to correlate most transmissive fractures observed in flowmeter and optical televiewer data (Le Borgne *et al.*, 2007) with reflectors observed in the single-hole reflection

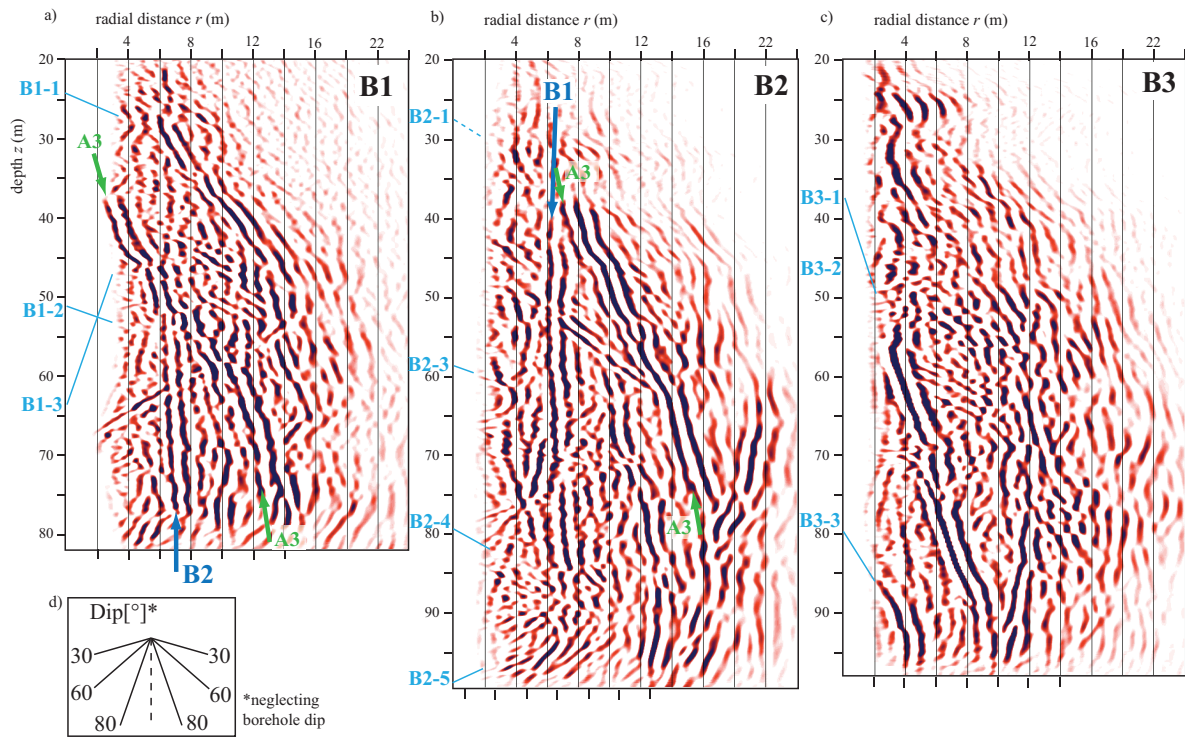


Figure 2.9: The same borehole sections as in Figure 2.8 but for the processed and pre-stack depth-migrated GPR data that were acquired with the 100 MHz antenna. Section (a) is identical to Figure 2.4d.

data (Figures 2.8 and 2.9). In fact, a total of 10 out of 11 transmissive fractures in the granite could be correlated with reflectors. These reflections appear as (sub-) linear features in the final processed and migrated images. Reflectors crossing the boreholes were best identified by first picking reflectors from the migrated 250 MHz data (Figure 2.9) followed by verification that these reflectors are visible on individual unmigrated time-sections. The dip angles of the reflectors and those observed in the boreholes were allowed to have a mismatch of up to 10° as fractures/reflectors that appear linear on the scale of the fracture might locally (i.e., where they cross the boreholes) show larger deviations in the dip angle as evidenced at outcrops of similar patterns on the coastline 5 km away. Most transmissive fractures can be correlated with reflectors, but there are also certain reflectors that appear to cross the boreholes that are unrelated to the previously identified permeable fractures. One important result is that we can associate a length scale to previously identified transmissive fractures.

The migrated single-hole (Figures 2.8 and 2.9) and cross-hole (Figure 2.10) data image several prominent fractures or fracture zones with lengths exceeding 40 m. Only one of those (B3-1 in Figures 2.8c and 2.9c) appears to cross the borehole. It is important to note that the anisotropic radiation/reception patterns of the antennas make subvertical dipping features in the single- and cross-hole data more prominent compared to shallow ones because the electric dipole source has its orientation in the vertical direction. Furthermore, imaging limitations at large distances away from the boreholes make it impossible to trace the full length of the more

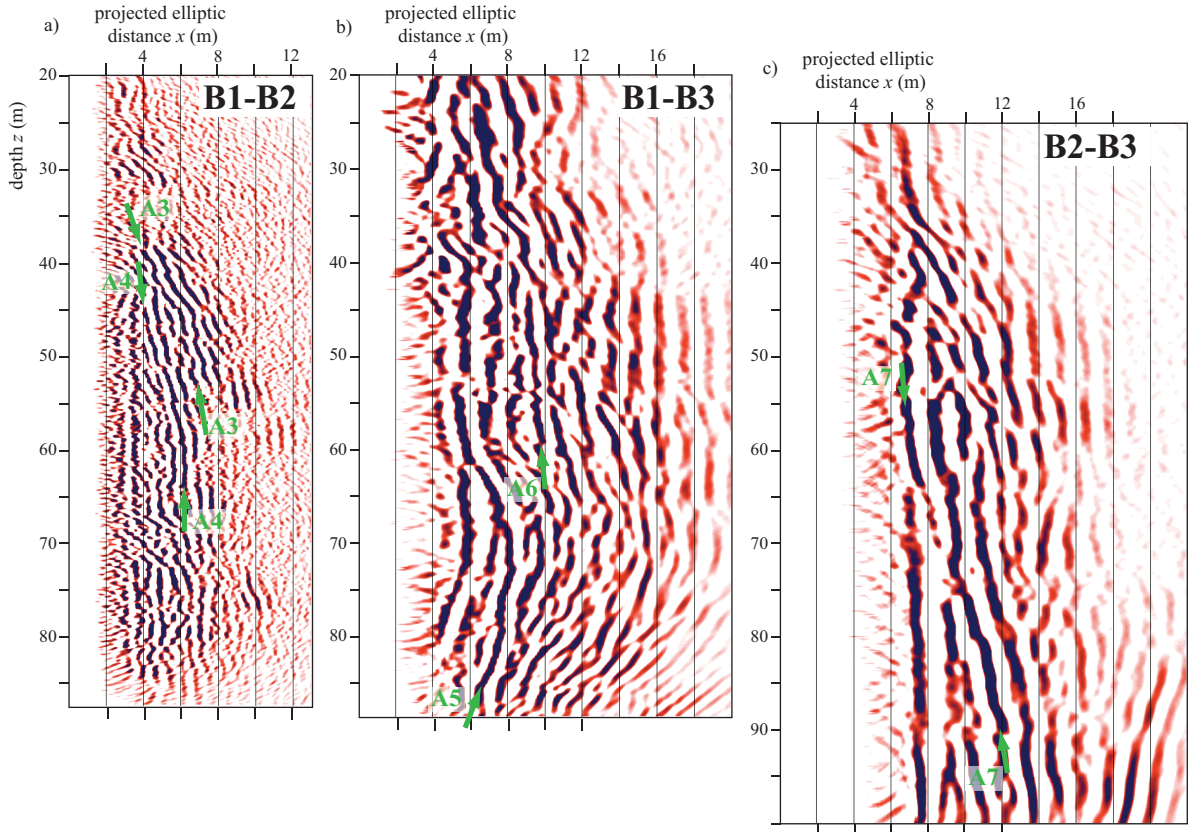


Figure 2.10: Processed and migrated cross-hole GPR sections of (a) B1-B2 (250 MHz), (b) B1-B3 (100 MHz), and (c) B2-B3 (100 MHz). A3-A7 refer to features discussed in the text. The projected elliptic distances x are relative to the CMP locations as shown for B1-B2 in Figure 2.1c. The axis aspect ratio $x:z$ is 2:1. Note the lack of information at $x \lesssim 2$ m due to the direct wave removal. Note also that dipping individual fractures that are expected to be linear show up as curved features in accordance with Figure 2.5b and c.

subhorizontal dipping reflectors. It is possible that the previously unknown subvertical fracture zones play an important role in (1) establishing the hydraulic connections observed and (2) providing sustained yield during pumping. This interpretation is supported by Le Borgne *et al.* (2007) who demonstrate that none of the identified permeable fractures appear to cross more than one borehole. Furthermore, steady-state conditions are established almost instantaneously at this site, which indicates a well-connected fracture network extending over a large scale. Some of these major reflectors can be imaged from different boreholes and with the cross-hole data (Figures 2.8-2.10). Consider A3, as it is imaged in both B1 and B2 single-hole data, and in the B1-B2 cross-hole data, it is possible to better constrain its location (e.g., Olsson *et al.*, 1992; Spillmann *et al.*, 2007).

Saline tracer tests monitored with single-hole GPR data will in the future be analyzed to test the conceptual model invoked above. It is also expected that such experiments will decrease the inherent uncertainty caused by projecting 3-D data into 2-D as the injection point is known.

2.11 Conclusions

GPR is one of few geophysical methods that are capable of imaging individual millimeter wide fractures away from boreholes. We have processed and interpreted multiple-offset single-hole and cross-hole GPR data acquired in a granitic rock aquifer. The multiple-offset acquisition not only increased the CMP fold, but also made it possible to image fractures with limited extents and dip angles for which reflections are only visible within a certain offset-range. Our processing scheme allowed us to separate useful reflections from unwanted signals to obtain high-resolution images. Key processing steps included time-zero and geometrical corrections, eigenvector filtering to remove direct wave and ringing effects, careful top muting and migration, and accurate radar wavespeed estimation and borehole positioning by a combined analysis of single- and cross-hole data. The migration (using pre-stack depth migration or DMO-corrections followed by depth migration) was able to handle subhorizontal dips and provided images that were free of major artifacts. The superposition of reflections necessitate a combined interpretation considering both unmigrated and migrated data.

The final GPR sections image a number of reflectors with dips in the range of $30\text{-}90^\circ$ at radial distances of 2-20 m and spatial extents of more than the first Fresnel-zone (2 m at $r = 20$ m down to 0.6 m at $r = 2$ m). Reflections from a certain reflector can be observed if a normal-vector to the reflector exists which crosses the borehole. We observe the highest resolution in the vicinity of the borehole when using the 250 MHz data, whereas the 100 MHz data are very useful in imaging major subvertical features away from the borehole. These mostly linear reflections are interpreted as mainly corresponding to fractures, but are also due to other boreholes and the contact zone between mica schist and granite. Ten out of eleven known transmissive fractures in the granite can be correlated to reflections. By identifying the same reflectors in different borehole GPR sections, we can reduce the inherent 360° circular uncertainty of single-hole data and elliptical uncertainty of cross-hole data to some extent. The dip direction of identified fractures remains underdetermined because the three boreholes do not form a triangular prism at depth, but rather lie on a common plane. Prominent subvertical reflectors image previously unknown fractures (they do not intersect the boreholes) with lengths exceeding 40 m that may play a key role in determining the flow geometry at the site.

Chapter 3

Single-Hole GPR Reflection Imaging of Solute Transport in a Granitic Aquifer

Caroline Dorn, Niklas Linde, Tanguy Le Borgne, Olivier Bour and Ludovic Baron

published in *Geophysical Research Letters*¹

¹C. Dorn, N. Linde, T. Le Borgne, O. Bour and L. Baron (2011). Single-hole GPR reflection imaging of solute transport in a granitic aquifer. *Geophysical Research Letters*, **38**, L08401, doi: 10.1029/2011GL047152.

3.1 Abstract

Identifying transport pathways in fractured rock is extremely challenging as flow is often organized in a few fractures that occupy a very small portion of the rock volume. We demonstrate that saline tracer experiments combined with single-hole ground-penetrating radar (GPR) reflection imaging can be used to monitor saline tracer movement within mm-aperture fractures. A dipole tracer test was performed in a granitic aquifer by injecting a saline solution in a known fracture, while repeatedly acquiring single-hole GPR sections in the pumping borehole located 6 m away. The final depth-migrated difference sections make it possible to identify consistent temporal changes over a 30 m depth interval at locations corresponding to fractures previously imaged in GPR sections acquired under natural flow and tracer-free conditions. The experiment allows determining the dominant flow paths of the injected tracer and the velocity (0.4-0.7 m/min) of the tracer front.

3.2 Introduction

Identifying and characterizing individual permeable fractures and corresponding flow paths at the local field-scale (1-100 m) is an important, but largely unresolved problem with implications for designing waste disposals (nuclear, toxic waste, CO₂) and extraction of natural resources (oil, gas, heat, water). Hydrogeological investigations of fractured rock are commonly based either on local measurements in the vicinity of boreholes or hydraulic or tracer inference testing that provides low-resolution integrated information between boreholes or packed-off borehole intervals. Geophysical techniques and imaging methods make it possible to spatially resolve temporal changes at intermediate scales away from boreholes (e.g., Rubin and Hubbard, 2006).

Surface-deployed GPR reflection data (Talley *et al.*, 2005; Tsoflias and Becker, 2008; Becker and Tsoflias, 2010) has been successful in imaging saline tracers in individual sub-horizontal fractures, but such experiments are limited to depths of some tenths of meters even under ideal conditions. Cross-hole difference-attenuation radar tomography (e.g., Liu *et al.*, 1998; Day-Lewis *et al.*, 2003) can image bulk changes caused by tracer movement through fracture zones at larger depths, but the resolution of the resulting tomograms is insufficient to image the transport in individual mm-aperture fractures. Lane Jr *et al.* (1996) demonstrated significant temporal changes between single-hole GPR reflection data acquired before and after a steady-state saline tracer experiment at Mirror Lake, New Hampshire.

Saline tracer injections increase temporarily the electrical conductivity of the fluid within the fractures contributing to tracer movement and within the pumping boreholes. GPR reflections vary with fluid conductivity, as it affects (1) GPR reflection/transmissivity coefficients at rock-fluid interfaces of fractures and boreholes (e.g., Tsoflias and Becker, 2008), and (2) the frequency-dependent attenuation within the fluids (e.g., Liu *et al.*, 1998). To compare GPR reflections at different observation times, it is necessary to correct for variations in the effective source wavelet that are due to increased fluid conductivity in the observation borehole.

We present single-hole GPR monitoring results acquired during a dipole (injection-extraction) tracer experiment in a well-studied granitic aquifer (Le Borgne *et al.*, 2007). The main differences with the work of Lane Jr *et al.* (1996) is that (1) we perform a pulse injection to determine the velocity of the tracer front, (2) we account for time-varying electrical conductivity in the observation borehole and associated changes in the ringing noise characteristics, and (3) we perform depth-migrations of the difference data. To the best of our knowledge, this is the first time tracer transport in a network of connected fractures has been imaged using single-hole GPR reflection monitoring. Our results are compared with migrated single-hole GPR reflection sections (Dorn *et al.*, 2012a) acquired under natural flow and tracer-free conditions to determine which of the imaged fractures that transport the saline tracer and how these fractures are inter-connected.

The objectives of this paper are to show that single-hole GPR reflection data combined with saline tracer experiments make it possible to (1) monitor tracer transport in individual fractures, (2) obtain high-resolution depth-migrated images of tracer displacement, and (3) retrieve site-specific information about the geometry and hydrological connections of the main transport pathways.

3.3 Field site and experiment

The tracer test was carried out in a saturated and sparsely fractured (less than 1 open fracture per meter) granite formation close to Ploemeur, France (Le Borgne *et al.*, 2007). We used two 6 m spaced boreholes B1 (80 m deep) and B2 (100 m deep) that reach a contact zone at $z \approx 40$ m depth ($z = 0$ m corresponds to the top of the borehole casing) between porous mica schist and underlying low-porosity granite, which is the formation of interest in this study.

Single- and cross-hole GPR reflection data acquired under natural flow conditions (Dorn *et al.*, 2012a) constrain the geometry of the main fractures (midpoint, minimum extent of fracture, fracture dip) within the granite at radial distances $r = 2 - 20$ m away from the boreholes. Additionally, borehole logging (optical, acoustic, gamma-ray and resistivity logs) and hydraulic testing characterized fractures that intersect the boreholes and identified those that are hydraulically connected. The formation is highly transmissive with overall transmissivities over the length of each borehole on the order of 10^{-3} m²/s. Le Borgne *et al.* (2007) found that the local conductive fracture network is dominated by only a few well-connected fractures (i.e., only 3-5 such fractures intersect a borehole over its entire length), but no single fracture appears to connect B1 and B2.

In the injection well B2, 94 L of saline tracer (50 g NaCl/L, initial tracer salinity is 30 times higher than the background salinity) were injected during 11 minutes at a rate of 8.5 L/min within a transmissive fracture at $z = 55.6$ m that was isolated from lower-lying fractures using a packer system. After the injection, we continued to push the tracer with fresh water at the same rate.

In the observation well B1, we pumped water at ~ 5.5 L/min and acquired single-hole GPR data (250 MHz omni-directional antennas with a dominant frequency of 140 MHz, 4 m antenna spacing) with a depth sampling of $\Delta z = 0.1$ m over $z = 35$ -75 m. We used 250 MHz antennas to obtain a high resolution even though Tsoflias and Becker (2008) have shown that lower frequency antennas are more sensitive to salinity changes. Thirty GPR raw sections $\mathbf{D}_1^{\text{raw}}$ to $\mathbf{D}_{30}^{\text{raw}}$ together with borehole fluid electrical conductivity and pressure logs (logger attached to the antenna cables just above the upper antenna) were acquired at observation times t^{obs} relative to the start of the injection. The reference section $\mathbf{D}_1^{\text{raw}}$ was acquired just before the injection, and the following sections $\mathbf{D}_i^{\text{raw}}$ were acquired every 10 minutes (the acquisition of one GPR section takes approximately 5 minutes), except $\mathbf{D}_{30}^{\text{raw}}$ that was acquired the next day after overnight pumping. Relative vertical positioning accuracy of a few cm between time-lapses was possible by using a calibrated digital measuring wheel, and by marking the start and end points on the cables. Two plastic centralizers attached to each antenna assured that the lateral positions within the boreholes were similar between surveys.

3.4 Data processing

Apart from standard GPR processing, we accounted for (1) depth-positioning uncertainties on the cm-scale, (2) temporal variations in the effective source signals caused by variations in the borehole fluid conductivity, and (3) significant direct wave energy and ringing signals caused by poor dielectric coupling that dominate the individual raw sections $\mathbf{D}_1^{\text{raw}}$ to $\mathbf{D}_{30}^{\text{raw}}$ at traveltimes $t < 90$ ns. Generally, the raw data have high signal-to-noise-ratios for $t < 160$ ns.

Static corrections accounted for time-zero drifts and residual misalignments of the direct wave between individual sections. An initial geometrical scaling was applied together with a wide bandpass filter in the frequency domain (linear tapered with corner frequencies 0-20-300-380 MHz). We accounted for depth positioning errors by maximizing the correlation between the zero-crossing patterns of individual data traces compared to the stacked section of all data (the standard deviation of the corrections was 3 cm).

To correct for temporal changes of the effective source signal, we applied a continuous wavelet transform and analyzed the wavelet power spectra of the data using the Morlet wavelet (Torrence and Compo, 1998). Firstly, we removed the wavelet scales with corresponding center frequencies outside of the 20-160 MHz range. Secondly, wavelet-scale dependent factors \mathbf{F}_i were defined as the ratios of wavelet power of the direct wave of the processed data $\mathbf{D}_i^{\text{proc}}$ with respect to the reference $\mathbf{D}_1^{\text{proc}}$ ($= \mathbf{R}_1^{\text{proc}}$). We then used the factors \mathbf{F}_i to rescale $\mathbf{R}_1^{\text{proc}}$ in the wavelet domain into new reference sections $\mathbf{R}_2^{\text{proc}}$ to $\mathbf{R}_{30}^{\text{proc}}$. The underlying assumption for this correction is that the increased electrical conductivity of the borehole fluid affects the direct wave in the same way as later arriving signals, such that any remaining differences between time-lapses only reflect changes occurring within the rock formation. We rescaled $\mathbf{R}_1^{\text{proc}}$ instead of $\mathbf{D}_i^{\text{proc}}$ because of the higher bandwidth of $\mathbf{R}_1^{\text{proc}}$ as attenuation of higher frequencies increases towards later acquisition times due to the increasing borehole fluid conductivity. An

eigenvector filter applied in a window around the direct wave ($t < 90$ ns) removed ringing effects parallel to the direct wave in the individual sections $\mathbf{R}_i^{\text{proc}}$ and $\mathbf{D}_i^{\text{proc}}$.

To facilitate amplitude comparisons for different traveltimes and time-lapses we calculated the relative differences \mathbf{M}_i by multiplying the differences $\mathbf{D}_i^{\text{proc}} - \mathbf{R}_i^{\text{proc}}$ with the inverse envelope sections of $\mathbf{R}_i^{\text{proc}}$. We defined a minimum amplitude threshold for the envelope sections of $\mathbf{R}_i^{\text{proc}}$ to avoid overestimating difference energy in low-reflectivity regions. The estimated relative difference magnitudes vary smoothly between time-lapses, the main changes occur during the first few time-lapses, and the signal returns towards the background at the end of the experiment (not shown).

Pre-stack Kirchhoff depth-migration based on the 1-D velocity function of Dorn *et al.* (2012a) made it possible to migrate \mathbf{M}_i with minimal smearing or other artifacts (Figure 3.1). Migration of difference sections is useful as the linearity of migration in the input wavefield term makes the final migrated sections comparable to GPR results obtained under natural flow and tracer-free conditions (Dorn *et al.*, 2012a). The unmigrated difference sections \mathbf{M}_i (not shown) contain significant random noise at $t > 130$ ns, but the destructive superposition of random noise energy during migration significantly decreases the presence of incoherent events in the migrated images.

3.5 Discussion

The migrated relative difference sections of \mathbf{M}_i (6 of them are shown in Figure 3.1) display patterns of high magnitudes with subhorizontal to vertical dips ($30\text{-}90^\circ$, relative to the surface) at $r = 2\text{-}10$ m radial distance from B1. Note that we only image changes in a 2-D projection around the borehole (i.e., depth z and radial distance r). In general, patterns close to the injection point are imaged only at early times t^{obs} . Further away from the injection point, patterns appear at later t^{obs} and they are visible for longer time periods. The evolving magnitudes can be traced from the injection point at $z = 55.6$ m in B2 throughout the depth interval $z = 40\text{-}72$ m. The dips and locations of these features correlate well with previously imaged fractures from static multi-offset single-hole data (Figure 3.2a) (Dorn *et al.*, 2012a) and hydrogeological studies (see Figure 3.2a) (Le Borgne *et al.*, 2007). This makes us confident that we can identify the main tracer-occupied fractures in Figure 3.2a by superimposing migrated difference sections on the static images from B1 and in B2 (Figure 3.2b) by identifying the same fractures as in B1 based on their dips and depths.

At $t^{\text{obs}} = 2$ min (Figure 3.1a), high magnitudes are concentrated in front of the injection interval (C1 in Figure 3.2) indicating that we can image the injected tracer. Other imaged features correlate with a fracture intersecting B1 at 50.9 m and a complex subvertical fracture zone pattern at $z = 40\text{-}47$ m (see Figure 3.2). We think that these changes possibly relate to reactivation of remaining tracer from previously performed saline tracer experiments, performed in the preceding days, as we change the pumping and injection configuration. At $t^{\text{obs}} = 12$ min (Figure 3.1b), we find that the pattern around the injection point has grown in

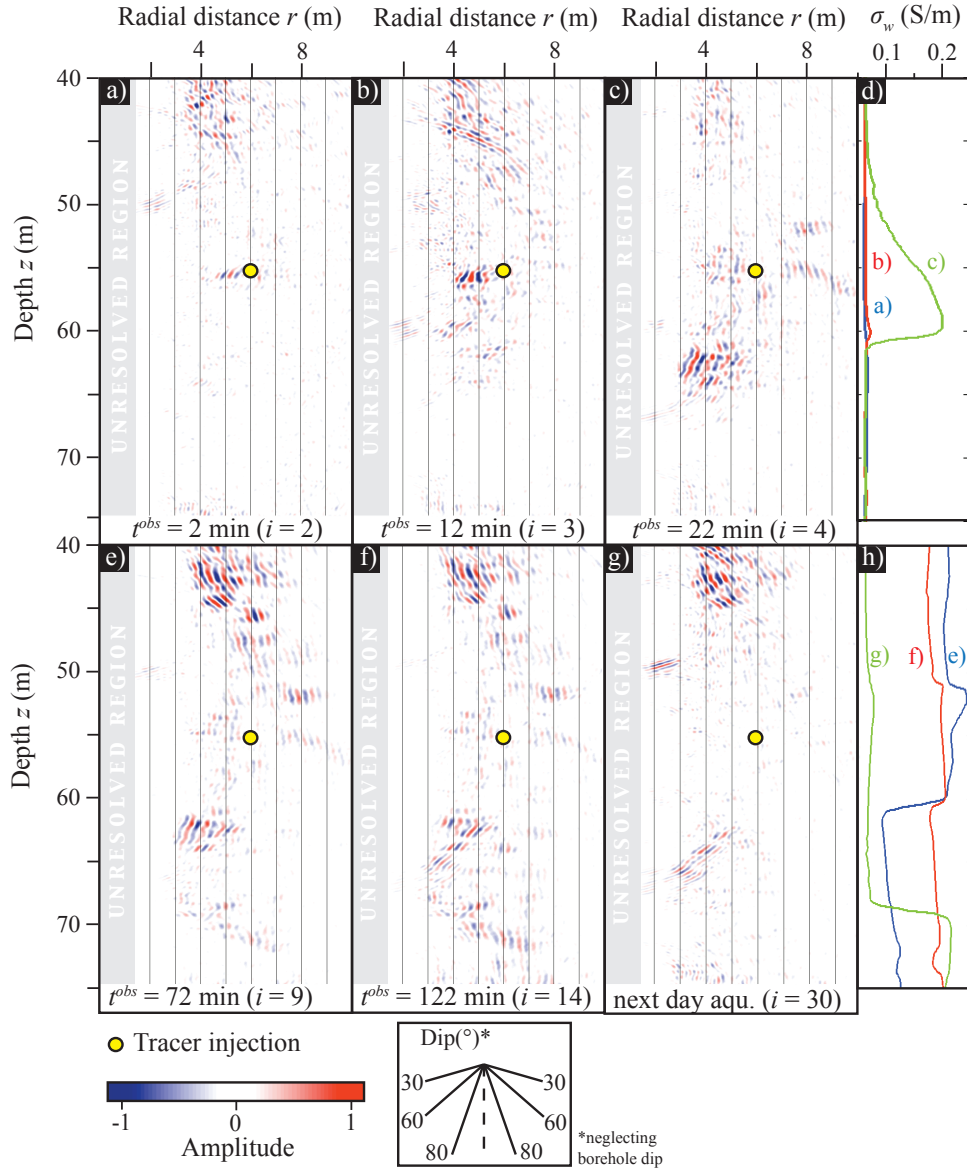


Figure 3.1: Migrated relative difference GPR sections acquired in B1 at t^{obs} (a) 2 min, (b) 12 min, (c) 22 min, (e) 72 min, (f) 122 min, and (g) next day acquisition. (d) and (h) Electrical conductivity σ_w of the borehole fluid in B1 acquired at the observation times t^{obs} in (a-c) and (e-g), respectively. High difference patterns originate from increased salinity in fractures located at the front of each such pattern (i.e., smallest radial distance r for each depth z). Note that we do not image any features at $r < 1.5$ m (gray region) because of the dominance of the direct wave at early times and its subsequent removal, which tends to remove superimposed reflections at early times.

size and magnitude. At the same t^{obs} , a feature appears at $z = 60$ m that is related to the fracture dipping 30° (C2 in Figure 3.2) through which the first saline tracer arrive in B1 at this time (Figure 3.1d). The downward movement of the tracer continues at $t^{obs} = 22$ min (Figure 3.1c) with a dip of 75° at $z = 62$ -65 m (C3 in Figure 3.2) and a reflectivity pattern appear dipping 50° at $z = 63$ -66 m (C4 in Figure 3.2). A pattern at $t^{obs} = 22$ min and $r > 7$ m

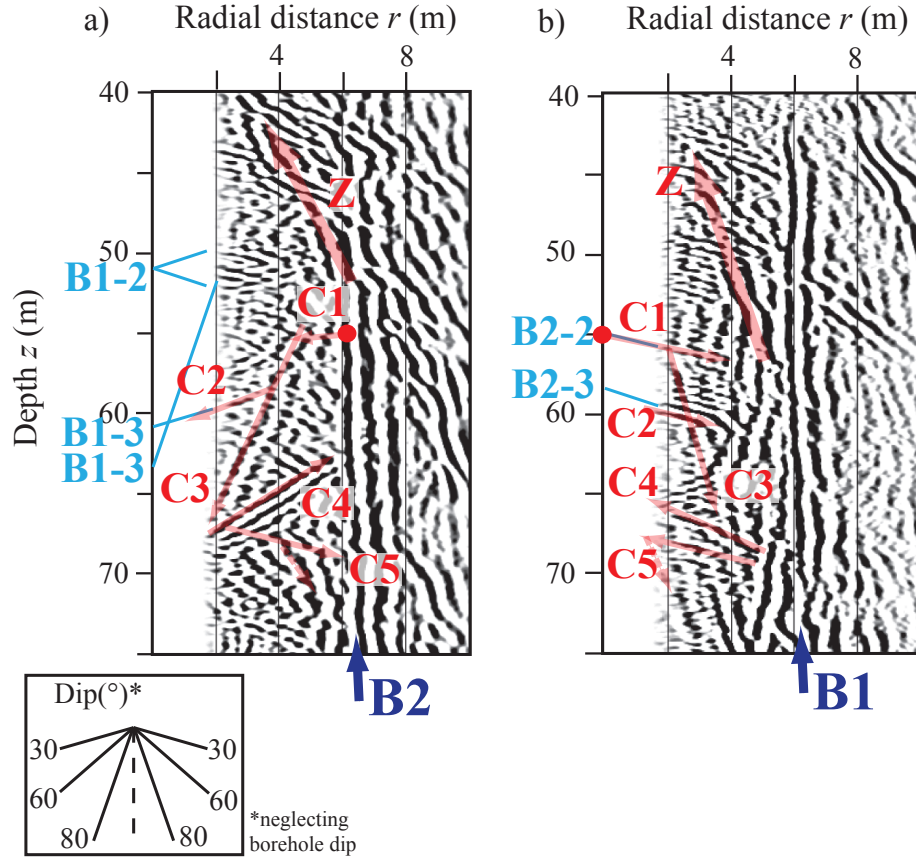


Figure 3.2: Extracts of migrated static single-hole GPR sections of (a) B1 and (b) B2 from Dorn *et al.* (2012a) with superimposed interpretation (orange arrows) of fractures (C1-C5, Z) through which the injected tracer moves and the possible flow direction. Light blue letters refer to transmissive fractures identified in the boreholes using optical logs and flowmeter tests (Le Borgne *et al.*, 2007), whereas marine blue letters refer to reflections from other boreholes.

appear that is likely related to the feature (Z in Figure 3.2) with prominent to moderate magnitudes developing at $z = 40 - 57$ m (Figure 3.1e-g). Between $t^{obs} = 72-122$ min a patchy moderate magnitude pattern develops at $z > 67$ m (C5 in Figure 3.2) indicating continuous downward movement of the tracer. The next day acquisition ($i = 30$, Figure 3.1g) shows a few locations of remaining high magnitudes (C4, Z, and the fracture intersecting borehole at $z = 50.9$ m that now reappear), but most of these patterns have disappeared indicating a return to background conditions.

It is possible to follow the tracer between time-lapses, which allows us to estimate approximate velocities of the tracer front (e.g., $v = 0.4-0.7$ m/min in fractures C2 and C3). The upward movement of the tracer in Z is likely related to the natural upward pressure gradient at the site (i.e., there is an ambient upward flow of ~ 1.5 L/min in B1) (Le Borgne *et al.*, 2007). The slower changes between time-lapses at later times $t^{obs} > 72$ min may indicate that the remaining tracer is largely unaffected by the pressure gradient imposed in the injection and

extraction borehole, and rather follow natural flow gradients (e.g., C4 and Z in Figure 3.2).

There is significant tracer arrival in the observation borehole B1 through C2 (see Figure 3.1d and h) in accordance with the imaged magnitude patterns at early times. There is also a deeper arrival of saline tracer arriving after more than one hour, which is likely to occur at 78.7 m (Le Borgne *et al.*, 2007) (see Figure 3.1h). This later and deeper tracer arrival gives confidence in the hydrological significance of C5 (Figure 3.1e-g). The reflectivity corresponding to the fracture at $z = 50.9$ m for early t^{obs} and the next day acquisition seems uncorrelated with the information from the electrical conductivity logs as this fracture appear to produce fresh groundwater (see Figure 3.1h). This highlights the need to complement this type of experiment with other data that track the arrival of the saline tracer in the borehole. Furthermore, we argue that televiewer data and flowmeter measurements (Le Borgne *et al.*, 2007) offer an excellent complement to characterize the near-borehole environment as fractures within $r < 1.5$ m cannot be imaged with the GPR data.

3.6 Conclusions

We find that single-hole GPR reflection imaging is capable of monitoring saline tracer movement through a connected network of mm-aperture fractures over tens of meters. This was made possible through careful positioning, a rather elaborate processing of the single-hole GPR data and by depth-migrating the relative-difference sections. The processing scheme accounted for variable borehole fluid conductivities, variable transmitter power and geometrical inaccuracies.

The final migrated relative-difference sections image spatially- and temporally evolving patterns at $r = 2$ -10 m radial distance with dips between 30-90° at locations corresponding to previously imaged fractures. We conclude that the saline tracer occupies at least 5 fractures (C1-C5) and a large fracture zone (Z) during the tracer experiment. As single-hole GPR reflection data with omni-directional antennas provide 2-D projections of reflections, we can only assign a minimum velocity of tracer movements (e.g., ~ 0.4 m/min for C4). One main advantage of these types of experiments compared to classical tracer experiments is that they provide a length scale of the tracer transport path that can be used together with the breakthrough data to determine transport velocities.

Data from this experiment and another five unreported tracer experiments will in the future be combined with flowmeter data and hydrogeological modeling to constrain the possible geometry and fracture properties of the hydrologically most prominent fractures at the site.

Chapter 4

Inferring Transport Characteristics in a Fractured Rock Aquifer by Combining Single-Hole GPR Reflection Monitoring and Tracer Test Data

Caroline Dorn, Niklas Linde, Tanguy Le Borgne, Olivier Bour, Maria Klepikova

published in *Water Resources Research*¹

¹C. Dorn, N. Linde, T. Le Borgne, O. Bour and M. Klepikova (2012). Inferring transport characteristics in a fractured rock aquifer by combining single-hole GPR reflection monitoring and tracer test data. *Water Resources Research*, **48**(11), W11521.

4.1 Abstract

Investigations of solute transport in fractured rock aquifers often rely on tracer test data acquired at a limited number of observation points. Such data do not, by themselves, allow detailed assessments of the spreading of the injected tracer plume. To better understand the transport behavior in a granitic aquifer, we combine tracer test data with single-hole ground-penetrating radar (GPR) reflection monitoring data. Five successful tracer tests were performed under various experimental conditions between two boreholes 6 m apart. For each experiment, saline tracer was injected into a previously identified packed-off transmissive fracture, while repeatedly acquiring single-hole GPR reflection profiles together with electrical conductivity logs in the pumping borehole. By analyzing depth-migrated GPR difference images together with tracer breakthrough curves and associated simplified flow- and transport modeling, we estimate (1) the number, the connectivity and the geometry of fractures that contribute to tracer transport, (2) the velocity and the mass of tracer that was carried along each flowpath, and (3) effective transport parameters of the identified flowpaths. We find a qualitative agreement when comparing the time evolution of GPR reflectivity strengths at strategic locations in the formation with those arising from simulated transport. The discrepancies are on the same order as those between observed and simulated breakthrough curves at the outflow locations. The rather subtle and repeatable GPR signals provide useful and complementary information to tracer test data acquired at the outflow locations and may help to characterize transport phenomena in fractured rock aquifers.

4.2 Introduction

Security concerns about waste disposals (nuclear, toxic waste, CO₂) and the need for efficient and sustainable extractions of natural resources (water, oil, gas, heat) in fractured rock formations require both process understanding and characterization of transport properties in fractured media. This implies a need for reliable monitoring technology for tracking temporal changes in the subsurface, in particular those related to contaminant transport. The limited accessibility to fractured rock systems contrasts with hydrological properties that are typically extremely heterogeneous at all scales (e.g., Bonnet *et al.*, 2001; Long *et al.*, 1996; Paillet, 1998). Generally, the data available for constraining fractured rock models have rather low information content with respect to the complexity of the system. For example, breakthrough curve data can be explained by a relatively small number of model parameters, while a very complex structure might have given rise to the observed data (e.g., Becker and Shapiro, 2000, 2003).

Models of conservative solute transport in fractured media typically combine advective and dispersive transport mechanisms within fractures with possibly matrix diffusion and sorption (Małoszewski and Zuber, 1985; Hadermann and Heer, 1996; Lapcevic *et al.*, 1999). While these basic mechanisms are well known, a major challenge for modeling a system is the adequate

description of heterogeneity at different scales. At the scale of the fracture, heterogeneous advection or flow channeling has been shown to be very common. Flow channeling, which is a phenomenon that increases in importance with the statistical variability in fracture aperture, refers to the situation in which the flow within discrete pathways make up a very large fraction of the total flow (Tsang and Neretnieks, 1998; Moreno and Tsang, 1994). Highly localized fluxes and diffusion into stagnant inter-channel spaces within fracture planes are typically not taken into account in classical dispersion theories and the testing of alternative transport models requires detailed experimental investigations and imaging at the fracture scale (Becker and Shapiro, 2000).

Stochastic continuum methods can provide equivalent distributed models explaining observed state variables (e.g., temperature, pressure, tracer concentration, etc.) (Neuman and Di Federico, 2003). The applicability of such models at the local field-scale (1-100 m) is questionable in fractured rock systems as it is uncertain if a representative elementary volume (REV) exists as fractures often prevail at all scales (Long *et al.*, 1982; De Dreuzy *et al.*, 2001, 2002; Neuman, 2005). Alternative representations based on Discrete Fracture Networks (DFN) (e.g., Darcel *et al.*, 2003) are relatively difficult to condition and calibrate even with detailed measurements of aperture in boreholes or in-situ flow properties (Neuman, 2005). Instead of building complex distributed models of heterogeneity, it is possible to account for unresolved heterogeneity and processes using effective models, for example, using concepts of multi-rate mass transfer (Haggerty and Gorelick, 1995; Cvetkovic and Haggerty, 2002), continuous time-random walk (Berkowitz *et al.*, 2006), or multiple flow channels (Becker and Shapiro, 2000). However, it is often difficult to assess which interpretive framework is the relevant considering typically available breakthrough data (or other hydrological data) (Haggerty *et al.*, 2000, 2001; Harvey and Gorelick, 2000; Le Borgne and Gouze, 2008). Obtaining spatially distributed images related to tracer movement within the formation can therefore be of key importance for defining appropriate effective models for transport in fractured media.

When analyzing breakthrough curves alone, it is generally not possible to uniquely (1) determine if transport occurs through one or several fractures and if multiple arrivals are caused by fracture heterogeneity (aperture variations) or by multiple flow paths involving different fractures or (2) infer what may be the cause of low mass recovery (e.g., through flowpaths driven by density effects or ambient flow; storage close to the injection point, in the fractures taking part in the tracer transport or through mass exchange with the rock matrix).

Geophysical imaging may provide information about subsurface structure and dynamics in-between the injection and extraction points, that is, at locations where hydrological data are generally not available (e.g., Rubin and Hubbard, 2006). One of the most suitable geophysical methods in fractured rock investigations at the 1-100 m scale is GPR. This method allows detecting mm-aperture fractures and resolving temporal changes away from the observation points (Olsson *et al.*, 1992; Lane Jr *et al.*, 1996, 1998; Grègoire and Joesten, 2006; Becker and Tsofilas, 2010; Dorn *et al.*, 2011). Surface GPR is useful to study transport in shallow subhorizontal fractures (Talley *et al.*, 2005; Becker and Tsofilas, 2010). For larger depths,

cross-hole difference-attenuation radar tomography (e.g., Liu *et al.*, 1998; Day-Lewis *et al.*, 2003) can image tracer movement through fracture zones, but the resolution of the resulting tomograms is insufficient for imaging transport in individual mm-aperture fractures.

Dorn *et al.* (2011) showed that time-lapse single-hole GPR data acquired during and after saline tracer injection tests allow imaging tracer movement through a network of connected fractures. The recovered images are relatively subtle despite extensive processing and many different time-lapses are necessary to make robust interpretations concerning transport pathways. Nevertheless, the resulting information about tracer transport and storage cannot be obtained by any other field technique that we are aware of, which warrants further study with this type of data. Herein, we build on the work by Dorn *et al.* (2011) by analyzing five tracer experiments (one of them being the experiment presented in our previous study) that were acquired under different injection and pumping conditions in a granitic rock aquifer. The objectives of this work are to show that time-lapse single-hole GPR reflection data acquired during saline tracer injection experiments make it possible to (1) obtain repeatable results, (2) identify transport pathways over tens of meters through connected individual fractures, (3) identify main transport mechanisms and causes of incomplete mass recovery at a site, and (4) provide geometrical constraints for the estimation of effective transport properties, namely hydraulic conductivities and dispersion coefficients. It is our hope that this contribution will motivate further research in how time-lapse GPR data can be used in fractured rock hydrology for (1) model validation, (2) model calibration, and (3) inversion purposes. A simplified flow- and transport model calibrated to the breakthrough data is used to highlight some of these possibilities and associated challenges.

4.3 Methods

4.3.1 The single-hole ground-penetrating radar reflection method

Ground-penetrating radar (GPR) is an electromagnetic imaging method of the subsurface that is presented by Annan (2005), while Balanis (1989) describes the underlying physics of radar wave propagation. A GPR transmitter sends a source signal out into the medium, while a GPR receiver collects the resulting signals arising from signal transmission, reflections, and scattering at electromagnetic boundaries. The single-hole GPR configuration refers to the case in which the transmitter and receiver are both located in the same borehole at a known separation (see Figure 4.1). In single-hole reflection mode, imaged reflectors can arise from fractures located in all directions from the borehole as illustrated in Figure 4.1; planar reflectors that intersect the borehole are imaged as V-shaped reflections. Data processing of the acquired data allows determining the distances to the reflectors and their associated dips, but not their azimuth. Reflectors are predominantly related to variations in electrical permittivity ϵ , but also in electrical conductivity σ , and in magnetic permeability μ . The attenuation of the signal propagating in the medium is proportional to σ . The data recorded by a receiver located at a given distance from the transmitter is traditionally used to image boundaries that in fractured

media correspond to fracture surfaces (e.g., Olsson *et al.*, 1992; Liu and Sato, 2006). When saline tracer arrives at a fracture, the locally elevated conductivity leads to increases in the reflectivity of the fracture and thus a higher amplitude GPR reflection (Tsoflias and Becker, 2008). An unwanted effect associated with measurements in boreholes following tracer injection tests is that temporal variations in fluid conductivity within the pumping borehole changes the radiation characteristics of the antenna (Ernst *et al.*, 2006) and therefore the effective source wavelet, which complicates the subsequent data processing.

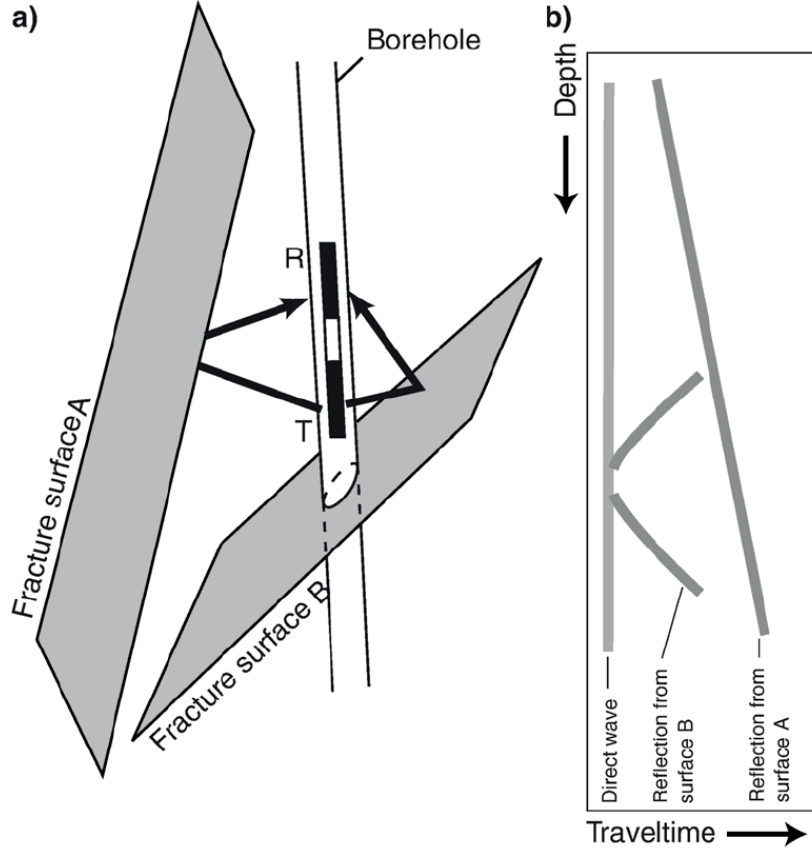


Figure 4.1: (a) Principle of the single-hole GPR reflection method, in which a transmitter T sends out a signal that is reflected and subsequently collected by a receiver R located in the same borehole as the transmitter. (b) Schematic reflection section illustrating typical reflection patterns arising from intersecting and non-intersecting fractures. Figure from Spillmann *et al.* (2007).

Beside the medium constitutive parameters, the recorded reflection amplitude from a fracture depends on a number of factors: (1) The fracture aperture and signal wavelength, as closely spaced reflections from the upper and lower fracture surfaces interfere with each other (Tsoflias and Becker, 2008; Widess, 1973). (2) The dip of the fracture, as the reflection coefficient of a dipping interface (or fracture) is a function of the signal angle of incidence and signal polarization (Bradford and Deeds, 2006; Tsoflias and Hoch, 2006), subvertical dipping features have higher reflection amplitudes than subhorizontal fractures when using GPR in

vertical boreholes (0-30° dipping fractures are not directly detectable). (3) The distance between a fracture and the antennas, due to signal attenuation fractures are detectable up to roughly $r \approx 15$ m radial distance in granitic formations using a central signal frequency of 140 MHz. (4) The spatial extent of a fracture, as a reflection is an integration over an area of about the first Fresnel-zone (e.g., for a central frequency of 140 MHz, the Fresnel-radius is 0.6 m at a radial distance $r = 2$ m and 2 m at $r = 20$ m). (5) The azimuth of a fracture, as reflections from a plane fracture can only be observed if a normal-vector to the reflector crosses the borehole. (6) The roughness of the fracture that creates diffractions that might allow imaging of fractures with unfavorable orientations.

4.3.2 Field site

The experiments presented herein were carried out within a fractured rock aquifer that constitutes the main water supply for the town of Ploemeur, France (Figure 4.2), with an average extraction rate of 2,000 L/min (Le Borgne *et al.*, 2006). Our tracer tests were conducted ~ 3 km away from the water extraction site at the test-site Stang-er-Brune (Le Borgne *et al.*, 2007). The experiments were carried out between two ~ 6 m spaced boreholes B1 (83 m deep) and B2 (100 m deep). The boreholes reach a contact zone at a depth $z \approx 40$ m ($z = 0$ m corresponds to the top of the B1 borehole casing) between highly deformed mica schist and underlying saturated granite. Within the granite (at $z = 40$ -80 m), the strongly deviated B2 is located 40-100°N relative to B1. The granite formation has the most permeable fractures (Le Borgne *et al.*, 2007) and is therefore the area of primary interest in this study (Figure 4.2).

Le Borgne *et al.* (2007) used televiwer data together with hydraulic testing (notably single-hole and cross-hole flowmeter tests) at the site to characterize fractures that intersect the boreholes and identify those that are hydraulically connected. The formation is highly transmissive with overall hydraulic transmissivities on the order of 10^{-3} m²/s over the length of each borehole. Le Borgne *et al.* (2007) reported an ambient vertical upward flow in the boreholes of about 1.5 L/min. This ambient vertical flow is the result of a 50 cm hydraulic head difference between the deepest fractures at $z = 100$ m and the upper mica schist. This regional upward flow that appears in all permeable boreholes is also expected to affect the well-connected fractures. The transmissive fracture network at the site is dominated by a relatively limited number of well-connected fractures (i.e., only 3-5 such fractures intersect a borehole over its entire length). These fractures have a dip in the range of 30-80° and an azimuth in the range of 190-270°. The dips and azimuths of the boreholes suggest that there is no single fracture that intersects both boreholes B1 and B2 (Le Borgne *et al.*, 2007).

Dorn *et al.* (2012a) acquired 100 MHz and 250 MHz multifold single- and cross-hole GPR reflection data to constrain the geometry of the main fractures within the granite formation. Using the single-hole 250 MHz data, it was possible to obtain high-resolution images of the main fractures in the granite at radial distances $r = 2 - 13$ m away from B1 and B2 (Dorn *et al.*, 2012a) including those that were identified as being transmissive by Le Borgne *et al.* (2007).

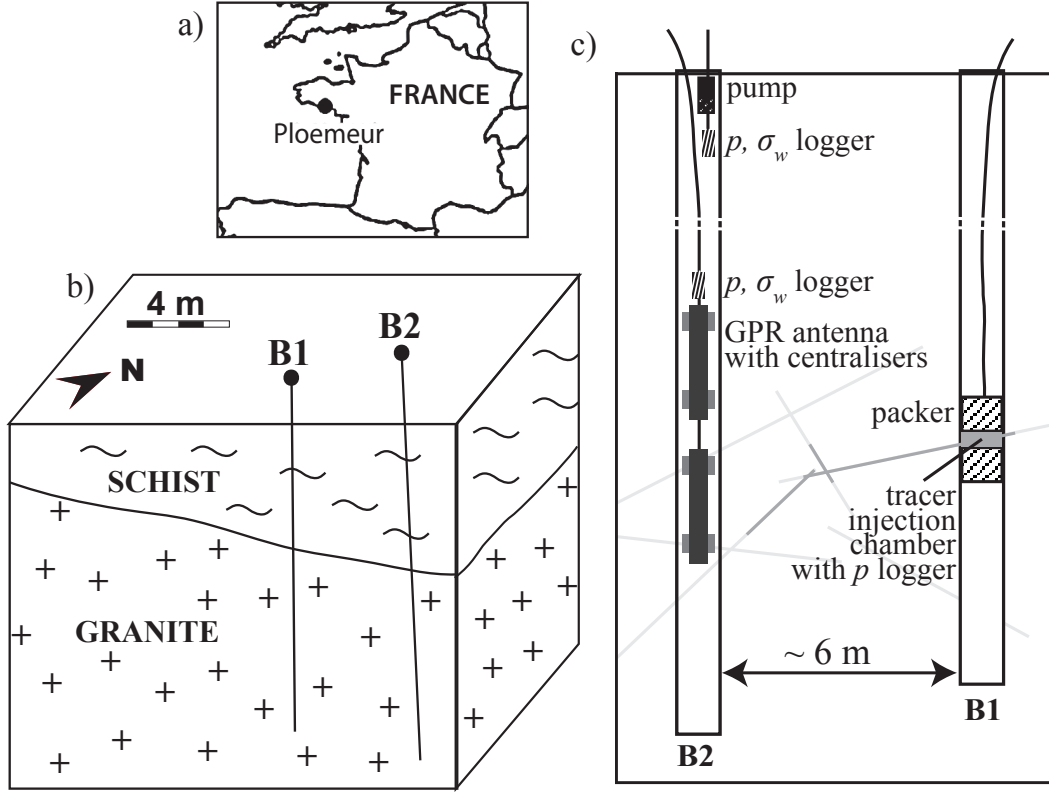


Figure 4.2: (a) Location of the Stang-er-Brune study-site in the vicinity of Ploemeur, France. (b) Geological model of the field site with a 30° dipping contact between mica schist and underlying granite. (c) Schematic of the data acquisition setup, in which p and σ_w logger refer to hydraulic pressure and groundwater conductivity loggers, respectively.

4.3.3 Experimental setup

Table 4.1 provides the experimental details of the tracer tests (referred to as experiments Ia, Ib, II, IIIa, and IIIb in the following) that were performed between B1 and B2 in June 2010. Figure 4.2c is a sketch of the experimental setup for the case in which B1 is the injection and B2 the pumping borehole. All logging takes place in the pumping borehole. Note that our naming convention is different than the one used by Le Borgne *et al.* (2007) in that we name each fracture according to the borehole name and the depth at which it intersects. For example, a fracture intersecting borehole B1 between $44.0 \text{ m} \leq z < 45.0 \text{ m}$ is named B1-44.

For each experiment, a saline solution of $\sim 90 \text{ L}$ was injected during a short time interval (10-30 min) at a controlled rate into a transmissive fracture (experiments Ia and Ib in B1-78, experiment II in B1-50, and experiments IIIa and IIIb in B2-55) that was isolated from the rest of the injection borehole by a double-packer system. The initial tracer salinity was ~ 100 times higher than the background salinity of the groundwater. After the injection, we continued in four of the five experiments to push the tracer with fresh groundwater at approximately the same rate. For experiment Ib, no further injection of fresh groundwater was pursued after

Table 4.1: Experimental setup of the five tracer experiments. The listed pumping rates refer to the time periods of GPR monitoring.

Experimental parameters	Experiments				
	Ia	Ib	II	IIIa	IIIb
	<i>Injection well</i>				
Fracture of injection	B1-78	B1-78	B1-50	B2-55	B2-55
Depth of injection	78.7 m	78.7 m	50.9 m	55.6 m	55.6 m
Injection rate	2-3 L/min	2.3-3.5 L/min	2.3-2.7 L/min	8-10 L/min	7-9 L/min
Amount of tracer	87 L	90 L	92 L	93.5 L	92.5 L
Injected amount of salt	3.5 kg	4.7 kg	3.7 kg	4.7 kg	4.6 kg
Tracer conductivity	5 S/m	5.5 S/m	5 S/m	5.5 S/m	5.5 S/m
Pushing tracer with fresh water	yes	no	yes	yes	yes
	<i>Observation well</i>				
Borehole	B2	B2	B2	B1	B1
Number of time steps N	16	21	29	31	33
Observation interval	35-95 m	35-90 m	35-85 m	35-80 m	35-75 m
Range of pumping rates	~30 L/min	5-30 L/min	13-25 L/min	1-10 L/min	5-6 L/min
Mean pumping rate	30 L/min	16 L/min	16 L/min	6 L/min	5.5 L/min
Mean time step	10 min	10 min	10 min	10 min	5 min
	<i>Mass Recovery</i>				
Recovered amount of salt	24%	15%	32%	19%	32%

the end of the tracer injection. To pull the tracer solution towards the pumping borehole, we pumped water in the upper cased section of the pumping borehole. Salt concentrations were monitored below the pump at $z = 10$ m using an electrical conductivity logger. Although the mean transfer time between the two boreholes was about 1 to 3 hours depending on the experiments, pumping lasted for at least 12 hours to remove most of the tracer from the rock formation. Along the observation depth interval in the pumping borehole, we repeatedly acquired single-hole GPR data while measuring the borehole fluid electrical conductivity σ_w and hydraulic pressure p (one CTD logger was attached to the GPR antenna cable just above the upper antenna, Figure 4.2c). We used 250 MHz GPR antennas (MALÅ Borehole antennas with center frequencies around 140 MHz; antenna separation of 4 m) to obtain a high spatial resolution.

The different raw GPR sections $\mathbf{D}_i^{\text{raw}}$ (depth sampling of $\Delta z = 0.1$ m) and corresponding σ_w borehole logs (depth sampling of $\Delta z < 0.2$ m) were acquired over observation intervals of tens of meters. Each time-lapse i is associated with an observation time t_i^{obs} relative to the start of the saline tracer injection. For each experiment, a reference GPR section $\mathbf{D}_1^{\text{raw}}$ was acquired just before the injection, and the following sections $\mathbf{D}_i^{\text{raw}}$ were acquired every 5-10 minutes (the acquisition of one GPR section takes approximately 5 minutes), except for the last section $\mathbf{D}_N^{\text{raw}}$ that was acquired the following day after overnight pumping. Repeatability

in the vertical positioning between the radar sections of a few cm were obtained by using a calibrated digital measuring wheel and by marking the start and end points on the cables. Two plastic centralizers attached to each GPR antenna assured that the lateral positions within the boreholes were similar between acquisitions (Figure 4.2c).

The whole suite of experiments (Table 4.1) allowed us to investigate under different conditions to what extent saline tracer transport in fractured media can be imaged with single-hole GPR reflection monitoring. The chosen injection points largely determine the fractures that take part in the tracer transport, but also variations in the injection and pumping rates will have a strong influence on the spreading of the tracer (especially at this site exhibiting significant ambient upward flow (~ 1.5 L/min) in the boreholes (Le Borgne *et al.*, 2007)). The main differences between experiments Ia and Ib were (as mentioned above) that no pushing of the injected tracer with groundwater was performed in experiment Ib and that the pumping rate was higher (~ 30 L/min) in experiment Ia than in experiment Ib (~ 16 L/min). The injection in experiment II was carried out in a fracture for which prior hydrological investigations indicate that the flowpaths toward B2 are rather subhorizontal. This is a challenging setup for single-hole GPR as subhorizontal fractures cannot directly be detected due to the high angle of incidence (tangential to the fracture) resulting in no reflected signal returning to the receiver antenna. Experiments IIIa and IIIb differ with respect to the previous surveys in terms of the higher injection rate (8-10 and 7-9 L/min); the pumping throughout experiment IIIa was unstable, whereas the pumping rate during experiment IIIb ranged between 5 and 6 L/min (see Table 4.1). Dorn *et al.* (2012a) presented the GPR results from experiment IIIa and processing of experiment IIIb reveals similar results. The processing employed was slightly different than what is proposed below, but the overall tendencies were very similar. The results from the GPR processing presented herein therefore only consider experiments Ia, Ib, and II, while the results of experiments IIIa and IIIb are included in the interpretation.

4.3.4 GPR data processing

The most important aspect of successful GPR difference imaging is repeatability. Processing of high-frequency single-hole GPR reflection monitoring data is very challenging and a quite extensive testing of alternative processing strategies was necessary to assure that the difference amplitudes are comparable between acquisitions and to assure smooth transitions in the retrieved patterns between time-lapses. Indeed, positioning accuracy of sources and receivers is most important when imaging subhorizontally dipping fractures. Apart from standard GPR processing, we therefore had to account for (1) vertical positioning uncertainties on the cm-scale due to cable twisting during the data acquisition, (2) temporal variations in the effective GPR source signals caused by variations in the borehole fluid conductivity, and (3) significant direct wave energy and ringing signals caused by poor dielectric coupling that severely contaminate the individual raw sections $\mathbf{D}_1^{\text{raw}}$ to $\mathbf{D}_N^{\text{raw}}$ for traveltimes $t < 90$ ns (the direct wave is a wave traveling along the borehole wall). Generally, the raw data have high signal-to-noise-ratios for $t < 160$ ns.

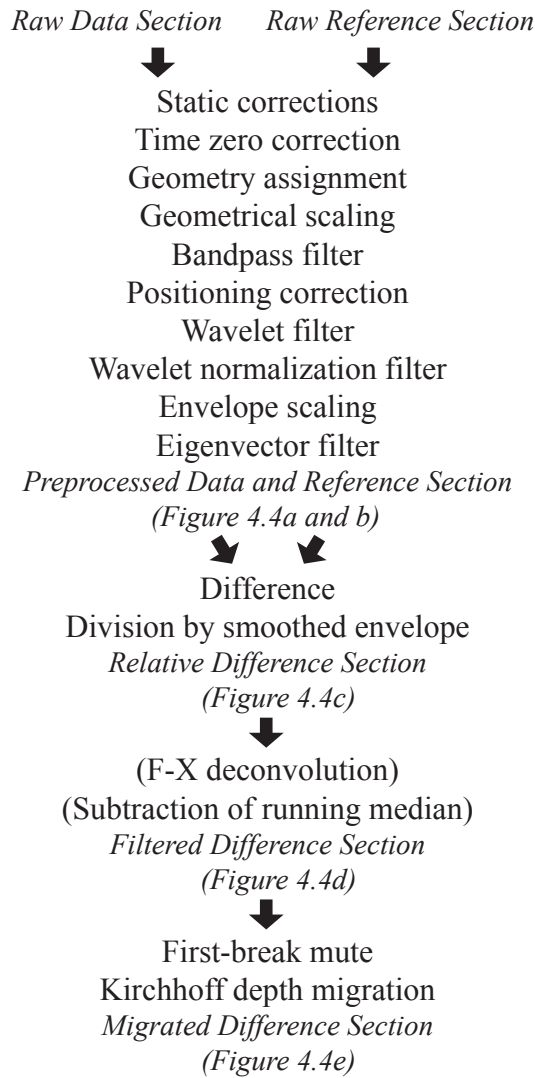


Figure 4.3: Flowchart of the GPR processing steps with reference to figures showing intermediate results. Processing steps in parenthesis only apply to experiments Ia and Ib.

Figure 4.3 summarizes the main processing steps of the GPR data. We accounted for time-zero drifts of the transmitter initialization time before correcting the residual misalignments of the direct wave between individual sections. An initial geometrical scaling of the signal was applied assuming spherical divergence of the source amplitude followed by a wide band pass filter in the frequency domain (linearly tapered with corner frequencies 0-20-300-380 MHz) that removes low and high frequency noise.

To minimize vertical positioning errors, we calculated depth corrections (Figure 4.3) using the processed data up to this point. To calculate the corrections, we aligned first-arrival energy, restricted the data to a time window after the first arrivals for times with a high signal-to-noise-ratio, applied a dip filter to suppress signals parallel to the direct wave, and narrowed the frequency spectrum of the data (60-70-190-210 MHz). We then calculated zero-crossing

patterns of all data traces (1 for a zero-crossing before a maximum, -1 before a minimum and 0 otherwise). The vertical corrections were determined iteratively by searching, for each data trace, a correction that maximized the correlation between the zero-crossing patterns of an individual data trace and the corresponding stacked traces of all time-lapse data. The corrections were then used to construct a new stacked data section on which this process was repeated until the proposed correction from one iteration to the next was smaller than 3 cm on average. These corrections were applied to the widely bandpass filtered data (Figure 4.3).

To correct for temporal changes of the effective source signal due to salinity variations in the observation borehole, we followed Dorn *et al.* (2011) by applying a continuous wavelet transform and analyzing the wavelet power spectra of the data using the Morlet wavelet (Torrence and Compo, 1998). In a first step, we removed wavelet scales with center frequencies outside the 20-160 MHz range. In a second step, we defined wavelet-scale dependent factors \mathbf{F}_i as the ratios of the wavelet power of the direct wave of the processed data $\mathbf{D}_i^{\text{proc}}$ with respect to the direct wave of the reference $\mathbf{D}_1^{\text{proc}}$ ($= \mathbf{R}_1^{\text{proc}}$). We then used the factors \mathbf{F}_i to rescale $\mathbf{R}_1^{\text{proc}}$ in the wavelet domain into new reference sections $\mathbf{R}_i^{\text{proc}}$. The underlying assumption for this correction of the reference conditions is that the increased electrical conductivity of the borehole fluid affects the later arriving signals similarly as the direct wave, such that any remaining differences between time-lapses after this correction only reflect changes occurring within the rock formation. The reason for rescaling $\mathbf{R}_1^{\text{proc}}$ instead of $\mathbf{D}_i^{\text{proc}}$ is the higher bandwidth of $\mathbf{R}_1^{\text{proc}}$ as high frequencies are strongly attenuated at later acquisition times due to the increasing borehole fluid conductivity.

To remove ringing signals caused by poor dielectric coupling, we applied an eigenvector filter that decomposes the data into eigenimages in a time window around the direct wave ($t < 90$ ns) using Karunen-Loeve theory. Then we excluded eigenimages representing ringing signals identified as those being parallel to the direct wave before reconstructing the data. After this preprocessing of the GPR data, the amplitudes are comparable and minimally affected by noise and signals other than reflections. As an example, the data at $t^{\text{obs}} = 45$ min and its reference section of experiment Ib are shown in Figure 4.4a and b. It is important to note that the reflections corresponding to fractures (or changes in salinity within the fractures during the time-lapse experiments) are seen over a relatively wide time-window (e.g., the strong top reflector between $z = 40$ -50 m) and do not represent direct images of the fractures. In fact, the recorded GPR signal is a convolution of a finite source signal (~ 30 ns corresponding to ~ 3 m) with a rather discrete reflectivity distribution arising from the mm-aperture fractures. The time or distance to a given reflector corresponds to the first-arriving energy in these wave trains.

To facilitate the comparison of difference magnitudes, we calculated relative differences \mathbf{M}_i (Figure 4.4c) over time by multiplying the differences $\mathbf{D}_i^{\text{proc}} - \mathbf{R}_i^{\text{proc}}$ with the inverse envelope (reflection strength) sections of $\mathbf{R}_i^{\text{proc}}$. To avoid over-interpreting energy differences in low-reflectivity regions, we defined a minimum amplitude threshold for the envelope sections of $\mathbf{R}_i^{\text{proc}}$. Generally, the relative difference magnitudes vary smoothly between time-lapses.

The largest changes occur during the first few time-lapses following the tracer injection and the signal generally returns towards zero at the end of the experiment (not shown). For experiments Ia and Ib it was necessary to further reduce the ambient noise level prior to migration (mapping data from time to distance from borehole) by applying a conservative f-x deconvolution (prediction filter in distance for each frequency) and subtracting a running median trace (Figure 4.4d, processing steps in brackets in Figure 4.3).

Pre-stack Kirchhoff depth-migration based on the 1-D velocity function of Dorn *et al.* (2012a) made it possible to migrate \mathbf{M}_i with minimal smearing or other artifacts (Figure 4.4e). Migration of difference sections is possible due to the linearity of migration with respect to the input wavefield term, which makes the final migrated sections comparable to migrated GPR sections (Dorn *et al.*, 2011). The unmigrated difference sections \mathbf{M}_i (Figure 4.4c) contain significant ambient noise at $t > 130$ ns, but the destructive superposition of ambient noise energy during migration significantly decreases the presence of incoherent events in the migrated images.

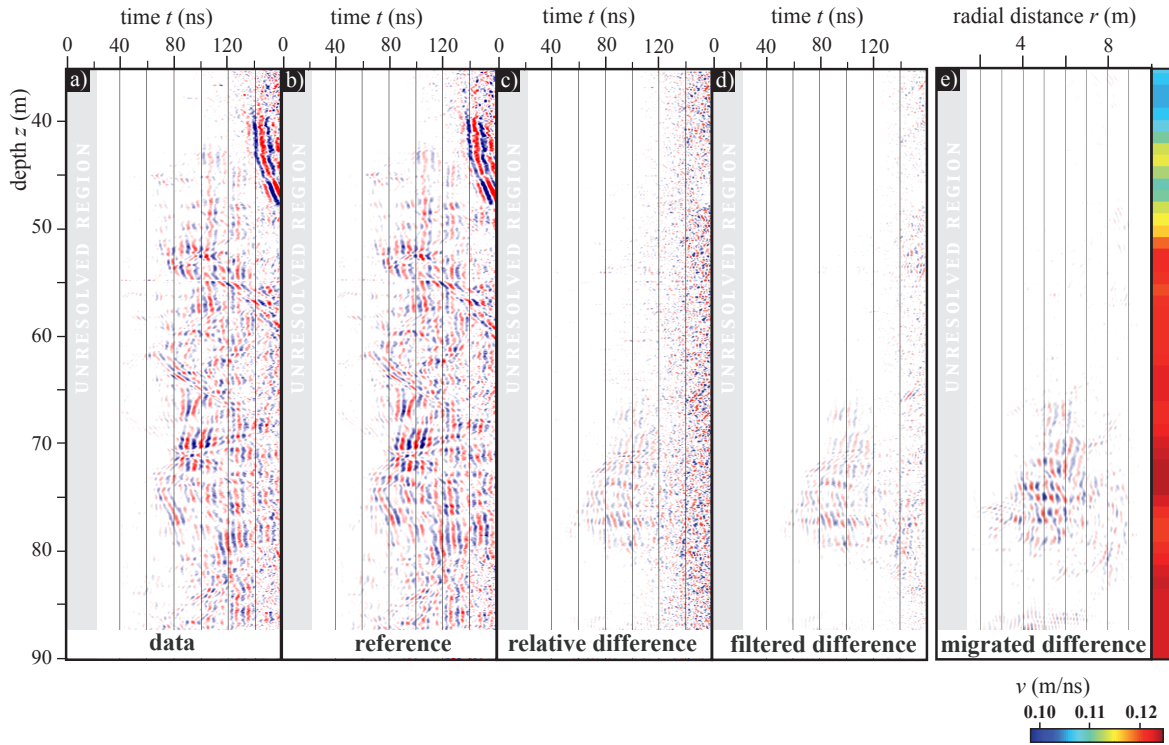


Figure 4.4: Results of data processing applied to a single-hole GPR data section of experiment Ib acquired after saline tracer injection at $z = 78.7$ m ($t^{obs} = 45$ min, 4 m antenna offset). (a) Data and (b) reference section after preprocessing. (c) Relative difference between (a) and (b) normalized by the envelopes of (b). (d) As in (c), but after f-x deconvolution to remove noise. (e) As in (d) but after depth migration using the velocity model shown to the right of the migrated difference. The axis aspect ratio $r:z$ is 2:1.

4.4 Results

4.4.1 Tracer test data

Figure 4.5 shows the measured electrical conductivities in the pumping borehole during the course of each experiment (interpolated from data logs with a depth sampling of $\Delta z < 0.2$ m and a time sampling $\Delta t \approx 10$ min, $\Delta t \approx 5$ min for experiment IIIb). The columns shown to the right of the each subfigure are the electrical conductivities acquired following overnight pumping. The flow and associated transport in the boreholes are directed upwards partly due to the natural upward gradient, but mainly because we pump at the top (except for experiment IIIa when the overnight pumping became weak and eventually stopped resulting in tracer accumulation at the bottom of the borehole).

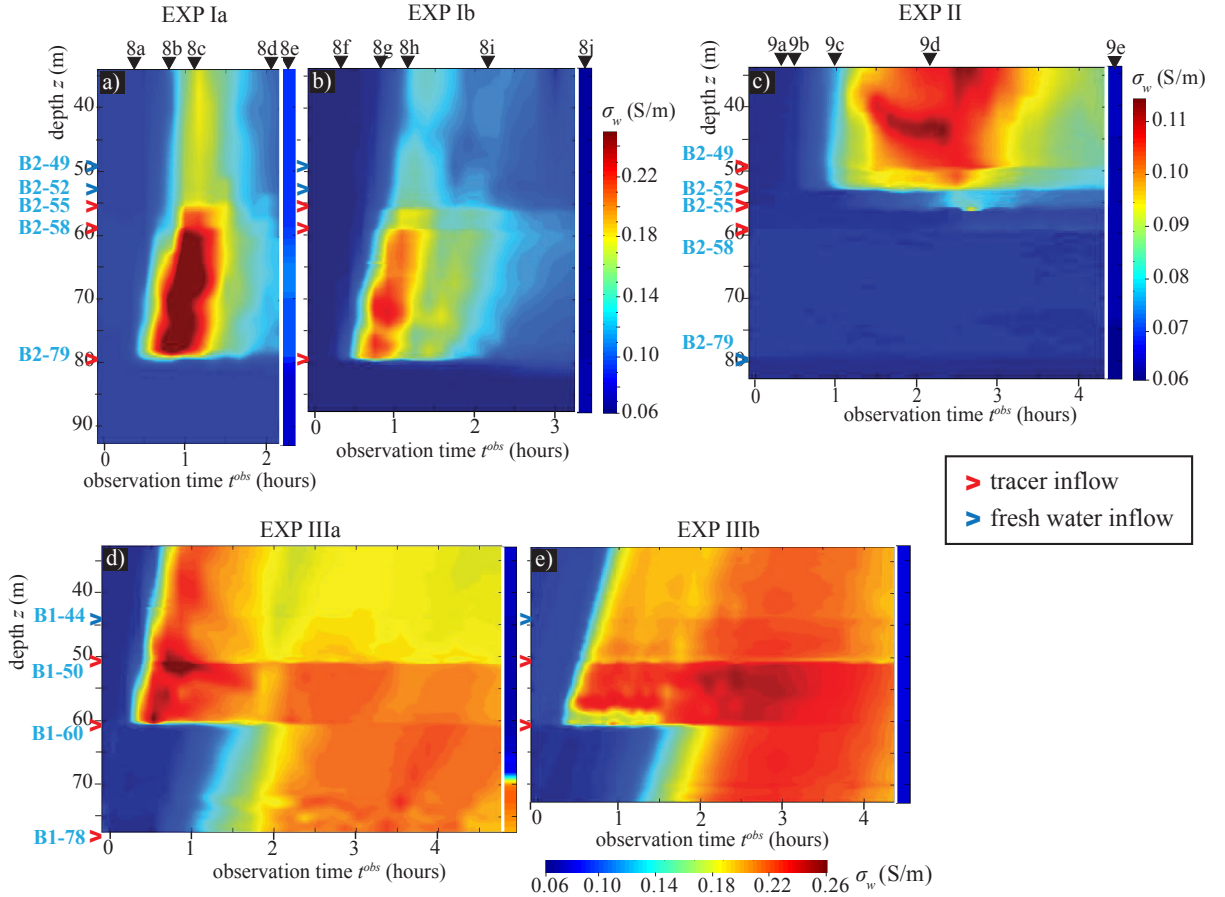


Figure 4.5: Electrical conductivity σ_w in the pumping borehole during experiments (a) Ia and (b) Ib, (c) II, and (d) IIIa and (e) IIIb. The values of σ_w the day after saline injections are shown in separate columns to the right of the subfigures. Black triangles mark the acquisition times of the conductivity profiles shown in Figures 4.8 and 4.9. The red arrowheads indicate locations with interpreted tracer inflow, while the blue arrowheads indicate inflow locations that are unaffected by the saline injections.

The variations of electrical conductivity in time and space can be used to identify tracer and freshwater outflow zones by identifying those locations in which the electrical conductivity varies sharply in the vertical direction over extended time periods. These zones highlighted in Figure 4.5 correspond to open fracture locations in the optical logs; most of them identified by Le Borgne *et al.* (2007): (1) B1-44, B1-50, B1-60 and B1-78; and (2) B2-49, B2-52, B2-55, B2-58 and B2-79. In experiments IIIa and IIIb, the location of the tracer outflow zone at the lower boundary of the observed depth interval (B1-78; see Figure 4.5d and e) is inferred from flowmeter data, as this is the only permeable zone below the observation interval. In order to identify the actual fractures through which tracer outflow occurs, we normalized the electrical conductivities (Figure 4.5) by the vertical flow distribution (Figure 4.6) of the fractures. In fact, some outflow zones do not carry significant amounts of tracer (see fractures B2-49 and B2-52 in Figure 4.5a-b, B2-58 and B2-79 in Figure 4.5c, and B1-44 and B1-52 in Figure 4.5d-e) and the tracer outflow zones B2-49 and B2-52 (experiment II) were not detected in the flowmeter data analysis of Le Borgne *et al.* (2007).

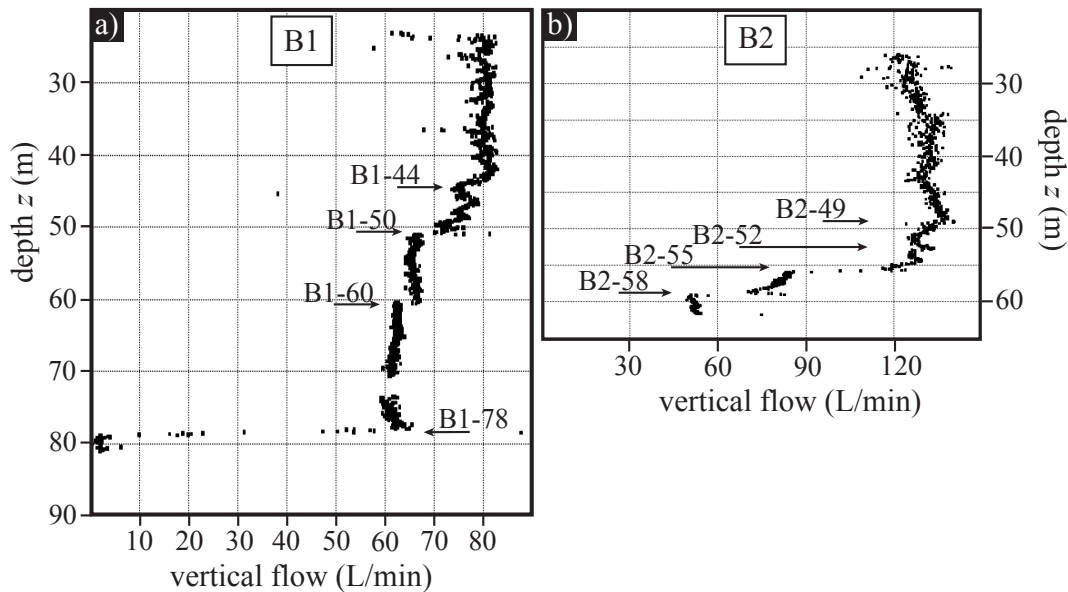


Figure 4.6: Induced vertical flow due to pumping in (a) B1 with 82 L/min and in (b) B2 with 138 L/min measured with an impeller flowmeter. All the flow below $z = 60$ m in B2 stems from fracture B2-79 at $z = 79.3$ m. Arrows indicate the locations of interpreted permeable fractures.

The peak electrical conductivities in the pumping borehole reach $\sim 5\%$ of the injected tracer conductivity, except for experiment II where we observe only $\sim 2.5\%$. Such low percentages are due to (1) dispersion of the solute within the fractured media, (2) the pumping of fresh water that mixes with the saline water within the pumping borehole and (3) the influence of the ambient flow regime that may lead to tracer mass loss.

To estimate the curves of mass recovered at each individual fracture, we subtracted the estimated mass flux in the borehole below the fracture from the estimated mass flux above. When

converting concentrations to mass rates, we accounted for the monitored, but rather unstable pumping rates (see Table 4.1), and available flowmeter data (Figure 4.6) that provide the relative contribution to flow of each outflow zone. To obtain the local mass recovery estimates, we then integrated the fracture-specific solute fluxes during the course of the GPR monitoring. The local mass recoveries should be analyzed with some caution as (1) the pumping rates and flow partitions between fractures are not perfectly known and (2) electrical conductivity logs acquired within the first 3-5 hours following the tracer injections do not capture the whole tail of the tracer breakthrough.

The derived fracture-specific curves of solute fluxes show very different characteristics for each type of tracer experiment (Figure 4.7).

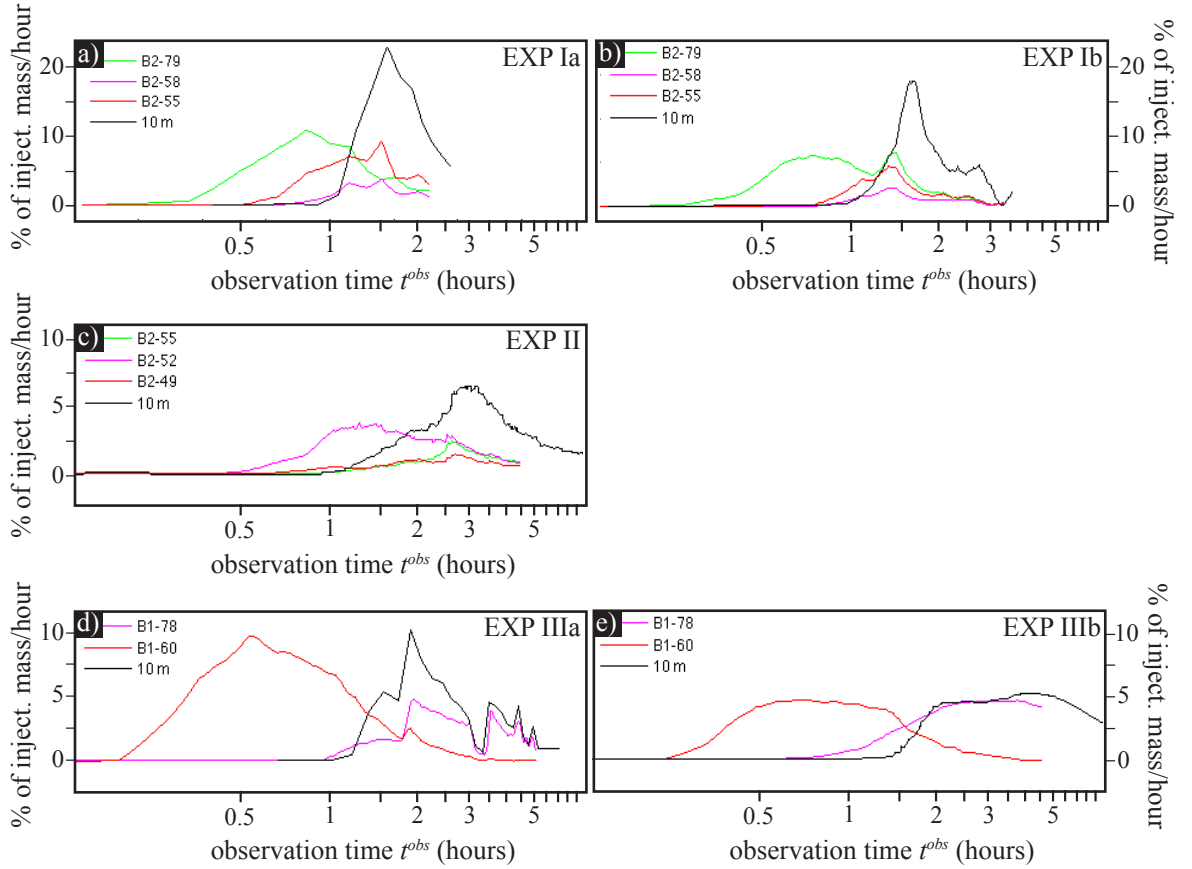


Figure 4.7: Local salt solute flux curves estimated at depth locations with significant tracer arrival (colored lines) and below the pump ($z = 10$ m, black line) normalized by the injected amount of tracer mass for experiments (a) Ia, (b) Ib, (c) II, (d) IIIa and (e) IIIb.

(1) For experiments Ia and Ib (Figure 4.7a and b), the tracer injected in B1-78 arrives after 20 min in B2-79. Additional tracer arrival occurs after 30 min in B2-55 and B2-58 (subtle increase of salinity). Nearly half of the recovered mass comes from B2-79, while $\sim 40\%$ of the recovered mass arrives at B2-55. After the main peak at $t^{obs} \approx 45$ min at B2-79, there

is a second peak in the solute flux curve after ~ 90 min. At the end of the experiment, the total mass recovery is $\sim 25\%$ for both experiments.

(2) For experiment II (Figure 4.7c), the tracer injection in B1-50 gives after 30 min rise to tracer breakthrough in B2 at B2-49 and B2-52. Additional tracer arrival occurs after 60 min in B2-55 and a very small amount of tracer arrives after 2.5 hours in B2-58. The fracture B2-49 contributes with $\sim 20\%$ of the recovered mass, the largest contribution to the total mass ($\sim 50\%$) comes from B2-52. None of these two fractures were detected by Le Borgne *et al.* (2007). About $\sim 20\%$ of the recovered mass arrives at B2-55. The estimated total mass recovery of salt after overnight pumping is $\sim 30\%$. (3) For experiments IIIa and IIIb (Figure 4.7d and e), the tracer injection in B2-55 gives after only 10 min rise to tracer breakthrough in B1-60. Within the first 2 hours, $\sim 40\%$ of the recovered tracer mass arrives at this fracture. After one hour, tracer arrival occurs in B1-78, where $\sim 60\%$ of the total mass is recovered. The total mass recovery at the end of the GPR acquisition experiment is $\sim 20\%$ for experiment IIIa and after overnight pumping $\sim 30\%$ for experiment IIIb. In summary, (1) the estimated solute fluxes from the outflow zones in the pumping borehole are the result of several different fractures or pathways; (2) the mass recoveries are generally relatively low, which we attribute to the ambient flow regime, density effects and the injection conditions.

4.4.2 Single-hole GPR data and difference imaging

Figures 4.8 and 4.9 show, for each of the experiments Ia, Ib and II, five migrated GPR relative-difference sections acquired at different times plotted on top of the migrated GPR sections of Dorn *et al.* (2012a). These images represent changes in reflection amplitudes in a 2-D projection around the borehole (i.e., depth z and radial distance r) with respect to background conditions. Note that the GPR difference-images have a large imprint of the finite source signal. This implies that the fractures in which salinity changes occur are located where the first arriving energy of the reflection wave trains are observed. Figure 4.10 highlights the reflections in the background images that correlate to the high magnitude patterns in the difference sections (Figures 4.8 and 4.9).

Patterns of high magnitudes have predominantly subhorizontal to vertical dips ranging from 30° to 90° (relative to the surface) covering radial distances $r = 2$ -10 m from the pumping borehole. It is not possible to resolve features for $r < 2$ m due to the very high direct wave amplitudes in the corresponding time interval that completely mask the much smaller reflection amplitudes. Subhorizontal patterns show overall weaker amplitudes than subvertical patterns, which can be attributed to the high angle of incidence to the fracture surface. Difference patterns close to the injection point are predominantly imaged with high magnitudes at early times t^{obs} (Figures 4.8a, 4.8f, 4.9a). At depths different than the injection point, patterns with typically weaker amplitudes appear at later t^{obs} and are generally visible for longer time periods. Patterns of evolving difference magnitudes can generally be traced from the injection points through depth intervals ranging over some tens of meters. The GPR difference images

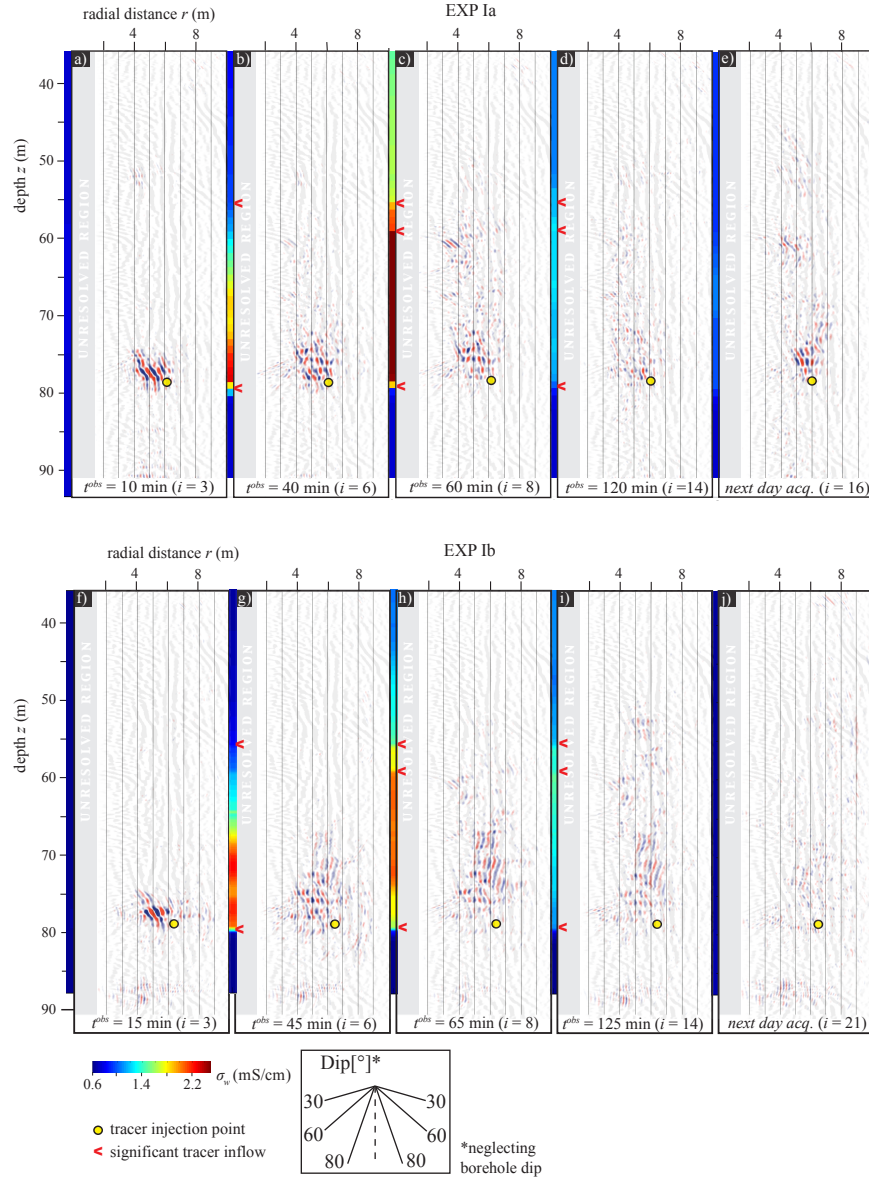


Figure 4.8: Migrated relative difference GPR sections acquired in B2 during experiment Ia (a-e) and experiment Ib (f-j) at different observation times t^{obs} , superimposed on the gray opaque migrated GPR section acquired under natural flow conditions (Dorn *et al.*, 2012a). High difference patterns originate from increased salinity in fractures located at the front of each such pattern (i.e., the smallest radial distance r for each depth z). Note that we do not image any features at $r < 1.5$ m (gray region) because of the dominance of the direct wave at early times and its subsequent removal, which tends to remove superimposed reflections at early times. The corresponding electrical conductivities σ_w of the borehole fluid in B2 are shown in the color profile at $r = 0$ m.

in Figures 4.8 and 4.9 are discussed in detail below together with some of the trends observed at the many intermediate observation times that are not shown (see Table 4.1).

Experiments Ia and Ib

The main difference in experimental design between experiments Ia and Ib is that we did not push the injected tracer with groundwater in experiment Ib after the end of the tracer injection. During tracer injection, pumping conditions were similar for both experiments. We expect significant differences for the tail of the solute flux curves if we push the tracer with groundwater or not, but less for the mean arrival times that are similar for the two experiments (Figure 4.7a-b). The spatial distributions of the GPR magnitude patterns and their evolution over time are similar for the two experiments (Figure 4.8) (the difference amplitudes are plotted with the same scale in all sub-figures). At early times (Ia: $t^{obs} = 10$ min, Ib: $t^{obs} = 15$ min; Figure 4.8a and f), a single high magnitude pattern is visible at $z = 75$ -80 m indicating an upward movement of the tracer from the injection point towards the pumping borehole. At later t^{obs} (Figure 4.8b, c, g and h), new magnitude patterns with dips between 40° and 80° show up in this depth region. The magnitudes get weaker with time and patterns start to appear at shallower depths (up to ~ 50 m depth). Two hours after injection, magnitude patterns for experiment Ia appear patchy and weak (Figure 4.8d), while for experiment Ib they are continuous and moderate in amplitude (Figure 4.8i). The next day acquisition for experiment Ia (Figure 4.8e) does not show weak and random amplitudes as experiment Ib (Figure 4.8j), but a region of moderate amplitudes above the injection point. These remaining amplitudes are partly attributed to unstable overnight pumping.

By overlaying the difference images on the migrated GPR sections of Dorn *et al.* (2012a), we find at least 9 fractures through which the tracer solution likely moved (highlighted fractures in Figure 4.10a). Close to the injection point there are three prominent fractures through which the tracer moves upward (dipping 70° , 75° and 80° between $r = 3.5$ and 7 m). The imaged magnitude pattern close to the pumping borehole at $r = 2$ -4 m and $z = 76$ m, which is dipping 40° is most likely related to the fracture through which the tracer flows into the pumping borehole in B2-79 (Figures 4.7a-b, 4.8a). Between $z = 50$ m and 70 m, the tracer solution moves through at least 4 more fractures, but the connections between these fractures are not always clearly imaged. Most probably, fractures outside of the detection range (with respect to dip and azimuth) carry some of the tracer. Even though tracer arrival at $z = 79.3$ m has been imaged, it is clear from the difference images that the tracer mainly moves upward through a network of connected fractures. This upward movement corresponds well with the later arriving tracer in B2-55 and B2-58 as shown in Figure 4.5a-b. The fractures carrying the tracer into the borehole in this depth interval are probably not imaged because of the low dips. In fact, optical logs indicate dips of 33° and 31° for these fractures. We attribute the less patchy and stronger relative-difference magnitudes in experiment Ib to the tracer solution being spatially more contained compared with experiment Ia. The pushing of the tracer in experiment Ia might have partially pushed the tracer in other directions than the pumping borehole B2, and therefore increased the spreading of the tracer. The overall similarity of the two sets of difference images representing experiment Ia (Figure 4.8a-e) and experiment Ib (Figure 4.8f-j) makes us confident (considering experimental differences) that

the experiments are generally repeatable and the processing scheme can handle the majority of the experimental uncertainties. Furthermore, the dips and locations of the patterns correlate well with previously imaged fractures using multi-offset single-hole data (Dorn *et al.*, 2012a) and hydrogeological studies (Le Borgne *et al.*, 2007). It appears thus that we can identify the main tracer-occupied fractures by superimposing migrated relative difference sections on the migrated multi-offset single-hole GPR data. Nevertheless, the interpretation must consider many intermediate acquisition times to assure that interpreted features are not related to processing artifacts. The interpretation shown in Figure 4.10a is based on careful analysis of the 16-21 difference-images obtained for each experiment (see Table 4.1).

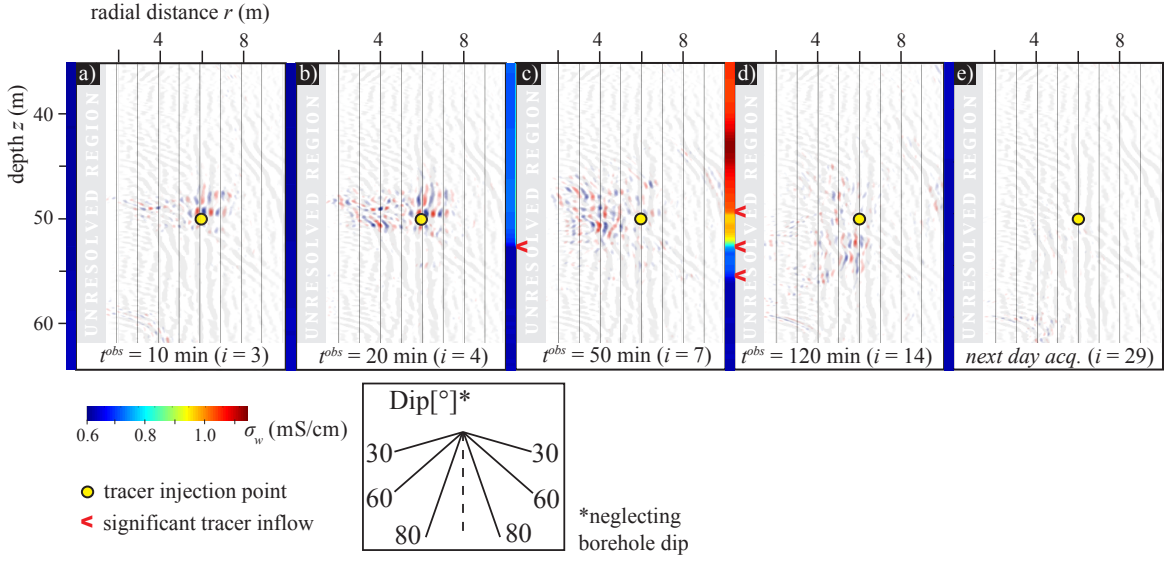


Figure 4.9: Migrated relative difference GPR sections acquired in B2 during experiment II at different observation times t^{obs} , superimposed on the gray opaque migrated GPR section acquired under natural flow conditions (Dorn *et al.*, 2012a). The corresponding electrical conductivities σ_w of the borehole fluid in B2 are shown in the color profile at $r = 0$ m.

Experiments II

The migrated difference images from experiment II (Figure 4.9) show complex magnitude patterns of superimposed reflections that are limited to the depth range of $z = 45\text{--}60$ m. The superposition of different signal contributions and the shallow dips of the fractures through which the tracer appears to move make it very difficult to trace magnitude patterns related to individual fractures. One well-resolved feature is the spatially compact high amplitude pattern above and behind the injection point that is visible at early times $t^{obs} < 50$ min ($z = 47\text{--}50$ m and $r = 5.5\text{--}7.5$ m in Figure 4.9a-b). Polarity changes are found at successive observation times at $z = 49$ m (Figure 4.9a-b), which appear to cut horizontally through this subvertical reflectivity pattern. Rather complex weak-to-high magnitude patterns at smaller radial distances are also seen in Figure 4.9a-c. At $t^{obs} > 50$ min, weak magnitudes appear at

$r = 9\text{-}10$ m in the depth range $z = 45\text{-}48$ m. After 2 h, the magnitude patterns between the injection and pumping boreholes in the depth range $z = 45\text{-}52$ m have weakened considerably and the remaining magnitudes are mostly concentrated in a region below the injection point (Figure 4.9d). The data acquired on the following day does not show any significant remaining relative-difference magnitude patterns, thereby indicating that most of the tracer has left the observable region.

The small differences between the tracer injection depth in B1 ($z = 50.9$ m) and the outflow depths in B2 ($z = 49\text{-}58.9$ m) makes the GPR interpretation difficult as it suggests that flow paths are rather subhorizontal. We find that the difference patterns are largely limited to a region in-between the injection and pumping borehole covering a similar depth interval as the outflow locations. The pattern that is imaged close to the pumping borehole (dipping 30°) around $z = 48$ m is likely related to B2-49 at which the tracer arrives in the borehole. The polarity changes discussed above are also observed in the migrated GPR sections of Dorn *et al.* (2012a). They might originate from nearly horizontal reflection boundaries in-between the boreholes. We have been conservative in interpreting these polarity changes in the difference images as possible tracer transport paths and only indicated one where we could correlate it to the GPR sections by Dorn *et al.* (2012a) (see Figure 4.10b). A possible explanation for the low mass recovery of this experiment is that this horizontal fracture at $z = 48$ m that can be traced over $r = 4\text{-}10$ m carried the tracer away from the injection point to a larger subvertical fracture zone located at larger radial distance ($r = 9\text{-}10$ m) at $z = 45 - 50$ m.

Experiments IIIa and IIIb

Experiments IIIa (Dorn *et al.*, 2011) and IIIb (not shown due to strong similarity with the results of experiment IIIa) indicate a strong influence of the natural gradient. By interpreting the overlaid images, we observe at least 6 tracer-occupied fractures (Figure 4.10c), including a large fracture zone covering a wide depth interval of $z = 40\text{-}65$ m (c.f., Dorn *et al.* (2011)). The saline tracer quickly moves down through two fractures dipping 50° and 75° . The tracer arrives in the pumping borehole through fracture B1-60. Tracer arrivals at greater depths cannot be inferred by our difference images alone as the tracer outflow occurs close to the bottom of the pumping borehole. It is likely that fracture B1-78 carries the tracer to the borehole. This fracture appears to be directly connected to the fractures we observe at $z > 70$ m in experiments Ia-b (Figure 4.10a).

The results in this section clearly demonstrate that the GPR difference patterns are related to transport within connected fractures. Evidence for this is given by the gradual spreading of the GPR difference-patterns away from the injection point (Figures 4.8 and 4.9; Figure 1 in Dorn *et al.* (2011)), the similarity of the inferred patterns for repeat experiments that include the same injection fracture (experiments Ia and Ib in Figure 4.8; experiments IIIa and IIIb (not shown)), and an overall agreement between the timing of the depth intervals experiencing temporal changes in the GPR images (Figures 4.8 and 4.9; Figure 1 in Dorn *et al.* (2011)) and the arrival of saline tracer at the outflow locations (Figure 4.7).

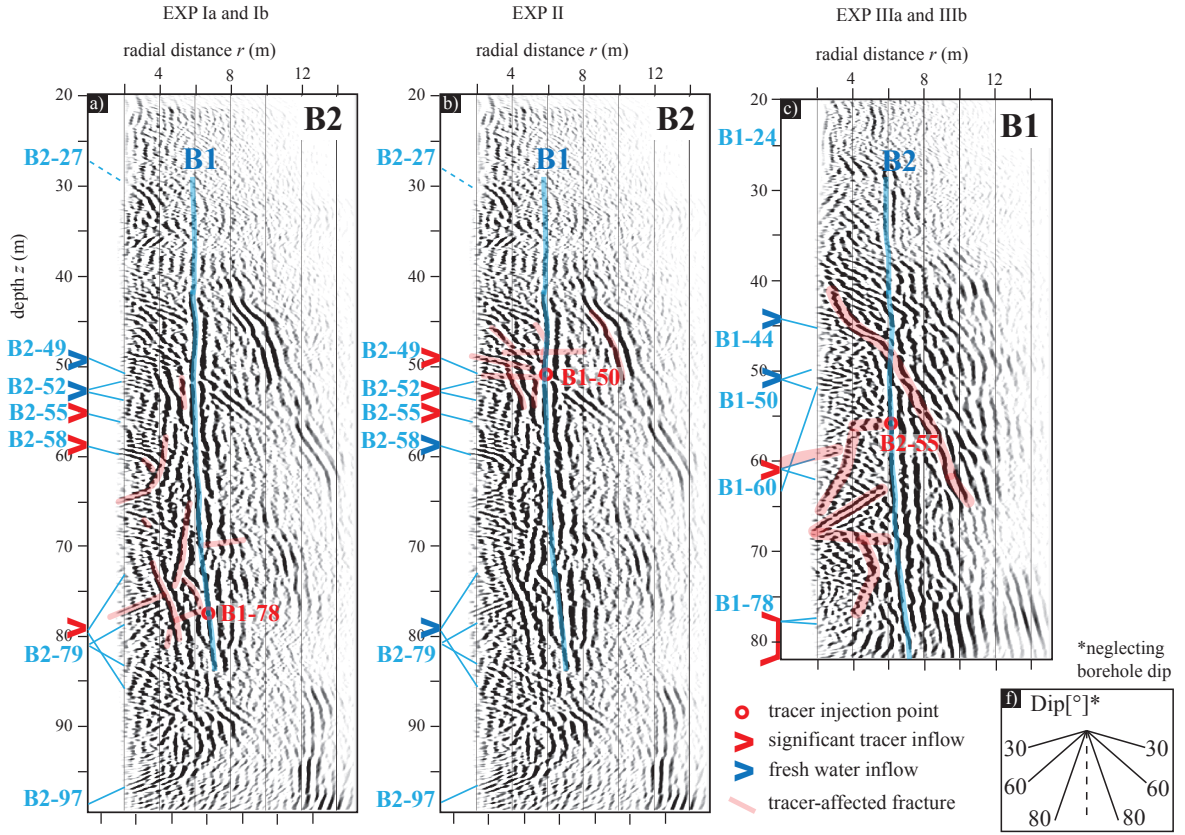


Figure 4.10: Extracts of the migrated multi-offset single-hole GPR sections of B1 and B2 from Dorn *et al.* (2012a) with superimposed interpretations of tracer pathways for experiments (a) Ia and Ib, (b) II, (c) IIIa and IIIb. Red circles indicate the tracer injection points, while red and blue arrowheads locate saline and unaffected groundwater inflow into the pumping borehole, respectively. Light red regions highlight fractures through which the injected tracer is interpreted to move, whereas blue regions highlight reflections from other boreholes. Light blue letters refer to transmissive fractures identified in the boreholes using optical logs and flowmeter tests with corresponding blue lines indicating their corresponding dips (Le Borgne *et al.*, 2007). (f) Dip angles corresponding to the axis aspect ratio $r:z$ of 2:1.

4.5 Comparison of GPR reflection sections with tracer transport modeling

In this section, we investigate in a more quantitative manner the agreement between tracer transport and the GPR difference sections. To do so, we calibrate a fracture model representing experiment Ib using a simplified three-fracture model that only models the main features of the observed mass flux curve in Figure 4.7b. This 3-D model (with 2-D flow in each fracture) is simplistic in that it (1) ignores the azimuths of the fractures, (2) it merges several connected fractures in one large fracture, (3) no heterogeneities of the fractures are considered except for classical dispersion parameters, (4) no density effects are considered, and (5) the natural gradient is ignored. This presented model is clearly very simplified, but it is useful to assess if

changes in the difference sections at chosen locations are consistent with the simulated tracer distributions. We investigate below if discrepancies between the inferred curves are similar to those observed for the simulated and observed solute transport at the outflow locations. If this is the case, we argue that the resulting GPR-inferred reflectivity changes can be used to derive semi-quantitative breakthrough curves at locations between the boreholes.

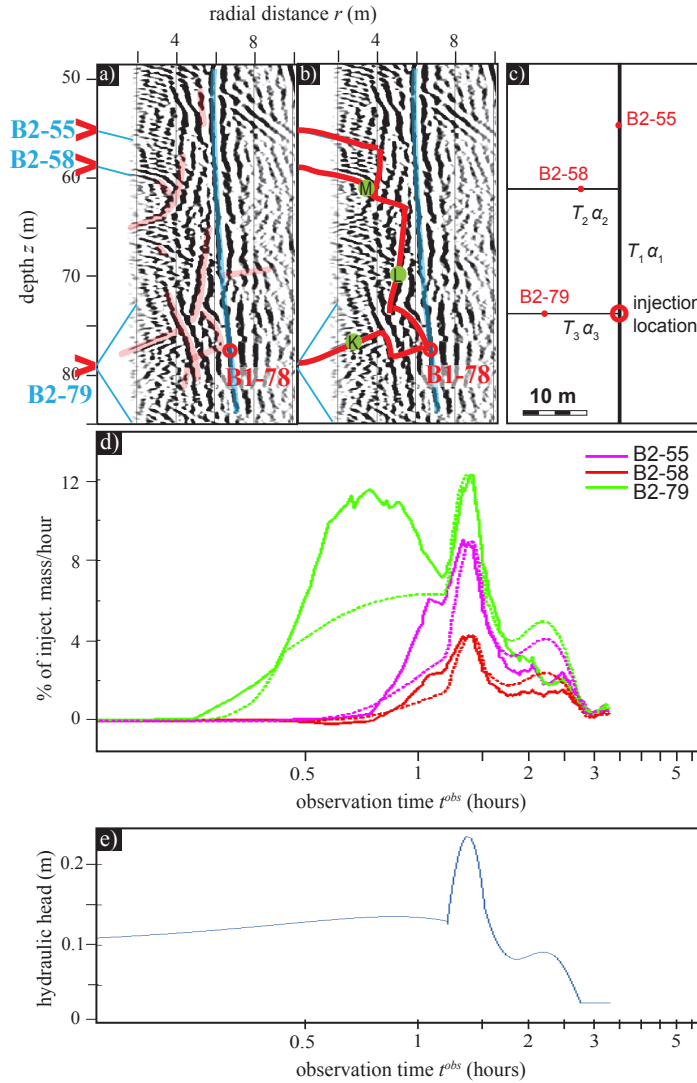


Figure 4.11: Transport model and modeling results for experiment Ib based on a simplified 3-D fracture model with three intersecting rectangular fracture planes with an aperture of 1 mm. (a) Extract of Figure 4.10a, on which we assign (b) three continuous transport pathways between injection and outflow locations. Letters K-M in (b) refer to the positions considered in Figure 4.12. (c) Graph representing a simplified representation of the pathways in (b) used in the transport model to estimate effective hydraulic conductivities k and dispersivities α . (d) Observed (solid lines) and simulated (dashed lines) local salt flux curves at outflow locations B2-55, B2-58 and B2-79. The derived transport parameters are: $K_1 = 0.6$ m/s, $K_2 = 2.3$ m/s, $K_3 = 0.2$ m/s, $\alpha_1 = 0.6$ m, $\alpha_2 = 0.3$ m and $\alpha_3 = 0.2$ m. (e) Hydraulic head used for the boundary conditions at the three outflow locations.

The map of interpreted tracer pathways (Figure 4.11a) for experiment Ib is used as a basis to define continuous transport pathways between injection and outflow locations (Figure 4.11b). The model in Figure 4.11c combines the three transport pathways in Figure 4.11b into three fractures. The distances between outflow and injection locations are inferred from Figure 4.11b. The sketched 3-D fracture planes in Figure 4.11c are modeled with an aperture of 1 mm and an extension of ± 100 m in the out-of-plane dimension. We modeled flow and transport using COMSOL Multiphysics 3.5 using a finite element mesh with 6,200 elements. We solve Darcy's law with the observed time-varying head boundaries in the pumping well for the tracer arrival locations (Figure 4.11e) and use mixed boundary conditions at the injection location (the observed fixed head during the injection period and zero flow conditions afterwards). The edges of the fractures are modeled as zero head boundaries. Using the calculated velocity field, we solve the advection-dispersion equation assuming a constant concentration at the injection location during the injection period. The free fitting parameters are hydraulic conductivities, dispersivity and the concentration as a fraction of the actual injected concentration. The latter allows us to partly consider mass loss and to fit the magnitudes of the observed solute fluxes.

The effective parameters for the three fractures were obtained by manual calibration aiming at fitting the first arrival times and the peak solute fluxes at $t^{obs} \sim 1.4$ hours. An automatic calibration procedure based on a Levenberg-Marquardt algorithm was also used, but did not provide significantly better results. It is clear that the simulated curves in Figure 4.11d (dotted lines) only represent some of the main characteristics of the measured curves (solid lines), which makes the estimated transport properties rather approximate. The derived effective hydraulic conductivities are $K_1 = 0.6$ m/s, $K_2 = 2.3$ m/s and $K_3 = 0.2$ m/s and the dispersivities are $\alpha_1 = 0.6$ m, $\alpha_2 = 0.3$ m and $\alpha_3 = 0.2$ m. The fitted curves underestimate mass fluxes at early arrival times and overestimate them after peak arrivals. Fluctuations in the pressure conditions significantly influence the shape of the modeled flux curves, for example, by reproducing observed peaks at $t^{obs} \sim 1.4$ and 2.3 hours (Figure 4.11e).

The resulting concentration fields were used to calculate how the simulated tracer distributions affect GPR reflectivity. This analysis is based on local tracer concentrations that correspond to the three locations highlighted in Figure 4.11b (green highlighted letters). The concentrations are mapped into σ_w values that we relate to variations of reflection coefficients of thin-layer reflectors using the expression of Deparis and Garambois (2009) under the assumption of a normal incidence wave.

Reflectivity strengths from the GPR difference sections are retrieved at each depth location by picking the maximum value around the chosen location (marked by letters K-M in Figure 4.11b). Figure 4.12 plots the time evolution of these picked reflectivity strengths (asterisks, normalized to the maximum of its fitted second order polynomial) and the estimated reflection coefficients from the simulated concentrations (solid line, normalized to the maximum value). Note that both estimates have been averaged over a 1 m large zone at each location.

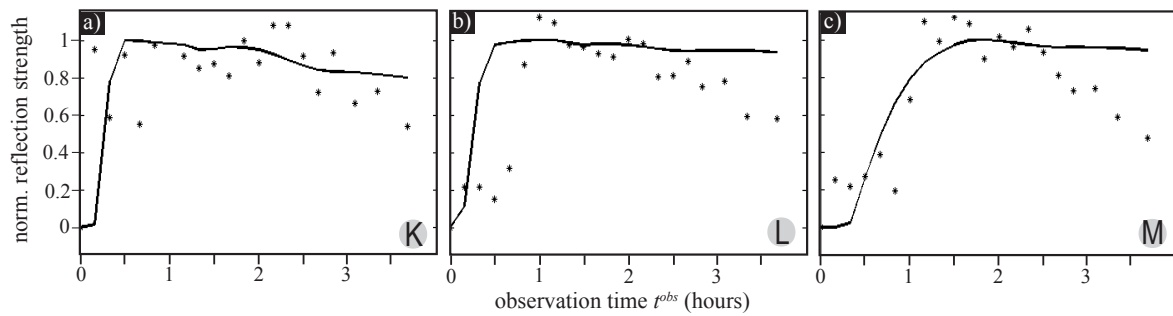


Figure 4.12: Time evolution of normalized reflectivity changes with respect to reference conditions observed in the GPR difference images (asterisks) and calculated from simulated tracer distributions (solid line) corresponding to locations (a) K, (b) L and (c) M in Figure 4.11b. At each location, we average the data over 1 m, but there is no smoothing over time.

Figure 4.12 illustrates that the times at which reflection strengths rise are overall similar for the two estimates. The earliest rise of the reflection strengths are observed for region K (6 m away from the injection point), which is consistent with the observed breakthrough data in that the first arriving mass is found along this flowpath. Reflection strengths are found to rise earlier in region L than in region M, which is consistent with their distance to the injection location (L is 8 m and M is 19 m away from the injection location). The main discrepancy between the curves is that the picked reflection strengths from the GPR difference-images start to go down after ~ 1 -2 hours, which is not seen in the simulated reflectivity coefficients based on transport modeling, except for position K (Figure 4.12a). This is consistent with the discrepancy evoked earlier between the simulated and observed solute fluxes in Figure 4.11d. Indeed, the simulated tracer concentration stay relatively high at the end of the simulations, while both the GPR data and the estimated solute fluxes at the outflow locations indicate that the tracer concentration goes down significantly after the peak arrival.

The results in Figure 4.12 provide evidence that the amplitude changes in the GPR data are directly related to concentration changes within the fractures, which implies that we can obtain relative breakthrough curves for locations between the observation boreholes. Absolute breakthrough curves would require more precise knowledge of the GPR source signal or alternatively a calibration of the radar reflected amplitudes to controlled tracer concentrations as done by Becker and Tsofiias (2010). Another striking aspect of Figure 4.12 is that the picked reflectivity strengths vary relatively smoothly over time. The fact that there is no smoothing applied to the GPR-inferred reflectivity changes over time gives confidence that the GPR data provide information about solute transport at locations within the formation.

4.6 Discussion

The GPR difference amplitude images presented in this work (Figures 4.8 - 4.9) and by Dorn *et al.* (2012a) provide useful complementary information to classical breakthrough data. Although each method has its limitations, we argue that their combination have a high potential

to improve characterization and lead to new insights about tracer transport in fractured media. The main limitations are: (1) breakthrough data provide integrated responses between injection and observation points; (2) the GPR data do not provide information about the region in the intermediate vicinity of the pumping borehole; (3) the GPR data are only 2-D projections imaging those parts of the local fracture planes that have a favorable orientation with respect to the acquisition geometry, and they do not provide information on the azimuth of fractures.

For all tracer injection experiments, we find that multiple transport paths carry the tracer between the injection point and the pumping borehole. This is seen already by considering the distribution of mass rates along the borehole (Figure 4.7), but the GPR difference images offer a more complete view of fracture connections and transport pathways between the two boreholes (Figures 4.8 and 4.9; Figure 1 in Dorn *et al.* (2011)). In all experiments, we find that the depth intervals and the timing of the GPR magnitude patterns agree well with the calculated mass rates. We see similarly located magnitude patterns in experiments Ia and Ib (Figure 4.8), as well as in experiments IIIa and IIIb (not shown). The patterns appear at slightly different times due to differences in the experimental setup (e.g., in terms of the pumping and injection rates). The similarities of the two sets of difference images obtained from repeat tests using the same fracture for injection make us confident that the experiments are repeatable and the processing scheme is robust. Our results suggest that it is possible to identify the main tracer-occupied fractures over time by superimposing migrated relative difference sections on the migrated GPR sections from B1 and B2 acquired under natural flow conditions (Dorn *et al.*, 2012a). When comparing these images, it seems that the most prominent fractures imaged by Dorn *et al.* (2012a) also carry tracer in the saline tracer experiments. The GPR difference images provide us with a plausible explanation about where the unaccounted mass went. For the experiments presented herein, it seems that most of the missing mass was transported from the injection point in a direction away from the pumping boreholes and the observable region, while some storage or delay in less mobile zones may have occurred.

When interpreting these results, it is important to consider that the GPR relative-difference images provide an incomplete description of tracer movement as the fracture azimuth is unresolved, but also because certain fractures that carry tracer will not be imaged. These include small-scale fractures (i.e., with a fracture surface smaller than about the first Fresnel zone (0.6 m at $r = 2$ m and 2 m at $r = 20$ m)), fractures with subhorizontal dips, fractures with an unsuitable azimuth, and fractures located close to the boreholes. We observe dips of fractures at all detectable angles (considering that only dips between 30° - 90° are detectable), the most common dip being around 30° . The recorded GPR difference-amplitudes are surface-averaged measures (over the first Fresnel zone) of electromagnetic contrasts, which imply that the difference images have a limited sensitivity to tracer dispersion within a single fracture. Still, in fractures that are imaged in the difference sections it is very likely that spreading within the fractures occur at least on the meter scale.

Differences in the experimental setup lead to observable differences in the temporal and spatial dynamics of the tracer transport. First of all, the pathways but also the ratios between

the imposed heads and the upward natural gradient differ: In experiments Ia and Ib with an injection rate on the order of the natural gradient, the tracer moves upwards and spreads over tens of meters (Figures 4.8 and 4.10a), in experiment II with again an injection rate on the order of the natural gradient, the tracer moves subhorizontally (Figures 4.9 and 4.10b); and in experiments IIIa and IIIb where the injection head is roughly three times stronger than the natural gradient, the tracer moves partly downwards and spreads over tens of meters (Figure 1 in Dorn *et al.* (2011) and Figure 4.10c). We observe multiple peaks in the solute flux inferred at different fracture locations (e.g., in B2-79 at $z = 79.3$ m for experiments Ia and Ib, Figure 4.5a-b) that are attributed to variations in the pumping rates as we see similar behavior in the simulated breakthrough curves of experiment Ib (Figure 4.11d).

For our experimental setup we have to note that the relative contributions to flow and mass of a given fracture depend on overall connectivity with the permeable fracture network, whereas the mass contribution depends on the local connections with the injection fracture. In experiment II, most of the mass arrives through a fracture that does not contribute significantly to flow (in B2 at $z = 52.7$ m). In fact, this fracture was not even identified by Le Borgne *et al.* (2007) when analyzing flowmeter data from the site. In experiments IIIa and IIIb, the recovered mass is arriving nearly in equal parts at two fractures located 22 m apart, one contributing with 80% and the other <5% to flow.

The mass recovery is low (<30%) in all experiments. The tracer might move out into fractures that carry the tracer away from the pumping borehole either due to the ambient flow field, by density effects or by the injection pressure. The pushing of the tracer by continued water injection in experiments Ia, II, IIIa and IIIb likely pushed some of the tracer away from the pumping borehole. In these cases, the pumping might only weakly affect the tracer and its subsequent movement. The regional upward gradient that is manifested by a ~ 1.5 L/min flow in the boreholes (Le Borgne *et al.*, 2007) seems to influence the tracer movement for some of the experiments, for which we observe significant upward movement of the tracer into larger fracture zones (experiments Ia-b and IIIa-b).

Tracer transport between the two ~ 6 m distant boreholes is fast for the experiments presented here. Tracer breakthrough occurs during the first hour in all experiments and peak concentrations in the borehole fluid are observed after 30 min (experiments Ia and Ib, Figure 4.5a-b) to 3 hours (experiment II, Figure 4.5c). Correspondingly, the GPR difference images evolve quickly in time during early observation times. The corresponding apparent tracer velocities considering the length of the 2-D projected pathway between injection and outflow locations in Figure 4.10 and the minimal tracer travel time give estimates in the range of 0.2-1.3 m/min. These velocities of the first arriving tracer are likely higher as the actual travel path length in 3-D is larger.

A comparison between picked GPR reflectivity changes at specific locations over time with those inferred from flow and transport modeling (Figure 4.12) show a good agreement at early times and discrepancies at late times, indicating that a more complex flow and transport model could be constrained with these data. The discrepancies are on the same order as those

between observed and simulated solute fluxes at the outflow locations using the same flow and transport model. The time-series of GPR reflectivity changes have a high signal-to-noise ratios and indicate not only the arrival time of the saline tracer at a specific location, but also how the tracer concentration decreases over time. Forced tracer tests examine only the fractures that are involved in tracer transport and does not represent natural conditions. To better understand and build models for predicting flow and transport under natural conditions one must carry out experiments under natural flow conditions. Using single-hole GPR difference imaging as presented here offer the possibility to image transport under such conditions even in the case of no or very limited tracer arrival in the boreholes.

The resulting GPR difference sections are a result of a rather extensive processing workflow. Research is warranted to better understand under what conditions this type of data can provide reliable information about transport within specific fractures and how to best use such data to constrain realistic 3-D fracture network models that honor not only borehole information, but also transport pathways, effects of natural flow gradients, and storage changes imaged by the GPR data. To facilitate the interpretation of the difference-migrated images, it would be most fruitful to test and further develop suitable deconvolution algorithms that remove the imprint of the GPR source signal (Schmelzbach *et al.*, 2011).

4.7 Conclusions

We find that time-lapse single-hole GPR data acquired during saline tracer injection tests provide insights about the temporal evolution of tracer plume geometry that is complementary to information derived from classical hydrological characterization of fractured aquifers. The GPR data make it possible to derive a length scale of the fractures involved in the tracer transport and to infer the connectivity and geometry of these fractures. Furthermore, the data help to better understand where the tracer that did not arrive in the pumping boreholes went. For five tracer experiments in a fractured granite, we find that the GPR data acquired with 250 MHz antennas provide subtle but reliable images of the evolution of tracer plumes through time at radial distances $r = 2 - 10$ m from the boreholes (Figures 4.8 - 4.9). Hydrological data and migrated relative difference amplitude images derived from the GPR experiments are consistent with each other and indicate similar tracer transport characteristics for the experiments that involved the same injection fracture. For all experiments, we find that multiple pathways involving several fractures connect the injection fracture with the pumping borehole and that the total vertical spread of the tracer is in the range of tens of meters despite that the two boreholes are only located six meters apart. The vertical ambient pressure gradient at the site seems to carry most of the injected tracer upwards through fractures that do not intersect the pumping boreholes, while some storage of tracer mass appears to occur in less mobile zones within the inter-borehole region. We find that 2-D geometrical information about pathway lengths and connections help to constrain breakthrough analyses. We demonstrate also for one of the experiments using a simplified fracture model how GPR

reflectivity time-series at chosen locations may be used to test and provide further constraints to transport models.

Chapter 5

Stochastic Generation of 3-D Connected Discrete Fracture Networks Conditioned to Hydrological and GPR Reflection Data

Caroline Dorn, Niklas Linde, Tanguy Le Borgne, Olivier Bour, Jean-Raynald de Dreuzy

in preparation for *Advances in Water Resources*

5.1 Abstract

The geometry and connectivity of fractures exert a strong influence on flow and transport properties of fracture networks. We present a new approach to stochastically generate three-dimensional discrete networks of connected fractures conditioned to hydrological and time-lapse ground-penetrating radar (GPR) reflection data. Interpretations of GPR images and optical borehole logs are first used to define the number and a probabilistic distribution of fracture geometry. A hierarchical direct sampling algorithm is then used to draw realizations from the posterior distribution at different levels of conditioning. The method is applied to a well-studied granitic formation using data acquired within two boreholes located 6 m apart. The hydraulic borehole logs and time-lapse GPR data indicate that, at least, 30 fractures are part of the connected network sensed by three tracer experiments with injection in different fractures. The prior models include the 30 fractures with their geometry (position and orientation) bounded by information from optical televiewer logs and static GPR data. Eleven cross-hole hydraulic connections between the boreholes, their relative hydraulic importance, and inferred topological constraints on the network provided by time-lapse GPR data are then used for conditioning to derive the posterior set of fracture models. We analyze a set of ~ 200 posterior realizations that reproduce all observed hydrological and GPR reflection data given their uncertainties. These models provide valuable statistics on length scales and density of connected fractures, as well as their connectivity. The resulting fracture networks lead (despite a uniform fracture transmissivity) to variations in cross-hole flow properties between realizations on the order of one magnitude. The posterior model space is strongly determined by the prior bounds obtained by highly informative GPR and televiewer data and their use is crucial to make the proposed stochastic inversion scheme feasible in practical applications. Among the conditioning data considered, we find that the topological constraints inferred from time-lapse GPR were the most useful in further constraining the variability of the network realizations.

5.2 Introduction

The characterization of flow, storage, and transport properties in fractured rock formations is a most difficult problem. The challenge resides mainly in the extreme heterogeneity of fractured formations, in which hydraulic conductivities vary over many orders of magnitudes within very short distances. Furthermore, flow and transport in fractured systems are highly organized, with flow channeling within fracture planes and preferential pathways within the connected fracture network (e.g., Neretnieks, 1993; Smith and Schwartz, 1984). Direct measurements of hydraulic or geometrical properties of all individual fractures are impossible, and the data coverage in field investigations is typically very low compared with the underlying heterogeneity. One solution to this problem is to derive effective bulk hydraulic properties at a scale corresponding to the support volume of the data (Maréchal *et al.*, 2004). But the use of bulk hydraulic properties to characterize fractured rocks has been widely criticized, as it

implies the existence of a homogenization scale (Berkowitz, 2002; Neuman, 2005). Ongoing research focuses on the hydraulic and geometrical characterization of fracture networks (e.g., network permeability, fracture density, fracture length distribution), of individual fractures (e.g., position, location, orientation, transmissivity) and their connectivity (e.g., Berkowitz, 2002).

Hydrological investigations of fracture rock aquifers often include flowmeter and tracer tests (e.g., Harvey and Gorelick, 2000; Day-Lewis *et al.*, 2006; Le Borgne *et al.*, 2007). These tests allow investigating hydraulic properties and dispersive phenomena for transmissive networks that can be sensed from measurement locations in boreholes. Hydraulic cross-hole connections can be investigated using tracer or flowmeter tests (except for single-hole flowmeter tests or slug tests, they generally necessitate time-consuming packer systems) (e.g., Paillet, 1998). Single-hole flowmeter tests provide information about the contribution to flow of a specific fracture observed in a borehole with respect to all outflow locations. Flowmeter and tracer tests provide averaged hydraulic estimates for the investigated hydraulic connections, which might comprise many fractures with complex connectivity patterns. Inferring hydraulic characteristics of the individual fractures is most often impossible. Even extensive packer tests used to produce hydraulic tomographic images fail to resolve individual fractures (Hao *et al.*, 2007).

Geophysical investigations in fractured rocks have demonstrated the value added of single-hole GPR reflection data in providing constraints on the geometry of individual fractures (e.g., Olsson *et al.*, 1992; Dorn *et al.*, 2012a). The geometrical properties of single fractures at the field scale, such as their location and orientation relative to the borehole can be constrained from GPR images (e.g., Tsoflias *et al.*, 2004; Olsson *et al.*, 1992; Grasmueck, 1996). Compared with other geophysical methods that are used in fractured rock investigations, GPR is the most favorable tool to resolve individual fractures away from the boreholes. Seismic methods, for instance, typically employ sources with a resulting larger wavelength and the acoustic impedance contrast is less pronounced than the electromagnetic impedance in most fractured rock environments (e.g., Mair and Green, 1981; Khalil *et al.*, 1993). The resolution of electrical resistivity tomography is insufficient to identify individual fractures (Day-Lewis *et al.*, 2005), but this is also the case for many other types of geophysical data when interpreted by smoothness-constrained inversion (such as seismic or GPR attenuation or travel time tomography; e.g., Day-Lewis *et al.* (2003); Ramirez and Lytle (1986); Daily and Ramirez (1989)).

Surface-deployed GPR can be used to image shallow dipping fractures (e.g., Grasmueck, 1996), whereas borehole acquisitions can be used to image rather steeply dipping fractures (e.g., Olsson *et al.*, 1992). Tsoflias *et al.* (2004) found that vertical fractures can also be detected with surface-based GPR measurements when using the polarization properties of electromagnetic waves. The possibility to use different GPR polarizations in borehole applications does not exist in commercial systems. Sato and Miwa (2000) developed a polarimetric borehole radar system and showed that the polarization properties of fractures can be related to their roughness. Borehole GPR reflection data can either be acquired in single-hole or cross-hole

mode, but single-hole mode appears generally to be the most informative (Dorn *et al.*, 2012a). Common borehole radar systems emit omni-directional radiation patterns (symmetry around the borehole axis), which precludes the determination of azimuths of plane reflectors when using data from one borehole alone. Directional antennas that were originally developed for the characterization of prospective nuclear waste depository sites, have only recently become more widely developed, but are still not commonly used (Slob *et al.*, 2010).

The deployment of GPR monitoring during tracer tests is useful to identify those fractures that are transmissive and connected to the injection point. Tracer movements can thus be imaged in individual fractures away from the borehole locations (e.g., Talley *et al.*, 2005; Dorn *et al.*, 2012b). In the following, we refer to this data type as time-lapse GPR data.

The accessibility of fractured rock investigations are typically restricted to borehole locations. This restriction has important consequences, in that the orientation of fractures can be well resolved at the borehole locations (using optical televiewer logs), but only within significant uncertainty ranges away from the borehole (e.g., using GPR reflection images) (Olsson *et al.*, 1992; Dorn *et al.*, 2012a). Furthermore, hydrological and geophysical data generally constrain different aspects of the same target, namely hydraulic and geometrical properties, respectively. The integration of different data types can help to overcome some of the limitations commonly encountered when characterizing fracture networks. As both hydrological and geophysical data and their interpretations contain considerable uncertainties, they should be carefully taken into account within a formal data integration procedure.

The use of geophysical data in building aquifer models have been investigated in a series of studies (e.g., Hubbard *et al.*, 1997; Gallardo and Meju, 2007; Linde *et al.*, 2006b; Day-Lewis *et al.*, 2000; Chen *et al.*, 2006). Many successful examples of deterministic integration methods exist that determine hydraulic and structural properties of unconsolidated materials (e.g., Looms *et al.*, 2008; Doetsch *et al.*, 2010), but fewer examples consider fracture rock systems (e.g., Day-Lewis *et al.*, 2003; Linde and Pedersen, 2004). Deterministic inversion algorithms seek one model that fits the data, while deviating the least from preconceived conceptions. Their applicability may be limited for highly non-linear problems as the typically used gradient-based optimization techniques may get trapped in local minima and they provide limited insights about model variability (e.g., Tarantola, 2005). Stochastic approaches are suitable when it is expected that very different models (e.g., in terms of fracture geometries) are possible given the available prior information and data, as they may explore the posterior probability density functions. The description of data errors are also more flexible and their effects on the model estimates can be accurately taken into account (Mosegaard and Tarantola, 1995). Stochastic sampling-based approaches for high dimensional problems (e.g., hundreds of parameters are extremely computationally expensive). This means that it is imperative to decrease dimensionality and model space as much as possible before applying this type of methods.

Numerous global search methods exist, for example Markov chain Monte Carlo methods (MCMC), simulated annealing or genetic algorithms. The most common family of meth-

ods today are those based on MCMC (e.g., Hastings, 1970; Mosegaard and Tarantola, 1995; Laloy and Vrugt, 2012). Day-Lewis *et al.* (2000) successfully conditioned the 3-D geometry of fracture zones to hydraulic data using a simulated annealing approach. Chen *et al.* (2006) used MCMC sampling to estimate probabilities of zones having high hydraulic conductivities. Markov chain Monte Carlo methods generate parameter samples that converge to a stationary distribution that coincides with posterior probability distribution under certain conditions (e.g., Hassan *et al.*, 2009; Chen *et al.*, 2006). MCMC methods can be inefficient for discrete fracture networks (DFN) for which small changes in fracture geometries might lead to very different responses (i.e., a small perturbation in the model space leads to dramatic changes in the data space). Other challenges associated with MCMC methods are how to determine the accurate convergence of the chain and how to sample independent realizations, as neighboring positions in the chain do not represent independent draws from the posterior distribution. One method that does not have those limitations is the direct sampling method, which is the only exact and also the simplest global search method (Mosegaard and Tarantola, 1995).

To investigate the 3-D heterogeneity of fracture networks, the stochastic generation of possible DFN models (e.g., Darcel *et al.*, 2003) conditioned to available data is appealing. The conditioning of DFN models to borehole observations (e.g., Darcel *et al.*, 2003) is a common approach, but its utility has been questioned given the difficulty in correlating fracture aperture at the borehole locations to hydraulic apertures (Renshaw, 1995) and the limited coverage of borehole data with respect to the investigated rock volume (Neuman, 2005). DFN approaches are predicated to statistical data of fracture distributions, but reliable statistics are very difficult to obtain. To partly circumvent these problems, we propose herein to condition connected DFN models to hydrological and GPR reflection data sensitive to hydrological state variables.

The posterior set of conditioned fracture models can be used to evaluate fracture network statistics. Fracture properties (e.g., length, aperture) of DFNs are usually described using concepts that imply power laws, fractals or scale-variant distributions. Reliable estimation of power law exponents and fractal dimensions based on field data is challenging, as spatial field measurements on outcrops or in boreholes cover generally not more than two orders of magnitudes. The geometries of fractures are often studied by means of fracture intensity profiles that are often restricted to borehole logs (and surface observations) and they must be corrected for their non-uniform sensitivity over the possible dip ranges of fractures and higher weathering near the surface (Davy *et al.*, 2006; Darcel *et al.*, 2003; Terzaghi, 1965). The underlying distribution of fracture lengths and orientations strongly influence the network connectivity (e.g., Kogut and Straley, 2001). The state of connection of a DFN is statistically determined by the percolation parameter. The percolation threshold above which the probability of having a connected path in a system is always 1 depends on the dimensionality of the system, the shape of fractures and the underlying fracture distribution. Networks with longer fractures reach the percolation threshold at lower fracture densities than those involving shorter fractures. Our work focuses on the connected portions of fracture networks, which implies that we are working with fracture networks above the percolation threshold. A connected network

generally consists of fractures that are part of the backbone (i.e., the fractures through which the most significant fluid flow occurs) and dead-end fractures that do not conduct significant amount of fluids.

The first contribution of this paper is to present a stochastic simulation method to generate 3-D fracture models conditioned to both hydraulic and geophysical data. We then investigate in a field-setting how these different sources of data contribute to the characterization of the local connected DFN. The geophysical images are shown to be very helpful in determining the number of fractures and to restrict the prior distribution of fracture parameters and thereby significantly reducing the model space. Hydraulic connection data and topological constraints are used for conditioning within a hierarchical direct sampling Monte Carlo scheme that allows drawing samples from the posterior distribution. We apply our scheme to data from the Stanger-Brune site in France, where a small fraction of well-connected fractures appear to control the flow. More specifically, we derive 3-D descriptions of connected fractures by combining (1) logging data together with (2) a few fundamental geometrical properties of connected fracture networks, (3) images of fractures obtained from GPR data acquired under natural conditions and during tracer test, (4) topological constraints based on the interpreted time-lapse GPR data, and (5) hydrological information (e.g., tracer arrival times, massflux curves) acquired during tracer tests.

5.3 Methodology

Within this study, we generate and condition connected DFN models under the assumption of an impermeable rock matrix. Fractures are simplified as homogenous thin circular discs distributed in a 3-D space, where each fracture is parameterized with a midpoint (x, y, z) , a dip (φ) , an azimuth (θ) and a radius (R) . The same constant transmissivity is assigned to all fractures. The proposed framework is general though and it would be straight-forward to include additional parameters, such as individual fracture transmissivities. The model describing the geometry of all individual fractures in a given model is defined in a vector \mathbf{m} . A series of observed hydrological and geophysical data \mathbf{d}_{obs} at a field site stems from the noise-contaminated response of a true and unknown system that may be described by a parameter vector \mathbf{m}_{true} . For a perfect theory, the model vector \mathbf{m}_{true} can be uniquely mapped to the data space by solving appropriate forward problems. The goal of the stochastic data integration or joint inversion procedure is to draw samples from a distribution $p(\mathbf{m})$ describing prior constraints on the model space that also explain site-specific data \mathbf{d}_{obs} within data and modeling errors, such that they are draws from the posterior distribution $p(\mathbf{m}|\mathbf{d})$. The agreement between calculated data \mathbf{d}_{cal} and observed data \mathbf{d}_{obs} is evaluated by a likelihood function $L(\mathbf{d}|\mathbf{m})$. This integration of information can be formalized through Bayes theorem that describes how to derive $p(\mathbf{m}|\mathbf{d})$ given the prior probability density $p(\mathbf{m})$ and the likelihood function $L(\mathbf{d}|\mathbf{m})$

$$p(\mathbf{m}|\mathbf{d}) = \text{const } p(\mathbf{m})L(\mathbf{d}|\mathbf{m}) \quad (5.1)$$

where *const* is a normalization constant (e.g., Mosegaard and Tarantola, 1995). Many different methods have been developed to derive $p(\mathbf{m}|\mathbf{d})$. Direct sampling is the only exact Monte Carlo sampling technique where each accepted model is a random draw from $p(\mathbf{m}|\mathbf{d})$. This simple method draws proposals directly from the prior distribution and their acceptance is decided by the value of the likelihood function alone, that is, there is no comparison made with previous proposals, as in MCMC.

A suitable metric is needed to compare simulated and observed data for a proposed model. We use the l_∞ norm, that is applicable if the error bounds are strict (Marjoram *et al.*, 2003), but other norms such as l_1 or l_2 norms could also be used. A model is in the case of the l_∞ norm accepted if all the residuals are within the uncertainty bounds of the observed data. The likelihood function is thus either zero or one with discrete jumps in between. It has a complex topology for fracture networks whose connectivity may change significantly with only small perturbations in fracture geometry.

Because we consider different types of conditioning data it is necessary to perform different types of forward simulations to evaluate the responses of proposed models. It is common that the associated computational costs are very different (e.g., flow simulations are computationally more expensive than evaluations of hydraulic connections). In order to keep the computational costs as low as possible, we apply a hierarchical formulation of Bayes theorem (e.g., Glaser *et al.*, 2004), in which the posterior distribution at one conditioning level is subsequently evaluated at the next level for other types of observational data. Time-consuming simulations of proposed models are thus only performed on models that are in accordance with data types for which quick simulation tools are available.

Direct sampling can be very slow in high dimensions when dealing with large data sets with small errors (i.e., the probability that a random draw fits all the data is prohibitively low). This work applies therefore primarily to instances when there are comparatively few data and when data or modeling errors are rather large. We argue that this is often the case in fractured rock investigations. Furthermore, the definition of the prior distribution is crucial to make the direct sampling approach feasible. For example, it is important to constrain how many fractures are part of the connected DFN and their respective positions to some extent. This leads to a somewhat unorthodox use of the prior, as it relies on certain site-specific data sets (albeit, not further used as conditioning data in the likelihood function). This implies that the properties of individual fractures are largely constrained by the definition of prior bounds and that subsequent conditioning is mainly done to assure that the proposed models are in agreement with available data that characterize the behavior of the whole fracture network (e.g., hydraulic cross-hole connections) that are difficult to include in the prior density function.

To demonstrate the methodology, we consider a set of classical hydrological data: optical televiewer logs, flowmeter data and tracer test data. Furthermore, we use single-hole GPR data that provide geometrical constraints on individual fractures that are part of the connected fracture network (Dorn *et al.*, 2011, 2012b). Indeed, the method capitalizes through its model parameterization on a very detailed description of the fracture geometry derived from GPR

imagery. As discussed above, it is of primary interest to take the uncertainty of the different data types into account. The different data types and their uncertainties are described in the following.

(1) Optical televiewer logs constrain the intersection depth, dip and azimuth of transmissive fractures that intersect the boreholes. The uncertainties of these estimates are mainly related to the interpreters identification of the fractures, the depth positioning error of the tool (cm-range) and the accuracy at which the borehole deviations are determined (about 0.5° for the inclination, and 1° for the azimuth). Furthermore, it is difficult to assess from borehole logs alone how well the local dip and azimuth at the borehole-fracture intersection represent the mean orientation of the entire fracture plane. In granite formations, Olsson *et al.* (1992) and Dorn *et al.* (2012a) found similar dips of fractures identified at the borehole locations and fractures imaged by GPR reflections.

(2) Hydraulic and tracer tests are generally used to identify and hydraulically characterize the fractures that intersect boreholes (and implicitly the connected fracture network). Single-hole and cross-hole flowmeter testing allow inferring hydraulic connections. Besides the resolution of the flowmeter tool (e.g., < 0.3 m/min for impeller flowmeters), the uncertainties are related to the uncertainties of the imposed hydraulic gradient and the influence of natural flow. Massflux curves acquired at outflow locations during tracer tests depend on the accuracy of the logger and calibration data, but experimental conditions often pose further limitations.

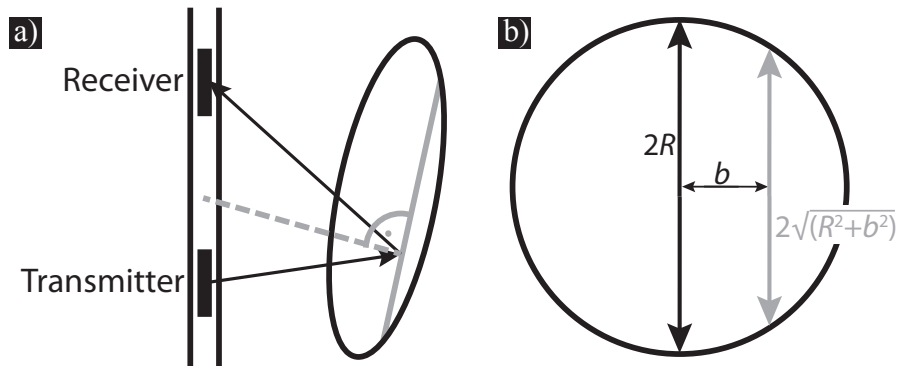


Figure 5.1: (a) Schematic of a simplified circular fracture plane with radius R and the chord (in grey) on which normal vectors may exist that intersect the borehole location (depending on the azimuth and the location of the fracture relative to the borehole) and thus allow the fracture chord to be imaged with GPR. (b) Plane view of fracture. The distance b is undetermined.

(3) Single-hole GPR reflection imagery provides very useful constraints on (i) the spatial extents of fractures that intersect a borehole (with intersection points determined from televiewer data) and (ii) geometrical attributes of fractures that do not intersect a borehole (e.g., Olsson *et al.*, 1992; Dorn *et al.*, 2012a). Commonly used omni-directional GPR antennas provide 2-D projections (there is a circular symmetry along the borehole axis) of reflectors corresponding to fracture chords. These chords represent the parts of a fracture where normal vectors exist that cut the observation borehole location (Figure 5.1). Due to the dipolar-type radiation pattern of GPR antennas, in which most of the energy is radiated normal to the

borehole axis, GPR imagery is practically limited to fractures dipping between 30° and 90° with respect to the observation borehole. Fractures are typically observed in the range of few meters to some tens of meters away from the borehole, depending on the antenna frequency used and the electrical conductivity of the host rock. There is a lack of information concerning the first meters around the borehole, as this region is strongly dominated by the direct wave that masks early reflections from close-by fractures.

The positioning of a fracture from its imaged fracture chord is affected by uncertainties of the GPR velocity used for migration, the picking error when interpreting reflections from migrated images (\sim a quarter wavelength), the size of the first Fresnel zone (depends on the radial distance r and the signal frequency), and how far the midpoint of the imaged chord lies away from the midpoint of the fracture plane (distance b in Figure 5.1). For a fracture identified in a migrated single-hole GPR image, we can attribute a minimal and maximal extent in depth z and a radial distance r , which implies that the dip angle is indirectly defined. The positioning uncertainties of GPR-imaged fractures that are also identified at their intersections with the borehole by televiewer logs are different. For those fractures, we assign dip and strike angles, depth of borehole intersection, and its minimal and maximal extent in depth. Time-lapse GPR imagery used to monitor tracer movements makes it possible to identify fractures that are connected to the tracer injection fracture. At a field site in fractured granite, Dorn *et al.* (2011, 2012b) showed that only a fraction (below $\sim 20\%$) of the GPR-identified fractures are actually well-connected to packed-off injection locations in the borehole. Due to the influence of natural pressure gradients, those connected fractures are not necessarily part of the flow path that is established by the imposed hydraulic gradient. In the present study, we do not account for the fact that the same fracture might be identified in GPR data from different boreholes. This assumption will be relaxed in the future.

5.4 Field application

Field site

We apply our hierarchical direct sampling scheme to data acquired in the well-studied Stang-er-Brune aquifer test site in Brittany, France, to derive a relatively large set of connected DFN models that all describe observations in the vicinity of two ~ 6 m spaced boreholes B1 (83 m deep) and B2 (100 m deep). The site is a crystalline rock aquifer consisting of saturated granite overlain by 30-40 m of highly deformed mica schist. The granite formation has the most permeable fractures (Le Borgne *et al.*, 2007) and is the area of primary interest.

Available data

Le Borgne *et al.* (2007) found that the formation at Stang-er-Brune is highly transmissive with overall hydraulic transmissivities on the order of 10^{-3} m²/s over the length of each borehole. An ambient vertical pressure gradient resulting in an upward flow in the boreholes of about 1.5 L/min in each borehole is also expected to affect the flow in the local fracture network. From

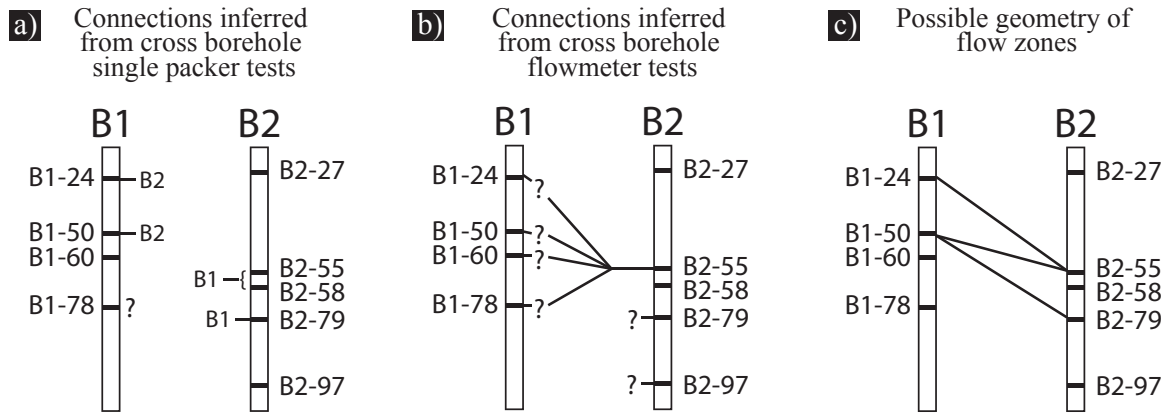


Figure 5.2: Synthesis of the hydraulic connections between B1 and B2 inferred from (a) single packer tests and (b) cross-borehole flowmeter tests. (c) Possible hydraulic connections at the Stang-er-Brune site inferred from the comparison of (a) and (b). Adapted from Le Borgne *et al.* (2007).

flowmeter and packer tests, Le Borgne *et al.* (2007) identified most of the borehole-intersecting fractures that are part of the transmissive fracture network. There are only 4-5 such fractures in each borehole over the thickness of the granite formation. In general, these fractures have dips in the range of 30-80° and azimuths in the range of 190-270°. None of these identified fractures intersects both boreholes B1 and B2 (Le Borgne *et al.*, 2007; Belghoul, 2007). Possible hydraulic inter-borehole connections at the site inferred from a combination of single packer tests and cross-borehole flowmeter tests were presented by Le Borgne *et al.* (2007) and are depicted in Figure 5.2.

With the objective of imaging the local fracture network within the granite formation away from the boreholes, Dorn *et al.* (2012a) acquired 100 MHz and 250 MHz multi-offset single-hole GPR data. In the following, we refer to this data as static GPR data as they were carried out without imposing any perturbations to the hydrological system by pumping or tracer injections. The majority of fractures that were identified as being transmissive by Le Borgne *et al.* (2007) were imaged and geometrically characterized. To identify which of the imaged fractures that are connected to the transmissive fracture network, Dorn *et al.* (2011) and Dorn *et al.* (2012b) performed GPR monitoring during saline tracer experiments. Three different transmissive fractures were chosen for the tracer injections (B1 at $z = 78.7$ and 50.9 m and B2 at $z = 55.6$ m) while pumping in the adjacent monitoring borehole. A total of 30 fractures were identified as being connected to at least one of the tracer injection locations. We used the static GPR data from Dorn *et al.* (2012a) to constrain the geometry of these fractures (Figure 5.3). They have a dip range of 30-80°, with the lower limit being imposed by the detection limit of the GPR system. Yet it is likely that the granite formation has very few subhorizontally dipping fractures (dips below 30°), because the borehole logs that are the most sensitive to subhorizontal fractures only indicate one transmissive fracture with a dip below 30° (in B1 at $z = 78.7$ m dipping 15°). During the course of the GPR-monitored tracer tests, the borehole

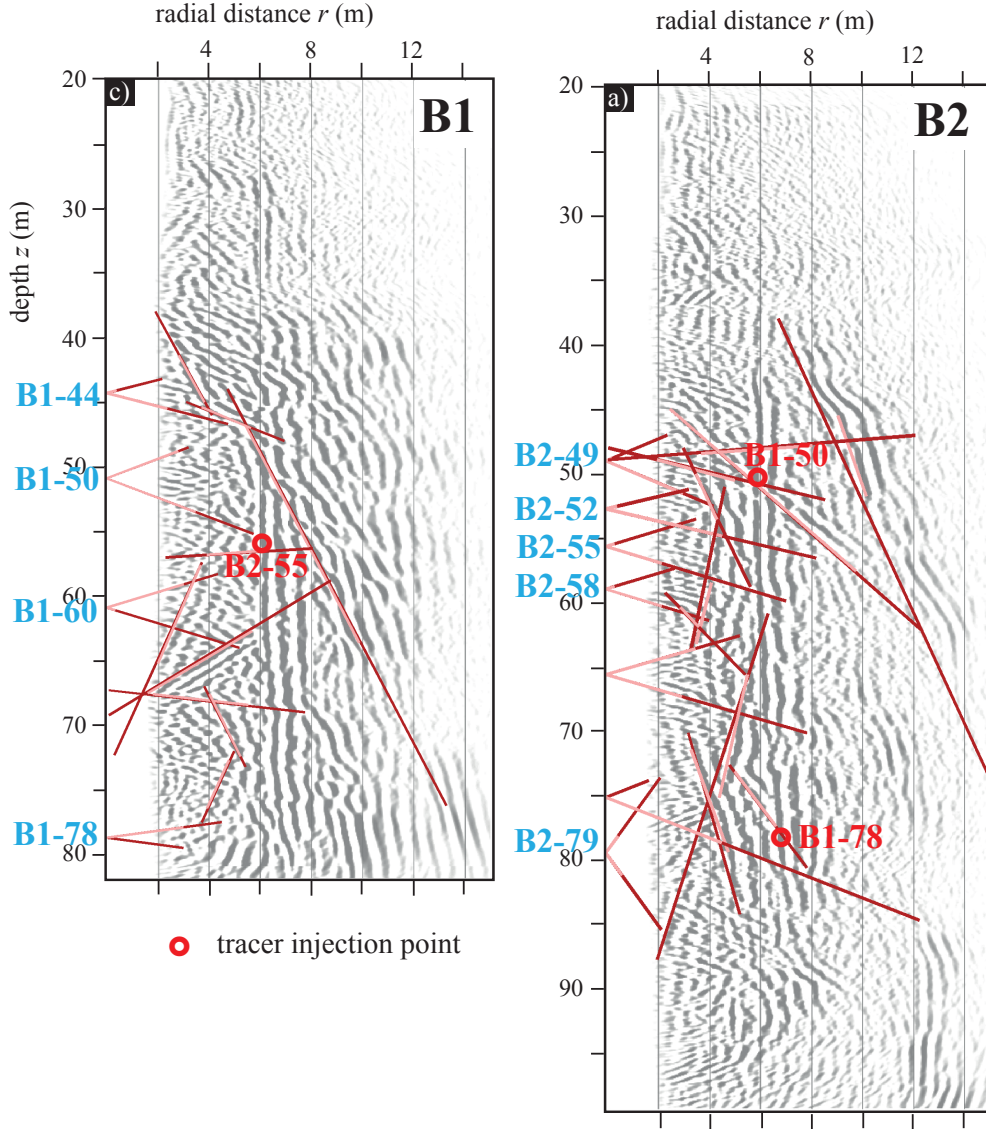


Figure 5.3: Extracts of the migrated multi-offset single-hole GPR sections of B1 and B2 from Dorn *et al.* (2012a) with superimposed interpretations of 30 fractures that were either inferred to be part of the connected fracture network using tracer tests and geophysical monitoring (Dorn *et al.*, 2011, 2012b) or to be hydraulically important based on Le Borgne *et al.* (2007). Light red colors depict the minimal extent of fracture chords, whereas dark red colors depict the maximal extent. Blue letters refer to hydraulically important fractures that intersect boreholes. Red circles refer to the location of the injection fractures used in the tracer tests by Dorn *et al.* (2012b). The axis aspect ratio $r : z$ is 2 : 1.

fluid electrical conductivity σ_w and hydraulic pressure p were monitored in the monitoring borehole. The electrical conductivity profiles were used to calculate concentration profiles and, together with previously acquired flowmeter data (Le Borgne *et al.*, 2007), to identify outflow locations and estimate massflux curves and mass recoveries at each such location (Table 5.1). In Table 5.1, l_{direct} denotes the direct distant between cross-hole connections. The pressure

conditions were rather unstable during these experiments, which implies that the pressure variations significantly influence the shape of the massflux curves (see Figure 11 in Dorn *et al.*, 2012b). The total mass recoveries were also relatively low in all experiments ($\sim 15\%$), which is likely due to the important natural flow gradient (natural vertical flow is 1.5 L/min and imposed pumping rates were in the order of 5-15 L/min). As conditioning data, the relative ratios of total mass recoveries at the different outflow locations are rather well constrained. This is because variations in the hydraulic head gradient are expected to similarly influence the mass recoveries at the different outflow locations. The connectivities between the outflow locations and the injection location mainly define the relative ratios of mass recoveries, while the ambient flow is considered to have no significant influence on these ratios.

Table 5.1: Information on specific cross-hole hydraulic connections observed during three different tracer tests between boreholes B1 and B2 based on Dorn *et al.* (2012b). The name of a fracture (e.g., B2-55) indicates in which borehole (here, B2) and at which depth range (here, $55.0 \text{ m} \leq z < 56.0 \text{ m}$) a fracture intersects the borehole.

Experiment	Fracture	Fracture	l_{direct} (m)	Hydraulic Connection	Relative Massrecovery
I	B1-78	B2-55	23.3	Yes	0.14
	B1-78	B2-58	20.1	Yes	0.30
	B1-78	B2-79	6.7	Yes	0.56
II	B1-50	B2-49	5.1	Yes	0.20
	B1-50	B2-52	5.3	Yes	0.53
	B1-50	B2-55	7.1	Yes	0.25
	B1-50	B2-79	9.8	Yes	0.02
III	B2-55	B1-78	23.3	Yes	0.65
	B2-55	B1-50	7.1	Yes	0.03
	B2-55	B1-60	7.0	Yes	0.32
	B2-55	B1-44	12.7	No	-

Prior distribution

The data used to define the prior distribution $p(\mathbf{m})$ of the connected DFN are listed in the following.

(1) Nine hydraulically important fractures were identified both in the borehole logs and in the GPR data, with three of them being used as tracer injection locations (Table 5.1). Another 21 fractures were solely identified from GPR time-lapse data as they do not intersect the boreholes. These 30 fractures are included in each proposed connected DFN. Note that this number constitutes a minimum number of the actual fracture network, as we do not consider fractures outside of the detectable GPR-ranges.

(2) We impose that all 21 fractures that were identified solely from the time-lapse GPR data have to be connected to the corresponding fracture in which the tracer injection took place. They do not have to be part of the backbone of the hydraulic connections established

for the experiment in which they were identified as the natural gradient may have pushed tracer into fractures that are not part of the backbone. Nearly all fractures have to be connected by definition, because some fractures play a role in several experiments (e.g., B2-55 plays a role in all three tracer tests; see Table 5.1). The only fracture that is unconnected to the other fractures is B1-44 in the case study. This fracture was identified by Le Borgne *et al.* (2007), but not in the time-lapse GPR images of Dorn *et al.* (2012b). The reason to include this fracture is that its spatial extension restricts the geometries of nearby fractures that must be unconnected to this fracture.

(3) Optical televiewer logs constrain dip, azimuth and intersection depth of fractures that intersect boreholes. We account for an uncertainty of 5° and 3° in azimuths and dip angles.

(4) Fractures identified by time-lapse GPR data (Dorn *et al.*, 2011, 2012b) are geometrically characterized by the static GPR data (Dorn *et al.*, 2012a). We account for the following uncertainties:

- picking error of reflectors in the migrated GPR sections is considered to be a quarter of a wavelength (with a central frequency of 140 MHz and a GPR velocity of 0.12 m/ns, the wavelength is $\lambda = 0.86$ m and the reading error is thus ~ 0.2 m),
- uncertainty of GPR velocity used in the migration ($\Delta v = \pm 0.002$ m/ns for the mean velocity of 0.12 m/ns based on tomographic inversion (Dorn *et al.*, 2012a), which implies a relative error of $\Delta r/r = 2 \times \Delta v/v = 4\%$ for the radial distances r as the waves travel from the source to the reflector and then back to the receiver,
- uncertainty of depth positioning of the final stacked GPR section was estimated to be $\Delta z = \pm 0.07$ m (Dorn *et al.*, 2012a),
- uncertainty due to the size of the Fresnel zone (depending on the radial distance r of a feature, we add an uncertainty Δz of half of the Fresnel zone that is given by $1/2 \sin(\varphi) \sqrt{1/2 \lambda r}$, where φ is the dip of the reflector.
- uncertainty of the offset between the actual fracture diameter and the imaged chord b , that is chosen to vary between 0 and $0.75 \times R$ (see Figure 5.1).

(5) Azimuths of fractures are only considered to be between 90 - 120° and 150 - 330° , as all identified fractures in the televiewer data have azimuths in these ranges (Belghoul, 2007).

(6) Borehole deviation data define the relative distances between boreholes B1 and B2, and thus allows defining all fracture geometries in one common coordinate system.

(7) No fracture is allowed to intersect both boreholes. The 21 fractures identified in the time-lapse GPR data can only intersect an adjacent borehole if there is an open fracture observed at a similar depth of intersection (± 0.15 m), similar dip ($\pm 20^\circ$) and azimuth ($\pm 20^\circ$) as in the optical borehole logs.

(8) We exclude fracture models that do not fit the meshing constraints in our flow model, meaning that the length of a fracture intersection, the distance between different intersections

and between an intersection to a borehole-fracture intersection, and the distance between two non-intersecting fractures must be larger than the minimum meshing size (0.15 m).

This section highlights that there is a very significant amount of detailed site-specific information that is included in the prior.

Conditioning data

The hierarchical direct sampling scheme is applied to three different conditioning levels that are described in the following. These data sources represent information that is difficult to incorporate in the prior distribution.

(1) Conditioning level 1: For each proposed model, we determine the cross-hole hydraulic connections (Yes-or-No connections) and compare them with those inferred from flowmeter and tracer tests (Le Borgne *et al.*, 2007; Dorn *et al.*, 2011, 2012b). The eleven connection constraints are listed in Table 5.1. Only models for which all the connections are correctly predicted are retained.

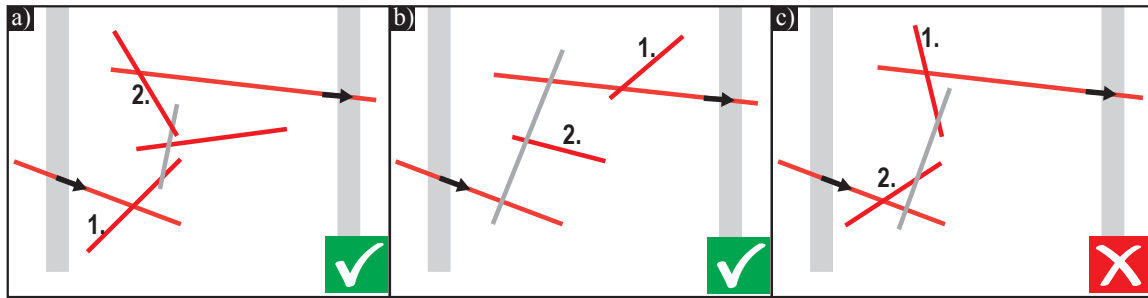


Figure 5.4: Simplified 2-D schematic describing (a-b) acceptance and (c) rejection of simulated fracture models at conditioning level 2. Red colored fractures are identified in the time-lapse GPR data to be connected to the shown injection location. Grey colored fractures are identified in other tracer tests. Both types of fractures can be part of a hydraulic connection between injection and outflow points in the observation borehole. A fracture model is only accepted if the connection order of fractures (indicated by the numbers in the figure) in the backbone agrees with the interpretation based on the GPR time-lapse images.

(2) Conditioning level 2: We compare for all tracer experiments and connections (Table 5.1) the sequential order of connecting fractures in the backbone of a simulated hydraulic connection between injection and outflow points (e.g., fracture A is followed by fracture B) with the order interpreted from time-lapse GPR images. A sequential order have been imposed for 13 fracture pairs. We were conservative in only imposing such constraints for connections that are very well-resolved in the time-lapse data. The calculation of the order of fracture connections that establishes a connection between the boreholes uses a depth-first search algorithm (Tarjan, 1972) that is based on a graph representation of the fracture network. Figure 5.4 depicts some scenarios of acceptance and rejection depending on the fracture network topology. For an established hydraulic connection, the backbone of the connection has to fully fulfill the sequential order of connecting fractures, dead-end fractures are excluded from the comparison.

The backbone of a hydraulic connection can consist of fractures that have been identified either during the corresponding tracer experiment (red colored fractures in Figure 5.4) or in another tracer test that uses a different injection location (grey colored fractures in Figure 5.4).

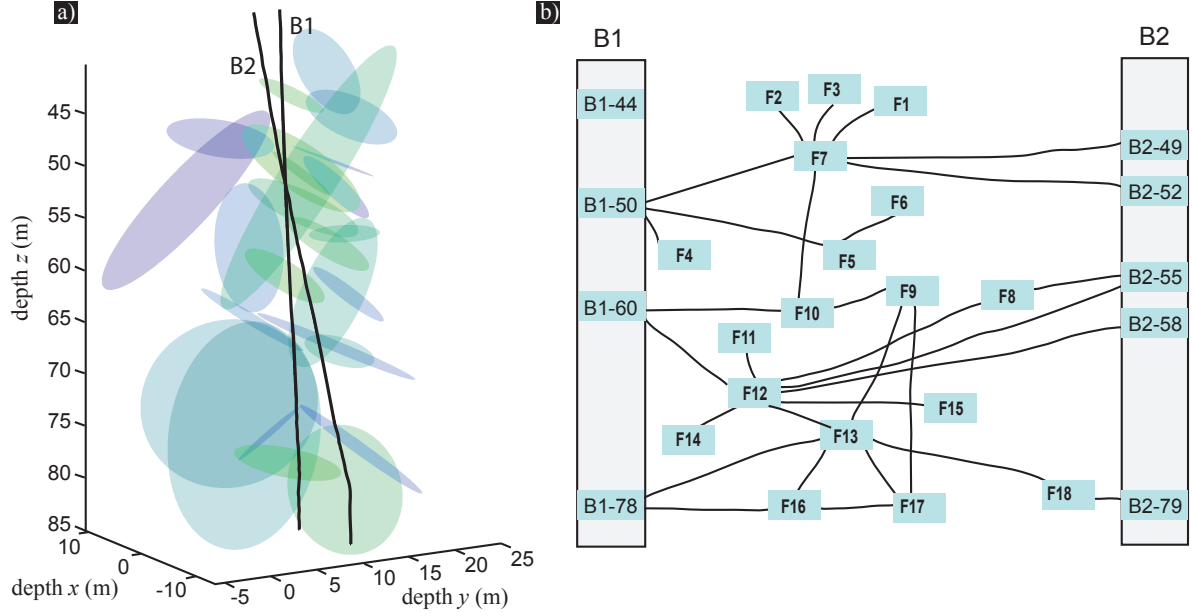


Figure 5.5: One realization of a fully conditioned fracture model (a) in 3-D Cartesian coordinates and (b) in graph representation.

(3) Conditioning level 3: We simulate flow through the proposed connected DFN to test if the simulated relative flows at the tracer arrival locations are matching the measured relative mass that arrives at those output fractures. We have chosen to compare relative flow with relative mass recovery ratios, in order to not introduce transmissivity as an additional parameter. The observed relative mass recovery ratios and the simulated flow ratios depend explicitly on the connectivity to the injection location and on the topology of the fracture network. The flow is simulated on the connected structure of the proposed networks using H2OLAB (Poirriez, 2011; Erhel *et al.*, 2009). In the flow modeling, the rock matrix is impervious. We consider homogenous and constant fracture permeabilities. The relative flow values will thus only be influenced by the topology of the fractures. Within the fracture planes it is assumed that Darcy's law and mass conservation is satisfied. No longitudinal flux is allowed on the fracture intersections and continuity of the hydraulic head and the transversal flux are imposed. For the injection and outflow locations at the fracture-borehole intersections, we impose Dirichlet boundary conditions to impose head gradients and use Neumann zero flux conditions on fracture edges. The model is solved with a mixed hybrid finite element method that allows using locally refined meshes at fracture intersections. Within a fracture, the mesh is 2-D and is conform within each intersection. The number of elements varies between 5×10^5 and 1×10^6 , depending on the model realization.

The imposed head gradient is estimated from the observed drawdown during the tracer experiments. Fracture networks are accepted for which the discrepancy of relative simulated flux rates and relative observed mass recoveries are smaller than 35%. This threshold was set according to the estimated error of the observed mass recovery ratios, that is mainly influenced by the relative error of flow ($\sim 15\%$ error) and the relative error of the measured concentration curves ($\sim 20\%$ error).

The accuracy of the conductivity logger (CTD diver 44077) is listed as 1%, but the conductivity values are likely smeared out because the borehole fluid was additionally mixed due to the up and down movement of the GPR antennas. The estimation of the associated error is difficult. We have estimated the error of 20% by calculating the gradient of the concentration around the tracer arrival locations using different depth interval lengths around the outflow location. The positioning error is negligible in comparison.

5.5 Results

We use the hierarchical direct sampling scheme to evaluate 2 million models drawn from the prior distribution. To generate a single realization of a 3-D fracture model requires, on average, 0.2 sec of CPU time. A fully conditioned fracture model that is tested for all the imposed data constraints require, on average, 4 min as the flow modeling for all three considered tracer tests is rather costly. Out of the tested 2 million prior models, 10% honor the binary hydraulic connection information (conditioning level 1) out of which only 0.4% honor the GPR-constrained sequential order of the fractures (conditioning level 2). Out of the remaining models, 24% agree with the observed relative mass recoveries (conditioning level 3). Overall, $\sim 0.01\%$ of all proposed prior models honor all imposed data constraints. Figure 5.5 shows two representations of the same realization of a fully conditioned fracture model, Figure 5.5a is a spatial representation in Cartesian coordinates, whereas the graph representation in Figure 5.5b indicates the connectivity of the fractures. Clearly, it is difficult to derive fracture network characteristics from such representations, but they help to validate the correct implementation of the scheme.

To evaluate the statistical properties of the prior and conditional models, we rely on the following geometrical characteristics of the fracture networks: mean \bar{R} and variance of fracture radii, mean fracture intersection length, characteristic length l_c and the mean number of intersections per connected fracture \bar{n}_{inter} . The mean and variance of fracture radii are key parameters in describing the connectivity of a fracture network (Bour and Davy, 1998). The mean intersection length quantifies if fracture intersections are well connected or not. Furthermore, the average number of intersections per fracture may be used to quantify the connectivity of a fracture network (Berkowitz, 1995; Robinson, 1983), while the characteristic length is a convenient measure of the average block size between fractures. In the following, we discuss the different measures in detail. Note that they are clearly expected to be correlated with each other.

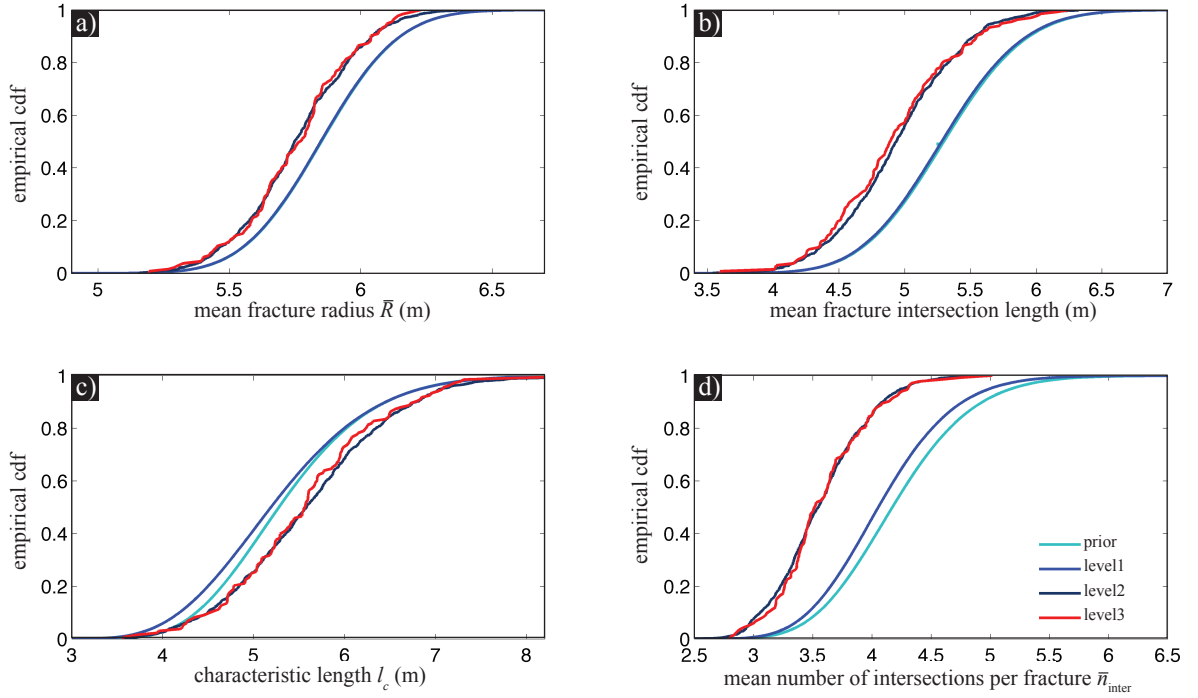


Figure 5.6: Empirical cumulative distribution of (a) the mean fracture radius \bar{R} , (b) the mean fracture intersection length, (c) the characteristic length l_c and (d) the mean number of intersections per connected fracture \bar{n}_{inter} . These distributions are derived from model realizations with different levels of conditioning. The prior distribution is based on 2×10^6 models, level 1 on 2×10^5 models, level 2 on 8×10^2 models and level 3 on 2×10^2 models.

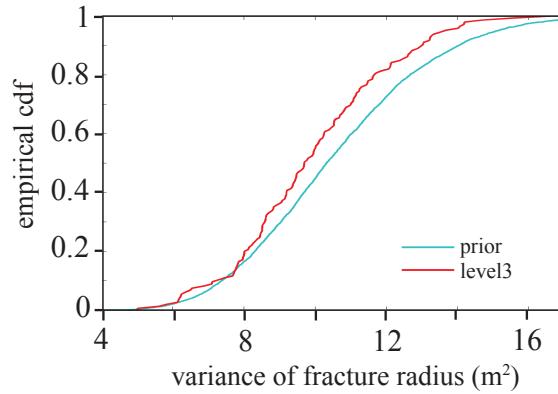


Figure 5.7: Empirical cumulative distribution of the variance of fracture radius for the prior distribution and level 3 based on 2×10^6 and 2×10^2 models, respectively.

Mean and variance of fracture radii

Figure 5.6a shows the cumulative distribution function (cdf) of the mean fracture radius for model realizations at different conditioning levels. The distribution of this parameter is well constrained in the prior ($5.2 \text{ m} < \bar{R} < 6.6 \text{ m}$) by the GPR-constrained geometrical bounds on the fracture geometries. Without the GPR data, the only applicable constraint from the borehole logs on the extent of fractures is the fact that there is no fracture intersecting both

adjacent boreholes (that are 6 m apart). Mean fracture radius \bar{R} (Figure 5.6a) of the prior set of models are on average higher than the mean fracture radius of the final conditioned DFNs. The difference between the 50th-percentile of prior and level 3 cdfs is about 38% of the prior's standard deviation.

Figure 5.7 shows the cdf of the variance of the fracture radii for the unconditioned and conditioned DFNs, with the final conditioned models indicating a slightly lower variance. The upper prior bounds on the fracture radii are rather uncertain (see parameter b). Mainly topological constraints from the time-lapse GPR data used in conditioning level 2 may reduce this uncertainty. The difference between the 50th-percentile of prior and level 3 cdfs is about 24% of the prior's standard deviation. Too large fracture radii result in more intersections with neighboring fractures and hence more fractures are included in the backbone structure, which makes it more likely that the resulting sequential order of fractures in the backbone contradicts the GPR constraints (conditioning level 2).

Mean fracture intersection length

The mean fracture intersection length (Figure 5.6b) is the length on a fracture plane that is shared with another fracture. As for the mean fracture radius, the distribution of the mean fracture intersection length indicates lower values in the level 3 distribution than in the prior distribution, but the differences are more pronounced. Here, the difference between the 50th-percentile of prior and level 3 cdfs is 84% of the prior's standard deviation. This is due to the fact that the probability of a fracture intersection is related to the area of a fracture plane rather than to the fracture radius. This implies that the variations in mean fracture intersection lengths are related to the square of the variations in mean fracture radius. Again the cdf of the intersection length are well constrained by the GPR-constrained bounds on the prior geometries of fractures. The reason for the typically smaller mean fracture intersection length in the fully conditioned DFNs is the same as described above.

Characteristic length

We define a characteristic length l_c as a measure of the mean blocksize between fractures (Figure 5.6c). For an idealized equi-distant lattice the characteristic length is a measure of the distance between two adjacent vertices. The characteristic length in Figure 5.6c is estimated by dividing the minimal cubic volume V that is spanned by a cluster j of i fractures by the sum of the fracture surfaces L of this cluster and averaged over the number of clusters J :

$$l_c = \frac{1}{J} \sum_j \frac{V_j}{\sum_i L_{i,j}}. \quad (5.2)$$

The characteristic lengths of the fully conditioned models tend to have higher values than the prior proposed models. The difference of the 50th-percentile between prior and level 3 distributions is about 33% of the prior's standard deviation. The smaller the l_c , the higher is the number of fracture intersections that exist between two points and the higher is the probability

of having multiple flowpaths between them. Compared to the prior models, we observe for the final conditioned models a tendency towards higher l_c and smaller mean fracture radii. It thus seems that an increase in the mean fracture radius increases the total surface in a fracture network more than it increases the volume that is spanned by the fracture network, because (1) the number of fractures involved in a proposed DFN is nearly constant by definition and (2) the positions of fractures are well bounded by the geometrical GPR constraints, which implies that the change of spanned volume is small. If GPR data would not be available, an approximation of the characteristic length (Figure 5.6c) could be obtained by dividing the borehole interval l by the number of observed fracture intersections along l . Because the borehole logs are preferentially cutting through subhorizontal fractures, an angular correction to the fracture dip φ is necessary by dividing by the cosine of the fracture dip (assuming perfectly vertical boreholes) (Terzaghi, 1965). The characteristic length can thus be approximated by:

$$l_c \approx \frac{l}{\sum_i 1/\cos(\varphi_i)} \quad (5.3)$$

For the granite formation ($z = 38\text{-}83$ m in B1 and $z = 43\text{-}100$ m in B2) and only considering the hydraulic important fractures (4 in B1 and 7 in B2), we estimate $l_c \approx 10$ m in B1 and $l_c \approx 5.5$ m in B2. Clearly, those approximations are very rough because they are based on a limited amount of data and assume uniform distribution of fracture dips. The prior and level 3 models yield much better constraints on the characteristic length, even if the borehole-based approximations lie within the same order (Figure 5.6c).

As mentioned, the characteristic length expresses how many fractures are on average involved in establishing a connection over a certain path length. Hence, we can calculate how many fractures n_{\min} would be needed to establish a hydraulic connection with a minimal path length of l_{\min} . The slope of $q = \Delta l_{\min} / \Delta n_{\min}$ should be $q \sim l_c$. Figure 5.8 shows l_{\min} over n_{\min} for final conditioned models. The slope $q = 4.7$ is consistent with estimations of l_c . To establish a hydraulic connection at the field site over 10 m distance, there are at least 5 fractures involved.

Number of intersections per connected fracture

Similar to the mean fracture intersection radius \bar{R} , the number of intersections per fracture \bar{n}_{inter} (Figure 5.6d) is related to the mean fracture area. We define this parameter by:

$$\bar{n}_{inter} = \bar{R}^2 \sum_i n_{inter,i} / R_i^2 \quad (5.4)$$

This measure shows clearly the impact of the conditioning with a difference between the 50th-percentile of prior and level 3 cdfs of 120% of the prior's standard deviation. The largest difference between the conditioning levels can be seen between the models of conditioning level 1 and 2, where the sequential order of fractures in the backbone structure is conditioned to the

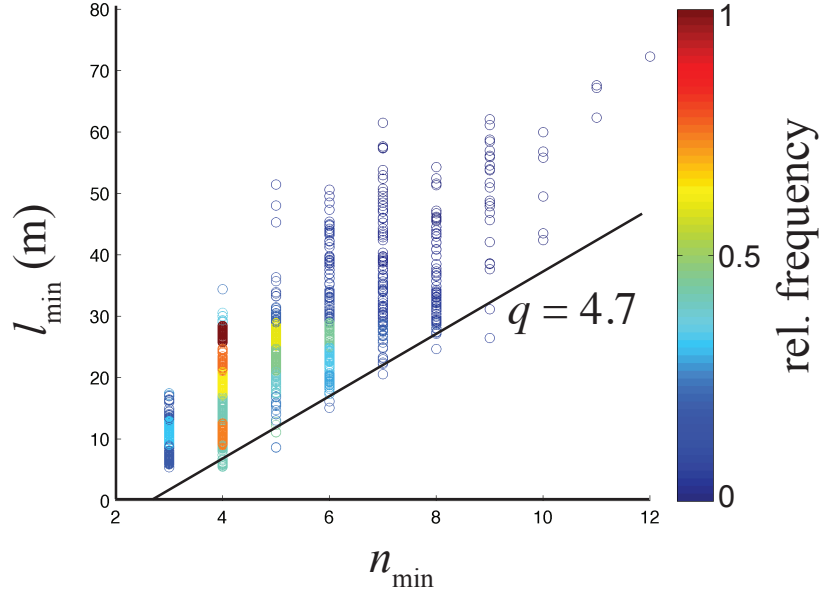


Figure 5.8: The relative number of occurrences of cross-hole connections for final conditioned models whose minimum pathlength l_{\min} of the connection requires n_{\min} numbers of fractures. The slope q is similar to the characteristic length l_c . The relative frequency represents the relative occurrence of a hydraulic connection.

GPR data. The constraints of GPR data on the topology of the DFNs condition the models to smaller \bar{n}_{inter} , which is related to the smaller fracture radii.

Flow contribution

Figure 5.9 shows the empirical cdf of flow for the three considered tracer experiments (Table 5.1). The x -axis in the plot is normalized such that the sum of the prior cdfs of all three experiments for the 50th-percentile sum up to one for an imposed head gradient of 1 m. In general, the differences between prior and level 3 conditioned models are mostly visible for short hydraulic connections. Figure 5.9c of experiment III with the longest hydraulic connections (Table 5.1) show the least differences between prior and level 3 distributions. This is mostly because there are not many variations of fracture connections possible to obtain the longest hydraulic connections, as the prior models rely on GPR interpretations that are spatially restricted. Furthermore, due to the shorter hydraulic connections of experiment II (Figure 5.9b), its flow contribution is more important than the contribution of experiments I and III.

5.6 Discussion

The proposed hierarchical direct sampling scheme yields samples from the prior and posterior distributions of connected DFNs at different level of conditioning. The rather low acceptance rates at each level of conditioning indicate that new information is added by the considered

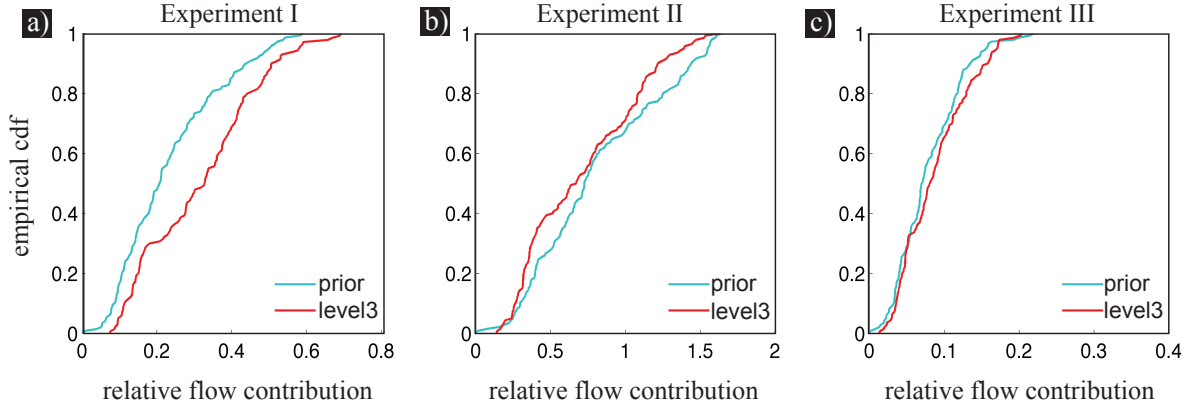


Figure 5.9: Empirical cumulative distribution of the relative flow contributions for the tracer experiment (a) I, (b) II and (c) III from model realizations of the prior (light blue) and level 3 (red) distributions based on 200 models.

data constraints. To quantify the added information, we have analyzed the different distributions of models by analyzing the empirical cdfs of average geometrical measures and flow contribution. It is important to note that the geometrical characteristics of the DFNs are already strongly constrained by the imposed geometrical constraints used to establish the prior models. Furthermore, the restriction of the prior models in terms of the number of fractures and the geometrical bounds on each fracture makes our proposed scheme computationally feasible despite the large number of model parameters.

Figure 5.6 shows that final conditioned models are centered towards smaller mean and variance of fracture radii than realizations from the prior, which is similarly expressed by the other geometrical measures. The uncertainty of the upper bounds on fracture radii caused by the underdetermined parameter b , is reduced by the conditioning data. The hydraulic connection data (conditioning level 1) has little effect on the distributions. This is mainly because (1) the GPR-identified fractures of the proposed prior models are already connected (by definition) to the corresponding injection fractures and (2) there is only one fracture for which a hydraulic connection was not observed in the field (B1-44 in Table 5.1). The acceptance rate of 10% at the conditioning level 1 is thus mainly related to the probability of fracture B1-44 to be disconnected to the DFN. The GPR-constrained sequential order of fractures (conditioning level 2) have the strongest effect on the fracture topology. The prior distribution has a significant uncertainty in fracture radius which leads to realizations with very different fracture connections and thus to very different sequential orders within the backbone structure. The GPR data constrain this sequential order of fractures in the backbone structure. Conditioning level 3 has little effect on the conditioning of the topology of the DFNs, which is mainly due to (1) the large uncertainty range of the relative mass recoveries and (2) that we compare mass recoveries and flux rates only in a relative sense.

By analyzing the flow distributions resulting from the prior and posterior distributions. We find smaller variability between the prior and posterior flux rates for long compared to

short hydraulic connections. The long hydraulic connections are roughly at the same order as the system size of realized DFNs. This is also expressed by Figure 5.10 in which we have calculated the tortuosity τ by $l_{\min}/l_{\text{direct}}$ for all ten possible hydraulic connections between injection and tracer arrival points that are considered in the final conditioned DFNs. The tortuosity of long hydraulic connections ($l_{\text{direct}} > 20$ m) vary very little between realizations as we consider a finite number of possible fractures in a finite volume. In contrast, there are realizations for which short hydraulic connections are established by very different pathways, the tortuosity may be up to ten for $l_{\text{direct}} \approx 5$ m. Models with such large tortuosities are probably rather unrealistic and would likely be rejected if we would include the conditioning to tracer breakthrough data.

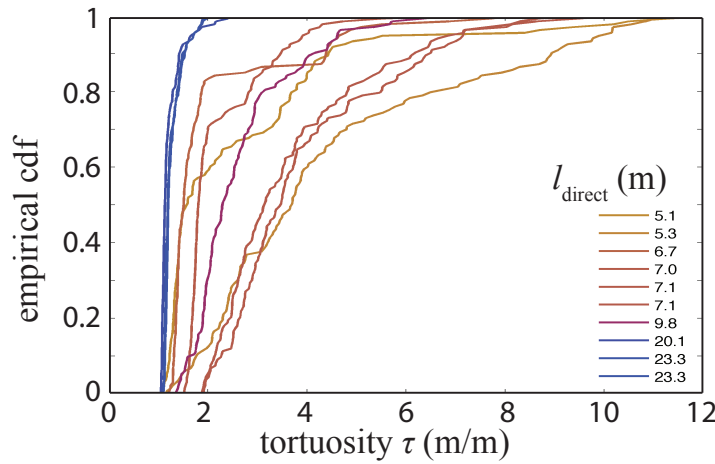


Figure 5.10: Empirical cumulative distribution of tortuosity of individual hydraulic connections between the injection and outflow point (indicated with different colors) calculated for the final conditioned fracture models. Tortuosity is calculated as the minimal distance of a hydraulic connection in a specific model realization divided by the direct distance between the inflow and outflow locations of the inter-borehole connection.

There are some further simplifications in the proposed study that could be relaxed in the future. First, the distribution of possible DFNs may be biased by assumptions as (1) fractures outside GPR detectable ranges are not taken into account (regarding dip, length, strike and radial distance), (2) the identification of fractures with GPR-imaged chord lengths smaller than ~ 3 m is very difficult due to signal superposition in the GPR images, even if the fractures are detectable, (3) we do not account for the fact that a fracture is identified in GPR images of different boreholes and (4) we only partly stimulate the local connected fracture network during the three considered tracer test and hence we consider only those fractures that are connected to the three considered tracer injection locations. Considering these limitations, it is likely that the mean fracture length and the mean intersection length are overestimated, that the density of fractures is underestimated, which also implies that the characteristic length could be overestimated. Second, for the purpose of building predictive transport models, a higher complexity of the fracture models is probably required. Some of the imposed assumptions

should be dropped in the future and further possible extensions of the proposed scheme are possible:

1. It is necessary to account for fractures that have been identified twice in different GPR images from neighboring boreholes. The location of such fractures can be further restricted in the prior bounds and the definition of two fractures when there is actually only one should be avoided.
2. Open fractures that are identified in the televiewer data but which do not play a role in any hydraulic connections could be taken into account when generating the connected fracture models. Their presence restricts the geometry of the adjacent fractures that are identified to be part of the cross-hole hydraulic connections and hence are not connected to these open fractures. By including these open fractures, models in which a hydraulic connection between the boreholes is realized that is not observed in the field, can be rejected.
3. Transport modeling of the performed tracer tests would allow obtaining estimates of the hydraulic transmissivities of the network. Individual transmissivity values could be assigned to every fracture. This extension could also require the implementation of transient flow modeling, depending on the observed data.
4. Timing information from the time-lapse GPR data could be considered (e.g., if in a specific tracer test we have identified a certain fracture after time t_{obs} in the time-lapse images, then the tracer must have reached this fracture at a time $t < t_{\text{obs}}$).
5. Stereological analysis of hydraulic important fractures based on televiewer data and GPR images could be used to derive a fracture length distribution. The generation of connected fracture models could then be conditioned to this distribution and its uncertainty ranges, namely by correlating the fracture radii and by allowing additional fractures to be generated (with geometries that lie outside the GPR detection ranges).

It is clear that some of the listed possible extensions would involve increased computation times as they require either more advanced forward modeling (e.g., transport modeling) or higher model dimensions (e.g., including individual fracture transmissivities). To constrain parameters in higher dimensions, data are needed that are sensitive to those parameters. The implementation of more complex models is thus a question of computational power, available data and data quality. All simulations presented herein were performed on one computer processor. Speed-ups based on direct sampling scales linearly with the number of processors, which means that higher dimensions and transport modeling would be computationally feasible when using, say, 100 processors in parallel, which is common practice nowadays.

5.7 Conclusions

The properties of hydraulic cross-hole connections strongly depend on the 3-D geometry and topology of the local network of connected fractures. This network can be studied by inves-

tigating the cross-hole connections through hydrological and GPR reflection data. We use different data types (hydraulic, televiewer and GPR reflection data) to define prior bounds and to condition connected 3-D fracture models that agree with all available data. A hierarchical direct sampling Monte Carlo method is used to generate large sets of such realizations. The bounds of the prior distribution (the number of fractures, their positioning, orientation and spatial extent) are largely defined by the televiewer and the GPR data. Their use in defining the prior distribution makes the stochastic scheme computationally feasible as these data strongly reduce the set of possible prior models. In applying the methodology to field data, we find models that can reproduce all of the observed data constraints (e.g., hydraulic connections and their relative degree of connectivity, as well as the sequential order in which tracer moves through fractures in the backbone structure). From these fully conditioned models, we derive length scales and connectivity metrics distributions of the network. For example, the distribution of a characteristic length of the fracture network indicate how many fractures are, on average, forming a hydraulic connection between two injection and extraction points. The posterior realizations exhibit a significant variability in simulated flow even if fracture transmissivities are the same in all fractures. We find that the most important conditioning data are those related to the sequential orders of tracer movement in the fractures as inferred by time-lapse GPR data. Assumptions about the number and geometrical bounds of fractures might bias the derived statistics and they will partly be relaxed in the future. This approach can be applied to other fractured rock sites where the electric conductivity of the host rock is low, such that GPR methods can be applied. We conclude that the stochastic generation of conditioned fracture models is a powerful approach to study 3-D heterogeneity of the local connected fractures.

Chapter 6

Conclusions and Outlook

The predictive capabilities of quantitative flow and transport models of fractured rock aquifers at the field scale are generally limited by the limited knowledge of the geometry of individual fractures and their connectivity. In fact, flow is often organized in preferential flow paths that are largely determined by the spatial organization of the fractures. Classical hydrological data can be used to investigate specific hydraulic connections that are accessible through boreholes. Such data provide averaged hydraulic estimates of these hydraulic connections, which might comprise several fractures with complex connectivity patterns. Recent studies have shown that individual fractures can be identified and geometrically characterized using GPR reflection data. The use of either hydrological or GPR reflection data alone is generally insufficient to parametrize reliable quantitative fracture network models at the field scale.

The general aim of this thesis was to improve fractured rock characterization by combining GPR reflection data with classical hydrological data. The three primary objectives outlined in the introduction has been largely met:

1. I have improved the imaging of tracer movements in a complex system of fractures using GPR reflection data and made it possible to locate corresponding tracer flow paths.
2. I have inferred fracture network characteristics from a combined interpretation of hydrological and GPR reflection data.
3. I have generated 3-D fracture models that are consistent with available hydrological and GPR reflection data.

6.1 Conclusions

To investigate the ability of borehole GPR reflection data to image individual fractures in complex fractured environments, I first used multiple-offset single-hole and cross-hole GPR reflection data under natural flow conditions (static GPR data) as presented in Chapter 2. A tailored processing scheme was tested in three adjacent boreholes at the Stang-er-Brune site in France. The multiple-offset acquisitions with 100 and 250 MHz GPR antennas allow detecting

mm-aperture fractures of limited spatial extent in the granite formation. I successfully imaged those parts of fractures for which normal vectors exist that cut the observation boreholes, given that their dips are in the range of $30\text{-}90^\circ$, that they lie within radial distances of 2-20 m from the boreholes and that their spatial extents are larger than the first Fresnel zone. To identify which of the imaged individual fractures that are transmissive and part of the local hydraulic connections, I analyzed single-offset single-hole GPR reflection data acquired repeatedly during saline tracer tests (time-lapse GPR data), as presented in Chapter 3. Key aspects for successful time-lapse GPR data analysis is signal repeatability. A rather elaborate processing scheme was therefore developed to account for variable fluid conductivities in the observation borehole, variable transmitter power, variable coupling of the antennas to the host rock and inaccuracies in the positioning of the GPR antenna system.

Compared to classical hydrological data, the time-lapse GPR data provide additional and complementary information about the temporal evolution of the spatial distribution of tracer solution. In a series of three different tracer experiments (using three different fractures as injection locations, while pumping in the adjacent borehole) I showed, in Chapters 3 and 4, that hydraulic connections between the two ~ 6 m apart boreholes comprise several fractures. Despite the short distance between the boreholes, the tracer may spread over tens of meters, depending on the fracture connectivity and the influence of the imposed and natural head gradients. About 20% of the fractures that were previously identified by the static GPR data (Chapter 2) are part of the inferred local flow paths. The length scales of fractures involved in the tracer transport can be derived from the static GPR data and their connectivity can sometimes be inferred from their temporal appearance in the time-lapse GPR data. Information about the fracture length and connectivity helps to constrain simplified fracture models, as presented in Chapter 4, and thus enhances the analysis of breakthrough data. Furthermore, the GPR images help to understand where tracer mass went that could not be recovered. The relatively low mass recovery in all experiments ($<30\%$) is attributed to the vertical ambient head gradient at the site. The usefulness of GPR data to estimate relative changes in tracer concentrations at specific fracture locations away from the boreholes was confirmed by smoothly varying GPR reflection amplitudes that were in agreement with tracer concentration changes derived from simplified fracture models. The time-series of GPR reflectivity changes indicate not only the arrival time of the saline tracer at a specific fracture location, but also how the tracer concentration increases and decreases over time.

The fracture model used in Chapter 4 to describe one specific tracer experiment was based on very strong simplifications. To mitigate them, I presented in Chapter 5 a new approach to stochastically generate 3-D models of connected fractures that are conditioned to all available hydraulic, televiewer and GPR imaging data. I appropriately accounted for (1) the 3-D nature of fracture models, (2) the finite size of fractures, and (3) the uncertainties of the different types of conditioning data. The main assumptions of the proposed scheme are that fractures are parametrized as thin circular discs and that the appropriate number of fractures involved in a model is identified by the time-lapse GPR data. I used a hierarchical direct sampling Monte

Carlo method to generate fully conditioned models of connected fractures. The appropriate definition of the bounds of the prior distribution are important to make the stochastic approach feasible and the results meaningful. Out of 2 million proposed prior models within the GPR-defined bounds, I found 200 models that can reproduce all of the considered data constraints (e.g., hydraulic connections and their relative contribution to flow, and the sequential order of fracture connections in the backbone structure). Based on these fully conditioned models, the length scales of hydraulically important fractures and the characteristic length of the connected fracture network were investigated amongst other geometrical measures. Those geometrical characteristics are important to understand the spatial organization of the local network of connected fractures that govern local flow processes.

In this thesis, I have successfully shown how GPR reflection data can be used in combination with classical hydrological data to improve the geometrical and hydraulic characterization of fractured rock. I have also demonstrated how the full range of available data from the Stanger-Brune site can help to build quantitative fracture models.

6.2 Outlook

In the following, I give an overview of some topics for future research that I judge important to further advance towards the ambitious goal of building predictive fracture network models. They include both experimental and methodological aspects.

- Stereological analysis of fractures based on a combination of televiewer data and GPR images could be used to constrain scaling laws describing fracture length distributions. As televiewer data are mostly sensitive to subhorizontal fractures, while GPR borehole data are mostly sensitive to subvertical fractures and fracture length scales, it is clear that the combined use of GPR data and televiewer data could yield improved estimates on the scaling behavior of the fracture distributions. Furthermore, as time-lapse GPR data provide a tool to identify the connected permeable fractures, their geometrical characteristics could be examined separately from the entire network. Theoretical arguments indicate that the statistics of the connected fractures differ from those of the whole network (e.g., in terms of fracture density, fracture length and aperture distributions), and experimentally investigating their relationship could be very interesting.
- The generation of connected fracture models could additionally be conditioned to site-specific scaling laws of fracture distributions (e.g., fracture length). This could be done by correlating the fracture parameters (e.g., lengths) and allowing for additional fractures to be generated (especially for geometries that lie outside the GPR detection ranges). This would lead to an unknown number of fractures in the proposed prior network models.
- The proposed stochastic ensembles of fracture network models very much depends on the definition of the prior bounds that in turn depend on the interpretation of GPR sections. The interpretation of time-lapse and static GPR sections might profit from deconvolution

to increase the spatial resolution of the depth-migrated sections (Schmelzbach *et al.*, 2011). Furthermore, the spatial extent of individual fractures might be easier to interpret using dip-filtered GPR sections that successively put emphasis on different dip ranges.

- Absolute changes in tracer concentrations at specific fracture locations could be estimated by first estimating the fracture aperture by analyzing amplitudes and phases of GPR reflections that correspond to the same fracture location, but acquired with different incident angles. The conversion of such GPR gathers into reflection coefficient properties as a function of offset and frequency is a very delicate operation that can only be performed if the coupling between GPR antennas and investigated rock is almost constant throughout the survey (Deparis and Garambois, 2009). The estimated fracture aperture can then possibly be used to correlate changes in the GPR signal to absolute tracer concentration changes. The dynamic of tracer concentration changes at different locations in the fracture network would then provide additional constraints for the estimation of hydraulic apertures of the individual fractures.

Note that aperture estimates from GPR amplitudes yield spatially averaged estimates. This results in an equivalent hydraulic aperture of a fracture, but hydraulic apertures are likely strongly affected by small-scale variations in geometrical aperture (Renshaw, 1995) that cannot be resolved using GPR reflections.

- The proposed stochastic inversion method could be adapted to also estimate fracture transmissivities of the individual fractures. This requires the use of tracer arrival times or breakthrough data as additional data constraints as well as transport modeling. Particle tracking for 3-D fracture networks within the Hydrolab code is soon to be implemented.
- The use of directional antenna would be most useful to reduce the uncertainty in fracture azimuth. State-of-the-art systems allow resolving azimuths of imaged fractures with an accuracy of about 30° (Slob *et al.*, 2010).
- The repeatability of GPR source signal during monitoring purpose would be improved if using a borehole flexible liner to isolate the monitoring locations from the influence of the conductive tracer. This might also enable the acquisition of hydrological data (pressure and concentrations) that are unaffected by the GPR antenna movement during acquisitions.
- In order to investigate the transport of solutes under natural flow conditions, GPR reflection monitoring could be performed during near natural gradient injection experiments. Spatial spreading of tracer and its temporal evolution will be different compared to forced flow conditions. Adjacent boreholes for which the natural vertical flow might have significant influence on the natural flow regime could be closed with the use of a flexible liner. Furthermore, the use of distilled water as a resistive tracer could be investigated as significant density effects cannot be excluded when using very saline tracers.

Bibliography

- Abelin, H., Neretnieks, I., Tunbrant, S., and Moreno, L. (1985). *Final Report of the Migration in a Single Fracture: Experimental Results and Evaluation*. Nationale Genossenschaft für die Lagerung Radioaktiver Abfälle (NAGRA).
- Aines, R. D., Nitao, J. J., Hanley, W. G., *et al.* (2002). The stochastic engine initiative: Improving predictions of behavior in geological environments we cannot directly observe. Technical report, Lawrence Livermore National Laboratory, Livermore, CA, U.S.A.
- Allaire, G. (1989). Homogenization of the Stokes flow in a connected porous medium. *Asymptotic Analysis*, **2**(3), 203–222.
- Anderssen, R. S. and Seneta, E. (1971). A simple statistical estimation procedure for Monte Carlo inversion in geophysics. *Pure and Applied Geophysics*, **91**(1), 5–13.
- Annan, A. P. (2005). GPR methods for hydrogeological studies. In Y. Rubin and S. S. Hubbard, editors, *Hydrogeophysics*, Water Science and Technology Library, pages 185–213. Springer Netherlands.
- Atkinson, B. K., editor (1987). *Fracture Mechanics of Rocks*. Academic Press Geology Series. Academic Press.
- Balanis, C. A. (1989). *Advanced Engineering Electromagnetics*. Course Smart Series. Wiley New York.
- Barton, N., Bandis, S., and Bakhtar, K. (1985). Strength, deformation and conductivity coupling of rock joints. *International Journal of Rock Mechanics and Mining Sciences & Geomechanics Abstracts*, **22**(3), 121–140.
- Becker, M. W. and Shapiro, A. M. (2000). Tracer transport in fractured crystalline rock: Evidence of nondiffusive breakthrough tailing. *Water Resources Research*, **36**(7), 1677–1686.
- Becker, M. W. and Shapiro, A. M. (2003). Interpreting tracer breakthrough tailing from different forced-gradient tracer experiment configurations in fractured bedrock. *Water Resources Research*, **39**(1), 1024.

- Becker, M. W. and Tsoflias, G. P. (2010). Comparing flux-averaged and resident concentration in a fractured bedrock using ground-penetrating radar data. *Water Resources Research*, **46**, W09518.
- Belghoul, A. (2007). *Caractérisation pétrophysique et hydrodynamique du socle cristallin*. Ph.D. thesis, Université Montpellier II - Sciences et Techniques du Languedoc.
- Berkowitz, B. (1995). Analysis of fracture network connectivity using percolation theory. *Mathematical Geology*, **27**(4), 467–483.
- Berkowitz, B. (2002). Characterizing flow and transport in fractured geological media: A review. *Advances in Water Resources*, **25**(8), 861–884.
- Berkowitz, B., Cortis, A., Dentz, M., and Scher, H. (2006). Modeling non-fickian transport in geological formations as a continuous time random walk. *Reviews of Geophysics*, **44**(2), RG2003.
- Binley, A., Winship, P., West, L. J., Pokar, M., and Middleton, R. (2002). Seasonal variation of moisture content in unsaturated sandstone inferred from borehole radar and resistivity profiles. *Journal of Hydrology*, **267**(3), 160–172.
- Bohlen, T. (2002). Parallel 3-D viscoelastic finite difference seismic modeling. *Computers & Geosciences*, **28**(8), 887–899.
- Bonnet, E., Bour, O., Odling, N. E., Davy, P., Main, I., Cowie, P., and Berkowitz, B. (2001). Scaling of fracture systems in geological media. *Reviews of Geophysics*, **39**(3), 347–384.
- Bour, O. and Davy, P. (1997). Connectivity of random fault networks following a power law fault length distribution. *Water Resources Research*, **33**(7), 1567–1583.
- Bour, O. and Davy, P. (1998). On the connectivity of three-dimensional fault networks. *Water Resources Research*, **34**(10), 2611–2622.
- Bradford, J. H. and Deeds, J. C. (2006). Ground-penetrating radar theory and application of thin-bed offset-dependent reflectivity. *Geophysics*, **71**(3), K47–K57.
- Carruthers, R. M. and Smith, I. F. (1992). The use of ground electrical survey methods for siting water-supply boreholes in shallow crystalline basement terrains. In E. P. Wright and W. G. Burgess, editors, *Hydrogeology of Crystalline Basement Aquifers in Africa*, volume 66, pages 203–220. Geological Society, London, Special Publications.
- Chen, J. and Rubin, Y. (2003). An effective Bayesian model for lithofacies estimation using geophysical data. *Water Resources Research*, **39**(5), 1118.
- Chen, J., Hubbard, S., and Rubin, Y. (2001). Estimating the hydraulic conductivity at the South Oyster Site from geophysical tomographic data using Bayesian techniques based on the normal linear regression model. *Water Resources Research*, **37**(6), 1603–1613.

- Chen, J., Hubbard, S., Rubin, Y., Murray, C., Roden, E., and Majer, E. (2004). Geochemical characterization using geophysical data and Markov chain Monte Carlo methods: A case study at the South Oyster bacterial transport site in Virginia. *Water Resources Research*, **40**(12), W12412.
- Chen, J., Hubbard, S., Peterson, J., Williams, K., Fienen, M., Jardine, P., and Watson, D. (2006). Development of a joint hydrogeophysical inversion approach and application to a contaminated fractured aquifer. *Water Resources Research*, **42**(6), W06425.
- Cook, A. M., Myer, L. R., Cook, N. G. W., and Doyle, F. M. (1990). The effects of tortuosity on flow through a natural fracture. In *Proceedings of the 31st US Symposium, Colorado School of Mines, Golden, CO, U.S.A.*, volume 31, pages 371–378. Geological Society Special Publication.
- Coscia, I., Greenhalgh, S. A., Linde, N., *et al.* (2011). 3-D crosshole ERT for aquifer characterization and monitoring of infiltrating river water. *Geophysics*, **76**(2), G49–G59.
- Cvetkovic, V. and Haggerty, R. (2002). Transport with multiple-rate exchange in disordered media. *Physical Review E*, **65**(5), 051308.
- Dafflon, B., Irving, J., and Holliger, K. (2009). Simulated-annealing-based conditional simulation for the local-scale characterization of heterogeneous aquifers. *Journal of Applied Geophysics*, **68**(1), 60–70.
- Daily, W. and Ramirez, A. (1989). Evaluation of electromagnetic tomography to map in situ water. *Water Resources Research*, **25**(6), 1083–1096.
- Darcel, C., Bour, O., and Davy, P. (2003). Stereological analysis of fractal fracture networks. *Journal of Geophysical Research*, **108**(B9), 2451.
- Davis, J. L. and Annan, A. P. (1989). Ground-penetrating radar for high-resolution mapping of soil and rock stratigraphy. *Geophysical Prospecting*, **37**(5), 531–551.
- Davy, P., Darcel, C., Bour, O., Munier, R., and De Dreuzy, J. R. (2006). A note on the angular correction applied to fracture intensity profiles along drill core. *Journal of Geophysical Research*, **111**(B11), B11408.
- Davy, P., Le Goc, R., Darcel, C., Bour, O., De Dreuzy, J. R., and Munier, R. (2010). A likely universal model of fracture scaling and its consequence for crustal hydromechanics. *Journal of Geophysical Research*, **115**(B10), B10411.
- Day-Lewis, F. D., Hsieh, P. A., and Gorelick, S. M. (2000). Identifying fracture-zone geometry using simulated annealing and hydraulic-connection data. *Water Resources Research*, **36**(7), 1707–1721.

- Day-Lewis, F. D., Lane Jr, J. W., Harris, J. M., and Gorelick, S. M. (2003). Time-lapse imaging of saline-tracer transport in fractured rock using difference-attenuation radar tomography. *Water Resources Research*, **39**(10), 1290.
- Day-Lewis, F. D., Singha, K., and Binley, A. M. (2005). Applying petrophysical models to radar travel time and electrical resistivity tomograms: Resolution-dependent limitations. *Journal of Geophysical Research*, **110**(B8), B08206.
- Day-Lewis, F. D., Lane, J. W., and Gorelick, S. M. (2006). Combined interpretation of radar, hydraulic, and tracer data from a fractured-rock aquifer near Mirror Lake, New Hampshire, U.S.A. *Hydrogeology Journal*, **14**(1), 1–14.
- De Dreuzy, J. R., Davy, P., and Bour, O. (2001). Hydraulic properties of two-dimensional random fracture networks following a power law length distribution: 1. Effective connectivity. *Water Resources Research*, **37**(8), 2065–2078.
- De Dreuzy, J. R., Davy, P., and Bour, O. (2002). Hydraulic properties of two-dimensional random fracture networks following power law distributions of length and aperture. *Water Resources Research*, **38**(12), 1276.
- De Marsily, G. (1986). *Quantitative Hydrogeology: Groundwater Hydrology for Engineers*, volume 440. Academic Press San Diego, California.
- Deparis, J. and Garambois, S. (2009). On the use of dispersive APVO GPR curves for thin-bed properties estimation: Theory and application to fracture characterization. *Geophysics*, **74**(1), J1–J12.
- Doetsch, J., Linde, N., Coscia, I., Greenhalgh, S. A., and Green, A. G. (2010). Zonation for 3-D aquifer characterization based on joint inversions of multimethod crosshole geophysical data. *Geophysics*, **75**(6), G53–G64.
- Doetsch, J., Linde, N., Pessognelli, M., Green, A. G., and Günther, T. (2012). Constraining 3-D electrical resistance tomography with GPR reflection data for improved aquifer characterization. *Journal of Applied Geophysics*, **78**, 68–76.
- Dorn, C., Linde, N., Le Borgne, T., Bour, O., and Baron, L. (2011). Single-hole GPR reflection imaging of solute transport in a granitic aquifer. *Geophysical Research Letters*, **38**(8), L08401.
- Dorn, C., Linde, N., Doetsch, J., Le Borgne, T., and Bour, O. (2012a). Fracture imaging within a granitic rock aquifer using multiple-offset single-hole and cross-hole GPR reflection data. *Journal of Applied Geophysics*, **78**, 123–132.
- Dorn, C., Linde, N., Le Borgne, T., Bour, O., and Klepikova, M. V. (2012b). Inferring transport characteristics in a fractured rock aquifer by combining single-hole GPR reflection monitoring and tracer test data. *Water Resources Research*, **48**(11), W11521.

- Ebihara, S., Sato, M., and Niitsuma, H. (2000). Super-resolution of coherent targets by a directional borehole radar. *Geoscience and Remote Sensing, IEEE Transactions on*, **38**(4), 1725–1732.
- Eisenburger, D. and Gundelach, V. (2000). Borehole radar measurements in complex geological structures. In *Proceedings of the Eighth International Conference on Ground-Penetrating Radar, SPIE*, volume 4084. International Society for Optics and Photonics.
- Engelder, T. (1987). Joints and shear fractures in rock. In B. K. Atkinson, editor, *Fracture Mechanics of Rock*, pages 27–69. Academic Press, London.
- Erhel, J., De Dreuzy, J. R., and Poirriez, B. (2009). Flow simulation in three-dimensional discrete fracture networks. *SIAM Journal on Scientific Computing*, **31**(4), 2688–2705.
- Ernst, J. R., Holliger, K., Maurer, H., and Green, A. G. (2006). Realistic FDTD modeling of borehole georadar antenna radiation, methodology and application. *Near Surface Geophysics*, **4**, 19–30.
- Farquharson, C. G. (2008). Constructing piecewise-constant models in multidimensional minimum-structure inversions. *Geophysics*, **73**(1), K1–K9.
- FOEN Switzerland (2009). Groundwater in Switzerland. Federal Office for the Environment (FOEN), available at <http://www.bafu.admin.ch/grundwasser/07496/07516>, accessed 7 November 2012.
- Gallardo, L. A. and Meju, M. A. (2007). Joint two-dimensional cross-gradient imaging of magnetotelluric and seismic traveltime data for structural and lithological classification. *Geophysical Journal International*, **169**(3), 1261–1272.
- Giannopoulos, A. (2005). Modelling ground-penetrating radar by GPRMax. *Construction and Building Materials*, **19**(10), 755–762.
- Glaser, R. E., Johannesson, G., Sengupta, S., *et al.* (2004). Stochastic engine final report: Applying Markov chain Monte Carlo methods with importance sampling to large-scale data-driven simulation. Technical report, Lawrence Livermore National Laboratory, Livermore, CA, U.S.A.
- Grasmueck, M. (1996). 3-D ground-penetrating radar applied to fracture imaging in gneiss. *Geophysics*, **61**(4), 1050–1064.
- Grègoire, C. and Joesten, P. K. (2006). Use of borehole radar tomography to monitor steam injection in fractured limestone. *Near Surface Geophysics*, **4**, 355–365.
- Griffiths, D. J. (1998). *Introduction to Electrodynamics*. Benjamin Cummings Publishing Company, 3rd edition.

- Hadermann, J. and Heer, W. (1996). The Grimsel (Switzerland) migration experiment: Integrating field experiments, laboratory investigations and modelling. *Journal of Contaminant Hydrology*, **21**(1), 87–100.
- Haggerty, R. and Gorelick, S. M. (1995). Multiple-rate mass transfer for modeling diffusion and surface reactions in media with pore-scale heterogeneity. *Water Resources Research*, **31**(10), 2383–2400.
- Haggerty, R., McKenna, S. A., Meigs, L. C., *et al.* (2000). On the late-time behavior of tracer test breakthrough curves. *Water Resources Research*, **36**(12), 3467–3479.
- Haggerty, R., Fleming, S. W., Meigs, L. C., and McKenna, S. A. (2001). Tracer tests in a fractured dolomite: 2. analysis of mass transfer in single-well injection-withdrawal tests. *Water Resources Research*, **37**(5), 1129–1142.
- Hao, Y., Yeh, T. C. J., Xiang, J., Illman, W. A., Ando, K., Hsu, K. C., and Lee, C. H. (2007). Hydraulic tomography for detecting fracture zone connectivity. *Ground Water*, **46**(2), 183–192.
- Harvey, C. and Gorelick, S. M. (2000). Rate-limited mass transfer or macrodispersion: Which dominates plume evolution at the Macrodispersion Experiment (MADE) site? *Water Resources Research*, **36**(3), 637–650.
- Hassan, A. E., Bekhit, H. M., and Chapman, J. B. (2009). Using Markov chain Monte Carlo to quantify parameter uncertainty and its effect on predictions of a groundwater flow model. *Environmental Modelling & Software*, **24**(6), 749–763.
- Hastings, W. K. (1970). Monte Carlo sampling methods using Markov chains and their applications. *Biometrika*, **57**(1), 97–109.
- Henry, D. (2010). Photo of granite fracture pattern taken at Schoodic Point, Acadia National Park Maine. available at <http://deejhenry.blogspot.ch/2010/07>, accessed 8 November 2012.
- Hollender, F., Tillard, S., and Corin, L. (2001). Multifold borehole radar acquisition and processing. *Geophysical Prospecting*, **47**(6), 1077–1090.
- Homer-Dixon, T. (1995). The ingenuity gap: Can poor countries adapt to resource scarcity? *Population and Development Review*, pages 587–612.
- Hubbard, S. S. and Linde, N. (2011). Hydrogeophysics. In P. Wilderer, editor, *Treatise in Water Science*, volume 2, pages 401 – 434. Elsevier.
- Hubbard, S. S., Rubin, Y., and Majer, E. (1997). Ground-penetrating radar-assisted saturation and permeability estimation in bimodal systems. *Water Resources Research*, **33**(5), 971–990.
- Ingebritsen, S. E. and Sanford, W. E. (2006). *Groundwater in Geologic Processes*. Cambridge University Press, 2nd edition.

- Jakubowicz, H. (1990). A simple efficient method of dip-moveout correction. *Geophysical Prospecting*, **38**(3), 221–245.
- Khalil, A. A., Stewart, R. R., and Henley, D. C. (1993). Full-waveform processing and interpretation of kilohertz cross-well seismic data. *Geophysics*, **58**(9), 1248–1256.
- Klimczak, C., Schultz, R. A., Parashar, R., and Reeves, D. M. (2010). Cubic law with aperture-length correlation: Implications for network scale fluid flow. *Hydrogeology Journal*, **18**(4), 851–862.
- Kogut, P. M. and Straley, J. P. (2001). Distribution-induced non-universality of the percolation conductivity exponents. *Journal of Physics C: Solid State Physics*, **12**(11), 2151–2159.
- Kosakowski, G. and Berkowitz, B. (1999). Flow pattern variability in natural fracture intersections. *Geophysical Research Letters*, **26**(12), 1765–1768.
- Krautkraemer, J. A. (1998). Nonrenewable resource scarcity. *Journal of Economic Literature*, **36**(4), 2065–2107.
- Laloy, E. and Vrugt, J. A. (2012). High-dimensional posterior exploration of hydrologic models using multiple-try DREAM (zs) and high-performance computing. *Water Resources Research*, **48**(1), W01526.
- Lane Jr, J. W., Haeni, F. P., Placzek, G., and Wright, D. L. (1996). Use of borehole-radar methods to detect a saline tracer in fractured crystalline bedrock at Mirror Lake, Grafton County, New Hampshire, U.S.A. In *Proceedings of the 6th Annual International Conference on Ground-Penetrating Radar, Sendai, Japan*, pages 185–190.
- Lane Jr, J. W., Haeni, F. P., and Versteeg, R. (1998). Use of a multi-offset borehole-radar reflection method in fractured crystalline bedrock at Mirror Lake, Grafton County, New Hampshire. In *Proceedings of the Symposium on the Applications of Geophysics to Engineering and Environmental Problems*, pages 359–368. Environmental and Engineering Geophysical Society.
- Lane Jr, J. W., Buursink, M. L., Haeni, F. P., and Versteeg, R. J. (2000). Evaluation of ground-penetrating radar to detect free-phase hydrocarbons in fractured rocks - results of numerical modeling and physical experiments. *Ground Water*, **38**(6), 929–938.
- Lapcevic, P. A., Novakowski, K. S., and Sudicky, E. A. (1999). The interpretation of a tracer experiment conducted in a single fracture under conditions of natural groundwater flow. *Water Resources Research*, **35**(8), 2301–2312.
- Lazaratos, S. K., Harris, J. M., Rector, J. W., and Van Schaack, M. K. (1995). High resolution cross well imaging of a West Texas carbonate reservoir: Part 4. reflection imaging. *Geophysics*, **60**(3), 702–711.

- Le Borgne, T. and Gouze, P. (2008). Non-fickian dispersion in porous media: 2. Model validation from measurements at different scales. *Water Resources Research*, **44**, W06427.
- Le Borgne, T., Bour, O., Paillet, F. L., and Caudal, J. P. (2006). Assessment of preferential flow path connectivity and hydraulic properties at single-borehole and cross-borehole scales in a fractured aquifer. *Journal of Hydrology*, **328**(1), 347–359.
- Le Borgne, T., Bour, O., Riley, M. S., *et al.* (2007). Comparison of alternative methodologies for identifying and characterizing preferential flow paths in heterogeneous aquifers. *Journal of Hydrology*, **345**(3), 134–148.
- Linde, N. and Doetsch, J. (2010). Joint inversion of crosshole GPR and seismic traveltime data. In R. D. Miller, J. H. Bradford, and K. Holliger, editors, *Advances in near-surface seismology and Ground-Penetrating Radar*, pages 1–18. Society of Exploration Geophysicists.
- Linde, N. and Pedersen, L. B. (2004). Evidence of electrical anisotropy in limestone formations using the RMT technique. *Geophysics*, **69**(4), 909–916.
- Linde, N., Chen, J., Kowalsky, M. B., and Hubbard, S. (2006a). Hydrogeophysical parameter estimation approaches for field scale characterization. In H. Vereecken, A. Binley, G. Casiani, A. Revil, and K. Titov, editors, *Applied Hydrogeophysics*, volume 71, pages 9–44. Springer Netherlands.
- Linde, N., Binley, A., Tryggvason, A., Pedersen, L. B., and Revil, A. (2006b). Improved hydrogeophysical characterization using joint inversion of cross-hole electrical resistance and ground-penetrating radar traveltime data. *Water Resources Research*, **42**(12), W12404.
- Liu, L., Lane, J. W., and Quan, Y. (1998). Radar attenuation tomography using the centroid frequency downshift method. *Journal of Applied Geophysics*, **40**(1), 105–116.
- Liu, S. and Sato, M. (2006). Subsurface water-filled fracture detection by borehole radar: A case history. *Journal of Environmental & Engineering Geophysics*, **11**(2), 95–101.
- Long, J., Remer, J. S., Wilson, C. R., and Witherspoon, P. A. (1982). Porous media equivalents for networks of discontinuous fractures. *Water Resources Research*, **18**(3), 645–658.
- Long, J., Aydin, A., Brown, S., *et al.* (1996). *Rock Fractures and Fluid Flow: Contemporary Understanding and Applications*. National Academies Press, Washington D. C.
- Looms, M. C., Jensen, K. H., Binley, A., and Nielsen, L. (2008). Monitoring unsaturated flow and transport using cross-borehole geophysical methods. *Vadose Zone Journal*, **7**(1), 227–237.
- Main, I. (1996). Statistical physics, seismogenesis, and seismic hazard. *Reviews of Geophysics*, **34**(4), 433–462.

- Mair, J. A. and Green, A. G. (1981). High-resolution seismic reflection profiles reveal fracture zones within a homogeneous granite batholith. *Nature*, **294**, 439–442.
- Małoszewski, P. and Zuber, A. (1985). On the theory of tracer experiments in fissured rocks with a porous matrix. *Journal of Hydrology*, **79**(3), 333–358.
- Maréchal, J. C., Dewandel, B., and Subrahmanyam, K. (2004). Use of hydraulic tests at different scales to characterize fracture network properties in the weathered-fractured layer of a hard rock aquifer. *Water Resources Research*, **40**(11), W11508.
- Marjoram, P., Molitor, J., Plagnol, V., and Tavaré, S. (2003). Markov chain Monte Carlo without likelihoods. *Proceedings of the National Academy of Sciences*, **100**(26), 15324–15328.
- Minnesota Geological Survey (2009). Photo of plumose fracture surface. available at http://en.wikipedia.org/wiki/File:Plumose_fracture.jpg, accessed 8 November 2012.
- Moreno, L. and Tsang, C. F. (1994). Flow channeling in strongly heterogeneous porous media: A numerical study. *Water Resources Research*, **30**(5), 1421–1430.
- Mosegaard, K. and Tarantola, A. (1995). Monte Carlo sampling of solutions to inverse problems. *Journal of Geophysical Research*, **100**(B7), 12431–12447.
- Neretnieks, I. (1993). Solute Transport in Fractured Rock: Applications to Radionuclide Waste Repositories. In J. Bear, C. F. Tsang, and G. de Marsily, editors, *Flow and Contaminant Transport in Fractured Rock*, pages 39–127. Academic Press San Diego, California.
- Neretnieks, I., Eriksen, T., and Tahtinen, P. (1982). Tracer movement in a single fissure in granitic rock: Some experimental results and their interpretation. *Water Resources Research*, **18**(4), 849–858.
- Neuman, S. P. (2005). Trends, prospects and challenges in quantifying flow and transport through fractured rocks. *Hydrogeology Journal*, **13**(1), 124–147.
- Neuman, S. P. and Di Federico, V. (2003). Multifaceted nature of hydrogeologic scaling and its interpretation. *Reviews of Geophysics*, **41**(3), 1014.
- Olsson, O., Falk, L., Forslund, O., Lundmark, L., and Sandberg, E. (1992). Borehole radar applied to the characterization of hydraulically conductive fracture zones in crystalline rock. *Geophysical Prospecting*, **40**(2), 109–142.
- Paillet, F. (1998). Flow modeling and permeability estimation using borehole flow logs in heterogeneous fractured formations. *Water Resources Research*, **34**(5), 997–1010.
- Palacky, G. J. (1988). Resistivity characteristics of geologic targets. In M. N. Nabighian, editor, *Electromagnetic Methods in Applied Geophysics*, volume 1, pages 53–129. Society of Exploration Geophysicists.

- Peterson Jr, J. E., Majer, E. L., and Knoll, M. D. (1999). Hydrogeological property estimation using tomographic data at the Boise hydrogeophysical research site. In *Proceedings of the Symposium on Applications of Geophysics to Engineering and Environmental Problems*, volume 12, pages 692–638. Environmental and Engineering Geophysical Society.
- Poirriez, B. (2011). *Étude et mise en œuvre d’une méthode de sous-domaines pour la modélisation de l’écoulement dans des réseaux de fractures en 3D*. Ph.D. thesis, Université Rennes 1.
- Pollard, D. D. and Aydin, A. (1984). Propagation and linkage of oceanic ridge segments. *Journal of Geophysical Research*, **89**(B12), 10017–10028.
- Postel, S. L. (2000). Entering an era of water scarcity: The challenges ahead. *Ecological Applications*, **10**(4), 941–948.
- Press, F. (1968). Earth models obtained by Monte Carlo inversion. *Journal of Geophysical Research*, **73**(16), 5223–5234.
- Ramirez, A. L. and Lytle, R. J. (1986). Investigation of fracture flow paths using alterant geophysical tomography. *International Journal of Rock Mechanics and Mining Sciences & Geomechanics Abstracts*, **23**(2), 165–169.
- Ramirez, A. L., Nitao, J. J., Hanley, W. G., *et al.* (2005). Stochastic inversion of electrical resistivity changes using a Markov chain Monte Carlo approach. *Journal of Geophysical Research*, **110**(B2), B02101.
- Renshaw, C. E. (1995). On the relationship between mechanical and hydraulic apertures in rough-walled fractures. *Journal of Geophysical Research*, **100**(B12), 24629–24636.
- Robinson, P. C. (1983). Connectivity of fracture systems - a percolation theory approach. *Journal of Physics A: Mathematical and General*, **16**(3), 605–614.
- Romero, C. E., Carter, J. N., Zimmerman, R. W., and Gringarten, A. C. (2000). Improved reservoir characterization through evolutionary computation. In *SPE Annual Technical Conference and Exhibition, Dallas, Texas*, 62942, pages 1–8. Society of Petroleum Engineers.
- Rubin, Y. and Hubbard, S. S., editors (2006). *Hydrogeophysics*, volume 50. Springer Netherlands.
- Ruelleu, S., Moreau, F., Bour, O., Gapais, D., and Martelet, G. (2010). Impact of gently dipping discontinuities on basement aquifer recharge: An example from Ploemeur (Brittany, France). *Journal of Applied Geophysics*, **70**(2), 161–168.
- Sato, M. and Miwa, T. (2000). Polarimetric borehole radar system for fracture measurement. *Subsurface Sensing Technologies and Applications*, **1**, 161–175.

- Schmelzbach, C., Scherbaum, F., Tronicke, J., and Dietrich, P. (2011). Bayesian frequency-domain blind deconvolution of ground-penetrating radar data. *Journal of Applied Geophysics*, **75**, 615–630.
- Slob, E., Sato, M., and Olhoeft, G. (2010). Surface and borehole ground-penetrating radar developments. *Geophysics*, **75**(5), A103–A120.
- Smith, L. and Schwartz, F. W. (1984). An analysis of the influence of fracture geometry on mass transport in fractured media. *Water Resources Research*, **20**(9), 1241–1252.
- Spillmann, T., Maurer, H., Willenberg, H., Evans, K. F., Heincke, B., and Green, A. G. (2007). Characterization of an unstable rock mass based on borehole logs and diverse borehole radar data. *Journal of Applied Geophysics*, **61**(1), 16–38.
- Stauffer, D. (1985). *Introduction to Percolation Theory*. Taylor and Francis Ltd., London, UK.
- Struckmeier, W. F. and Margat, J. (1995). *Hydrogeological Maps: A Guide and a Standard Legend*. Verlag Heise, Hannover.
- Subbey, S., Christie, M., and Sambridge, M. (2004). Prediction under uncertainty in reservoir modeling. *Journal of Petroleum Science and Engineering*, **44**(1), 143–153.
- Talley, J., Baker, G. S., Becker, M. W., and Beyrle, N. (2005). Four dimensional mapping of tracer channelization in subhorizontal bedrock fractures using surface ground-penetrating radar. *Geophysical Research Letters*, **32**(4), L04401.
- Tarantola, A. (2005). *Inverse Problem Theory and Methods for Model Parameter Estimation*. Society for Industrial Mathematics.
- Tarjan, R. (1972). Depth-first search and linear graph algorithms. *SIAM Journal on Scientific Computing*, **1**(2), 146–160.
- Terzaghi, R. D. (1965). Sources of error in joint surveys. *Géotechnique*, **15**(3), 287–304.
- Torrence, C. and Compo, G. P. (1998). A practical guide to wavelet analysis. *Bulletin of the American Meteorological Society*, **79**(1), 61–78.
- Touchard, F. (1999). *Caractérisation hydrogéologique d’un aquifère en socle fracture: Site de Ploemeur (Morbihan)*. Ph.D. thesis, University of Rennes I.
- Tronicke, J. and Holliger, K. (2005). Quantitative integration of hydrogeophysical data: Conditional geostatistical simulation for characterizing heterogeneous alluvial aquifers. *Geophysics*, **70**(3), H1–H10.
- Tsang, C. F. and Neretnieks, I. (1998). Flow channeling in heterogeneous fractured rocks. *Reviews of Geophysics*, **36**(2), 275–298.

- Tsang, Y. W. (1992). Usage of equivalent apertures for rock fractures as derived from hydraulic and tracer tests. *Water Resources Research*, **28**(5), 1451–1455.
- Tsoflias, G. P. and Becker, M. W. (2008). Ground-penetrating radar response to fracture-fluid salinity: Why lower frequencies are favorable for resolving salinity changes. *Geophysics*, **73**(5), J25–J30.
- Tsoflias, G. P. and Hoch, A. (2006). Investigating multi-polarization GPR wave transmission through thin layers: Implications for vertical fracture characterization. *Geophysical Research Letters*, **33**(20), L20401.
- Tsoflias, G. P., Halihan, T., and Sharp Jr, J. M. (2001). Monitoring pumping test response in a fractured aquifer using ground-penetrating radar. *Water Resources Research*, **37**(5), 1221–1229.
- Tsoflias, G. P., Van Gestel, J. P., Stoffa, P. L., Blankenship, D. D., and Sen, M. (2004). Vertical fracture detection by exploiting the polarization properties of ground-penetrating radar signals. *Geophysics*, **69**(3), 803–810.
- Turcotte, D. L. (1997). *Fractals and Chaos in Geology and Geophysics*. Cambridge University Press, 2nd edition.
- Waite Jr, A. H. (1966). International experiments in glacier sounding, 1963 and 1964. *Canadian Journal of Earth Sciences*, **3**(6), 887–892.
- Widess, M. B. (1973). How thin is a thin bed? *Geophysics*, **38**(6).
- Williams, J. H. and Johnson, C. D. (2004). Acoustic and optical borehole-wall imaging for fractured-rock aquifer studies. *Journal of Applied Geophysics*, **55**(1), 151–159.
- Witherspoon, P. A., Wang, J. S. Y., Iwai, K., and Gale, J. E. (1980). Validity of cubic law for fluid flow in a deformable rock fracture. *Water Resources Research*, **16**(6), 1016–1024.
- Wu, H. and Pollard, D. D. (1991). Fracture spacing, density, and distribution in layered rock masses: Results from a new experimental technique. In *The 32nd U.S. Symposium on Rock Mechanics (USRMS), Norman Oklahoma*. American Rock Mechanics Association.
- Yilmaz, Ö. (2001). *Seismic Data Processing*. Society of Exploration Geophysicists, Tulsa.
- Zheng, C., Bianchi, M., and Gorelick, S. M. (2011). Lessons learned from 25 years of research at the MADE site. *Ground Water*, **49**(5), 649–662.
- Zimmerman, R. W. and Bodvarsson, G. S. (1996). Hydraulic conductivity of rock fractures. *Transport in Porous Media*, **23**(1), 1–30.

- Zimmerman, R. W. and Yeo, I. W. (2000). Fluid flow in rock fractures: From the Navier-Stokes equations to the cubic law. In B. Faybishenko, P. A. Witherspoon, and S. M. Benson, editors, *Dynamics of Fluids in Fractured Rock, Geophysical Monograph*, volume 122, pages 213–224. American Geophysical Union, Washington, D. C.

Acknowledgements

This work would not have been possible without the support and the generous help of a number of people.

First of all, I sincerely thank Niklas Linde, my supervisor, for his guidance and for all of the personal and scientific support during my PhD. He gave me the unique opportunity to work on this interesting project; and his ideas and prompt valuable feedback greatly improved my work.

I also thank Klaus Holliger for giving me the chance to work in the UNIL Institute of Geophysics and for his support.

Special thanks to Tanguy Le Borgne and Olivier Bour, without whose support none of the work in this thesis would have been possible, as well as to Jean-Raynald de Dreuzy and Philipp Davy. Thanks for their invitation to Rennes and Barcelona, respectively, for their energy and enthusiasm for the project, and for helping me with all of my questions. I am very thankful to Sarah Leray who helped greatly with the Hydrolab code. Further acknowledgments go to the research group at University of Rennes 1-CNRS for their hospitality and for sharing their scientific thoughts, especially Maria Klepikova and the great Alphonse-Guerin-entourage.

I am thankful for the hard-working field assistants who came from the University Lausanne, University Rennes 1 and ETH Zürich during the two field campaigns at Stang-er-Brune. Their great company will remain in special memories. Thanks to Ludovic Baron who put a lot of effort into helping us with the preparation of the field campaigns.

I am thankful to Alan Green at ETH Zürich for making his GPR equipment available, as well as for providing access to a processing code. Thanks to Heinrich Horstmeyer for his technical support. Philippe Pezard at Géosciences Montpellier kindly made the geophysical logging data from the Stang-er-Brune site available.

Thanks to the people involved in peer-reviewing the individual chapters of this thesis for their constructive comments, including Hansruedi Maurer and Stewart Greenhalgh at ETH Zürich, Frederick Day-Lewis at the USGS, Matthew W. Becker at CSULB and other anonymous reviewers.

I had a great time enjoying the friendship and the inspiring environment of my colleagues at University of Lausanne.

Finally, thanks to my family and my friends for supporting me in good but also difficult times.

This research was supported by the Swiss National Science Foundation and the French National Observatory H+, to whom I express my gratitude.

Curriculum Vitae

Personal

Name	Caroline Dorn
Date of Birth	October 9, 1984
Citizenship	German

Education

2009–2013	PhD candidate at University of Lausanne, Switzerland
2008–2009	Diploma Thesis at ETH Zurich, Switzerland
2003–2009	Diploma (M.Sc.) in Geophysics, University Leipzig, Germany

Referred Publications

- Dorn, C., N. Linde, T. Le Borgne, O. Bour and M.V. Klepikova (2012). Inferring transport characteristics in a fractured rock aquifer by combining single-hole GPR reflection monitoring and tracer test data, *Water Resources Research*, **48**(11), W11521, doi:10.1029/2011WR011739.
- Dorn, C., N. Linde, J. Doetsch, T. LeBorgne, and O. Bour (2012). Fracture imaging within a granitic rock aquifer using multiple-offset single-hole and cross-hole GPR reflection data, *Journal of Applied Geophysics*, **78**, 123–132, doi: 10.1016/j.jappgeo.2011.01.010.
- Dorn, C., N. Linde, T. Le Borgne, O. Bour, and L. Baron (2011). Single-hole GPR reflection imaging of solute transport in a granitic aquifer, *Geophysical Research Letters*, **38**(8), L08401, doi:10.1029/2011GL047152.
- Carpentier, S., A. G. Green, J. Doetsch, C. Dorn, F. Campbell, H. Horstmeyer, A. E. Kaiser, J. Campbell, J. Pettinga, D. C. Nobes, R. Jongens, and M. Finnemore (2011). Recent deformation of Quaternary sediments in the northwest Canterbury Plains of New Zealand as inferred from GPR images and shallow P-wave velocity tomograms, **81**, 2–15, *Journal of Applied Geophysics*, special issue GPR, doi: 10.1109/ICGPR.2010.5550191.
- Dorn, C., S. Carpentier, A. E. Kaiser, A. G. Green, H. Horstmeyer, F. M. Campbell, J. Campbell, R. Jongens, M. Finnemore, and D. C. Nobes (2010). First seismic imaging of tectoni-

cally complex structures at shallow depths beneath the northwest Canterbury Plains, New Zealand, *Journal of Applied Geophysics*, **70**(4),317-331, doi:10.1016/j.jappgeo.2009.06.003.

Dorn, C., A. G. Green, R. Jongens, S. Carpentier, A. E. Kaiser, F. M. Campbell, H. Horstmeyer, J. Campbell, M. Finnemore, and J. Pettinga (2010). High-resolution seismic images of potentially seismogenic structures beneath the northwest Canterbury Plains, New Zealand, *Journal of Geophysical Research*, **115**(B11), B11303, doi:10.1029/2010JB007459.

Campbell, F. M., R. Jongens, A. G. Green, C. Dorn, S. Carpentier, A. E. Kaiser, H. Horstmeyer, J. Campbell, M. Finnemore, and J. Pettinga (submitted). Mapping and restoring Late Cretaceous - Present potentially seismogenic structures beneath the northwestern Canterbury Plains (New Zealand) based on high-resolution seismic reflection data and geological information, paper submitted to *New Zealand Journal of Geology and Geophysics*.